On the Fluid Mechanics of Self-Aeration in Open Channel Flows

Daniel Valero

Thesis submitted in partial fulfilment of
the requirements for the degree of
Doctor of Philosophy in Applied Sciences

Liège, Belgium November 2018

On the Fluid Mechanics of Self-Aeration in Open Channel Flows

Daniel Valero

Hydraulics in Environmental and Civil Engineering (HECE), Faculty of Applied Sciences, Université de Liège (ULiège)

Faculty of Civil Engineering, Aachen University of Applied Sciences (FH Aachen)

Jury:

Prof. Dr. Daniel B. Bung (Co-supervisor)	FH Aachen, Germany
Prof. Dr. Benjamin Dewals (President)	ULiège, Belgium
Dr. Sébastien Erpicum (Supervisor)	ULiège, Belgium
Prof. Dr. Nicolas Rivière	INSA Lyon, France
Prof. Dr. Anton Schleiss	EPFL, Switzerland
Prof. Dr. Vincent Terrapon	ULiège, Belgium

Liège, Belgium November 2018

"We do not want to imply that the equations are of little use; we merely want to make it unmistakenly clear that turbulence needs spirited inventors just as badly as dedicated analysts."

– Henk Tennekes and John L. Lumley (A First Course in Turbulence)

"With a thousand eyes, the river looked at him, with green ones, with white ones, with crystal ones, with sky-blue ones. How did he love this water, how did it delight him, how grateful was he to it! In his heart he heard the voice talking, which was newly awaking, and it told him: Love this water! Stay near it! Learn from it! Oh yes, he wanted to learn from it, he wanted to listen to it. He who would understand this water and its secrets, so it seemed to him, would also understand many other things, many secrets, all secrets."

– Hermann K. Hesse (Siddhartha)

Declaration

I hereby declare that except where specific reference is made to the work of others, the contents of this dissertation are original and have not been submitted in whole or in part for consideration for any other degree or qualification in this, or any other university. This dissertation is my own work and contains nothing which is the outcome of work done in collaboration with others, except as specified in the text and Acknowledgements.

Daniel Valero
November 2018

Acknowledgements

I would like to express my deepest appreciation for Prof. Bung and Dr. Erpicum, my guides through this doctoral journey. Without Prof. Bung, co-supervisor and friend, my work would have been mere equations with little application. Thanks for sharing your knowledge, for trusting me and encouraging me to always take tortuous ways; there is no joy in the paved road. My supervisor, Dr. Erpicum, has always been supportive and had a straightforward, wise answer. That was of great help for someone who gets lost in his own discussion. I am also grateful to the other Jury members, their valuable time and comments resulted in an improved thesis.

I have also greatly benefited from discussions with Prof. Chanson during my stay in Brisbane, his stay in Aachen and through e-mail correspondence. His never ending enthusiasm, broad knowledge and constructive feedback made the difference. I would also like to thank his colleagues, especially Dr. Zhang, Dr. Kramer and Dr. Leng for the kind welcome in Brisbane and

the avid exchanges. Dr. Zhang comments are also incorporated in Appendix A, as a result of a past collaboration.

I wish to thank Prof. Crookston. Many thanks for sharing your expertise, thoughtful comments and images. Thanks to Prof. Tullis and Prof. Oertel, both had high expectations on me, I wish this thesis does not disappoint them. Dr. Felder, Dr. Wang and Prof. Pfister are acknowledged, as some of their comments are incorporated in Chapter 1 as a result of a collaboration. Special thanks to Dr. Barkhudarov, his comments on Part III are appreciated. I would like to thank Prof. Dewals for following my doctoral advances. I would like to thank Dr. Amador for sharing his stepped spillway experimental dataset and Dr. Castro-Orgaz for sharing some historical data on smooth spillways.

I cannot forget about Prof. García Bartual, who originated my passion for fluid mechanics and research; Prof. Marco Segura, who always shared his insights on hydraulic structures; and Prof. Andrés Doménech, who was an unparalleled open channel flow professor. Thanks Rafa, Juan and Nacho. I am also especially grateful to Prof. García Raffi, who grew my enthusiasm for modelling and constantly looked after me. Thanks Luís.

I would like to thank Maurine Lodomez for providing with the French version of the Abstract, the students who have assisted me during the past years with experimental measurements and Rachael Talibart for sharing her stunning graphic art on waves.

I would like to thank Pepe, Agus, Jorge and Clara for the moments we shared back in Valencia; and Pablo, Ricard and Artur for the moments we shared in Aachen. Most especially, I want to thank Charlotte, who has been the ray of light on a rainy day.

A mi familia: Edu, Mari Carmen y José María, siempre os he sentido cerca. Sin vosotros, no estaría hoy escribiendo estas líneas.

Abstract

This dissertation is organized in five parts. Part I is made of four chapters which aim to introduce this dissertation and put it into the context of past developments. In Chapter 1, a historic analysis of air-water flow research in open channel flows is presented, jointly with a detailed discussion on research trends. Besides, aims and scope of this dissertation are clearly defined. Chapter 2 focuses on fundamental studies directly dealing with self-aeration, Chapter 3 deals with experimental studies on the self-aeration onset determination and Chapter 4 examines past attempts on numerical modelling of air-water flows. Part II describes the non-aerated region, which is of interest for the subsequent chapters. This part is intentionally divided into two chapters as to highlight the relevance of a commonly forgotten aspect: the free surface. Thereby, Chapter 5 deals with the water and air phases in the non-aerated flow region of spillways, whereas Chapter 6 is entirely dedicated to conceptualize the free surface. Main hypotheses related to the upcoming analytical

derivations are also examined in Chapter 6. Part III is the kernel of this dissertation and is divided into two chapters. The first one, Chapter 7, is dedicated to the mathematical derivations related to the equations governing the turbulent motion of a free surface. The main result of Chapter 7 is a kinematic and a dynamic equation that, together, yield a non-linear second-order differential equation describing the growth of the free surface perturbations. Chapter 8 aims to approximate, as accurately as possible, the forces acting over a free surface perturbation. The equations obtained in Chapters 7 and 8 allow computation of the growth rates for each wavelength, the free surface fluctuations spectra and the perturbations steepness. Part IV is composed of two chapters. Chapter 9 presents an application where capabilities of the derived equations are brought to light by means of a prototype scale application. Chapter 10 focuses on some empirical evidences obtained at a large-scale stepped spillway model. Perturbations growth is predicted by the developed theoretical model. Furthermore, it is shown that the free surface turbulent structure agrees, for the biggest wavelengths (gravitational dominated wavelengths), with that predicted by the mathematical analysis up to around 30 % of the non-aerated region length. Downstream, the energy distribution of these wavelengths starts changing. Notwithstanding that, the free surface structure at smaller wavelengths (surface tension dominated wavelengths) holds valid up to the inception point location. Further evidences also point in the direction of a breaking steepness as an appro-

priate parameter for self-aeration characterization. Part V contains a single chapter. This last chapter brings closure to this thesis and offers a discussion on the most relevant achievements and limitations of this doctoral work, together with an outlook into the future research challenges to be addressed. In summation, this investigation has provided with a fluid mechanics description of the self-aeration onset while demonstrating that it is the result of a new type of two-phase flow instability.

Résumé

Cette thèse est organisée en 5 parties. La Partie I se compose de quatre chapitres dont le but est d'introduire cette thèse de doctorat et de la positionner dans le cadre des développements réalisés par le passé. Dans le Chapitre 1, une analyse historique des recherches relatives aux écoulements eau-air à surface libre est présentée, en lien avec les différents courants qui ont sous tendus les développements successifs. Le Chapitre 2 se concentre sur les études fondamentales traitant majoritairement du phénomène d'auto-aération, le Chapitre 3 porte sur les études expérimentales qui se sont concentrées sur l'initiation de l'auto-aération et le Chapitre 4 examine les tentatives du passé pour modéliser numériquement les écoulements diphasiques eau-air. La Partie II décrit la région non-aérée, qu'il est nécessaire de bien comprendre pour aborder les chapitres suivants. Cette partie est intentionnellement divisée en deux chapitres de manière à mettre en évidence l'importance d'un paramètre généralement omis: la surface libre. Ainsi, le Chapitre 5 traite des phases eau et air dans

la région non-aérée des coursiers d'évacuateurs de crue tandis que le Chapitre 6 est entièrement dédié à la conceptualisation de la surface libre. Les principales hypothèses liées aux développements analytiques ultérieurs sont également examinées dans le Chapitre 6. La Partie III est le coeur de cette thèse de doctorat et est divisée en deux chapitres. Le premier, le Chapitre 7, est dédié à l'établissement mathématique des équations qui gouvernent le mouvement turbulent de la surface libre. Ce Chapitre 7 aboutit à une équation cinématique et une équation dynamique qui, ensemble, conduisent à une équation différentielle non-linéaire du second ordre qui décrit la croissance des perturbations de la surface libre. Le Chapitre 8 a pour but d'approximer, aussi précisément que possible, les forces agissant sur une telle perturbation de la surface libre. Les équations obtenues aux Chapitres 7 et 8 permettent le calcul du taux de croissance des perturbations de surface libre pour chaque longueur d'onde, des spectres de fluctuations et de la raideur des perturbations. La Partie IV est composée de deux chapitres. Le Chapitre 9 met en évidence les capacités des équations proposées au travers d'une application à échelle réelle. Le Chapitre 10 décrit quelques preuves empiriques obtenues sur un modèle à grande échelle de coursier en marches d'escalier. Le développement des perturbations est prédit par le modèle théorique proposé. De plus, il est montré que la structure turbulente de la surface libre est en accord, pour les plus grandes longueurs d'onde (dominées par la gravité), avec celle prédite par l'analyse mathématique jusqu'à environ 30 %

de la longueur de la région non-aérée. En aval, la distribution d'énergie de ces longueurs d'onde commence à changer. Malgré cela, la structure de la surface libre pour des longueurs d'onde plus petites (dominées par la tension superficielle) reste valide jusqu'au point d'initiation de l'aération. D'autres éléments corroborent l'idée selon laquelle la raideur limite est un paramètre pertinent pour caractériser l'auto-aération. La Partie V contient un seul chapitre. Ce dernier chapitre conclut la thèse et discute les principales réalisations du travail ainsi que leurs limites, tout en esquissant les enjeux pour les recherches futures. En conclusion, cette recherche fourni une analyse du problème de l'initiation de l'auto-aération basée sur les principes de la mécanique des fluides et démontre qu'elle est le résultat d'un nouveau type d'instabilité des écoulements diphasiques.

Kurzfassung

Die vorliegende Dissertation ist in fünf Teile gegliedert. Teil I setzt sich aus vier Kapiteln zusammen, welche in die grundlegende Thematik einführen und die nachfolgenden Inhalte der Arbeit in den Kontext früherer Erkenntnisse setzen. In Kapitel 1 wird ein Überblick über historische Forschungsergebnisse auf dem Gebiet der belüfteten Gerinneströmungen gegeben, einhergehend mit einer Diskussion aktueller Forschungsentwicklungen. Zudem werden Ziele und Umfang dieser Dissertation definiert. Kapitel 2 umfasst Grundlagen zur Selbstbelüftung. Kapitel 3 behandelt experimentelle Untersuchungen zu diesem Phänomen und Kapitel 4 fasst Untersuchungen zur numerischen Modellierung belüfteter Strömungen zusammen. Teil II beschreibt den unbelüfteten Fließbereich, welcher für die nachfolgenden Kapitel von Bedeutung ist. Dieser Teil ist in zwei Kapitel gegliedert, um die Relevanz eines meist vergessenen Aspekts zu unterstreichen: die freie Oberfläche. Dabei behandelt Kapitel 5 die Wasser- und Luft-Phase im unbelüfteten Bereich einer Schussrinne, während

Kapitel 6 der Konzeptionierung der freien Oberfläche gewidmet ist. Die wesentlichen Hypothesen in Bezug auf die nachfolgenden, analytischen Herleitungen werden ebenfalls in Kapitel 6 vorgestellt. Teil III ist der Kern dieser Dissertation und in zwei Kapitel gegliedert. Kapitel 7 behandelt die mathematischen Herleitungen von Gleichungen in Bezug auf die turbulente Bewegung der freien Oberfläche. Die wesentlichen Ergebnisse aus Kapitel 7 sind eine kinematische und eine dynamische Gleichung, welche gemeinsam zu einer nicht-linearen Differentialgleichung zweiter Ordnung zur Beschreibung des Zuwachses von Oberflächenperturbationen führen. Kapitel 8 hat zum Ziel, die auf diese Perturbationen wirkenden Kräfte mit bestmöglicher Genauigkeit zu beschreiben. Die in Kapitel 7 und 8 entwickelten Gleichungen erlauben die Berechnung der Zuwachsraten für verschiedene Wellenlängen, der Spektren von Oberflächenschwankungen und der Steilheit der Perturbationen. Teil IV setzt sich aus zwei Kapiteln zusammen. Kapitel 9 stellt die Anwendung der entwickelten Gleichungen auf ein Problem im Naturmaßstab vor. Kapitel 10 bezieht sich auf großmaßstäbliche Modellversuche und den dort gewonnenen, empirischen Belegen für das hier vorgestellte Konzept. Das dort gemessene Wachstum der Perturbationen stimmt mit den Ergebnissen des theroretischen Modells überein. Zudem wird gezeigt, dass die turbulenten Oberflächenstrukturen für die größten Wellenlängen (gravitationsdominierte Wellenlängen) mit den aus der mathematischen Beschreibung gewonnenen Ergebnissen bis zu einer Fließstrecke von 30 % des

unbelüfteten Fließbereichs übereinstimmen. Weiter unterhalb ändert sich der Energieanteil dieser Wellenlängen. Die Oberflächenstrukur der kleinsten Wellenlängen (oberflächenspannungsdominierte Wellenlängen) bleibt jedoch bis zum Erreichen des Selbstbelüftungspunkts erhalten. Ferner zeigen die Ergebnisse zeigen, dass ein Kriterium des Wellenbrechens als geeigneter Parameter zur Beschreibung der Selbstbelüftung herangezogen werden kann. Teil V besteht aus einem einzigen Kapitel. Dieses schließt diese Dissertation mit einer Diskussion der gewonnenen Ergebnisse und der Einschränkungen des hierin vorgestellten Konzepts. Außerdem wird der zukünftige, weitere Forschungsbedarf aufgezeigt. Zusammenassen lässt sich sagen, dass die vorliegende Studie eine strömungsmechanische Beschreibung des Prozesses der Selbstblüftung liefert. Dabei wird gezeigt, dass die Selbstbelüftung das Ergebnis einer neuartigen Zweiphasen-Strömungsinstabilität ist.

Resumen

Esta tesis doctoral está dividida en cinco partes. La Parte I se compone de cuatro capítulos donde se introduce esta tesis y se pone en el contexto de los desarrollos pasados. En el Capítulo 1 se desarrolla un análisis histórico de la investigación en flujos agua-aire y se ofrece una discusión sobre sus tendencias en investigación. Los objetivos de esta tesis también se presentan en este capítulo. El Capítulo 2 se centra en los estudios previos basados en desarrollos fundamentales relacionados con el inicio de la reaireación turbulenta, el Capítulo 3 resume los trabajos experimentales previos acerca de la determinación del inicio de reaireación y el Capítulo 4 examina la literatura relacionada con la modelación numérica de flujos agua-aire. La Parte II describe la región no aireada de los aliviaderos, que será de interés en los siguientes capítulos. Esta parte está intencionalmente dividida en dos capítulos, resaltando así la relevancia de un actor comúnmente olvidado: la lámina libre. De este modo, el Capítulo 5 describe los flujos de agua y de aire, mientras que el Capítulo 6

está dedicado exclusivamente a la conceptualización de la superficie libre. Las principales hipótesis relacionadas con las posteriores deducciones analíticas también son argumentadas en este capítulo. La Parte III es el núcleo de esta tesis doctoral y está dividida en dos capítulos. El Capítulo 7 está dedicado a deducir las ecuaciones que gobiernan el movimiento turbulento de una superficie libre. El principal resultado de este capítulo es una ecuación cinemática y otra dinámica que, juntas, dan lugar a una ecuación diferencial no-lineal de segundo orden que describe el crecimiento de las perturbaciones en la superficie libre. El Capítulo 8 tiene por objetivo aproximar de la forma más precisa posible las fuerzas que actúan sobre una perturbación. Las ecuaciones obtenidas en los Capítulos 7 y 8 permiten calcular el crecimiento de las perturbaciones, el espectro de fluctuaciones de la superficie libre y la distorsión para cada longitud de onda. La Parte IV está formada por dos capítulos. El Capítulo 9 presenta una aplicación donde las ecuaciones derivadas son puestas a prueba en una aplicación a escala de prototipo. El Capítulo 10 presenta varias evidencias empíricas en un modelo de un aliviadero escalonado a gran escala. El crecimiento de las perturbaciones es predicho por el modelo teórico desarrollado. Además, queda probado que la estructura turbulenta de la superficie libre, para las longitudes de onda más grandes (dominadas por la gravedad), se corresponde con la obtenida mediante el análisis matemático desarrollado hasta un 30 % de la extensión de la región no aireada del aliviadero. Aguas abajo, la distribución

de energía empieza a cambiar. Sin embargo, la estructura de la superficie libre para las longitudes de onda más cortas (dominadas por la tensión superficial) se mantiene válida hasta el punto crítico de reaireación. Los hallazgos obtenidos revelan que la distorsión de las perturbaciones es un parámetro apropiado para la caracterización del inicio de la reaireación. La Parte V únicamente contiene un capítulo. Este último capítulo cierra la tesis y ofrece una discusión acerca de los logros alcanzados y sus limitaciones, junto con una visión al futuro acerca de los retos que aún quedan por abordar. En resumen, la investigación desarrollada ha proporcionado una descripción basada en la mecánica de fluidos del proceso de reaireación y al mismo tiempo ha demostrado que su ocurrencia es el resultado de un nuevo tipo de inestabilidad propio de los flujos turbulentos multifase.

Table of contents

List of figures

List of tables

Nomenclature

Roman Symbols

A	Perturbation's amplitude or height
a_1	Best fit coefficients (Eq. 8.24)
a_2	Best fit coefficients (Eq. 8.24)
a_3	Best fit coefficients (Eq. 8.24)
B	Constant of integration of the law of the wall (Eq. 5.1)
B_{zz}	Autocorrelation function for the normal velocity fluctuations
C	Air concentration
C_f	Skin friction coefficient (Eq. 5.3)
C_m	Sectional mean air concentration

$D_{M,x}$	Coefficient of Eq. 5.8 for the streamwise normal stresses $(\overline{u'_x u'_x})$
$D_{M,y}$	Coefficient of Eq. 5.8 for the spanwise normal stresses $(\overline{u'_y u'_y})$
$D_{M,z}$	Coefficient of Eq. 5.8 for the normalwise normal stresses $(\overline{u'_z u'_z})$
D_x	Coefficient of Eq. 5.7 for the streamwise normal stresses $(\overline{u'_x u'_x})$
D_y	Coefficient of Eq. 5.7 for the spanwise normal stresses $(\overline{u'_y u'_y})$
D_z	Coefficient of Eq. 5.7 for the normalwise normal stresses $(\overline{u'_z u'_z})$
$E_{\eta\eta}$	One-dimensional free surface spectra
E_{zz}	One-dimensional normal velocity spectrum
F	Froude number $\left(q/\sqrt{g(\overline{h})^3}\right)$
f'	Non-inertial acceleration (Eq. 8.25)
F_*	Roughness Froude number (Eq. 3.5)
$\mathrm{F}_{*,\mathrm{v}}$	Roughness Froude number for stepped spillways (Eq. 3.9)
F_{gz}	Gravity force in the z direction (Eqs. 8.26 and 8.28)

f_κ	Eddy-perturbation interaction function (Eq. 8.7)
F_{pz}	Pressure force in the z direction (Eq. 8.28)
$F_{\sigma z}$	Surface tension force in the z direction (Eq. 8.24)
$F_{\tau z}$	Apparent stresses force in the z direction (Eqs. 8.17 and 8.19)
F_z	Force in the z direction
g	Gravity acceleration
g'	Net gravity accounting for the non-inertial acceleration (Eq. 8.25)
$\overline{h}$	Expected value of the flow depth
h	Instantaneous flow depth
h'	Expected value of the flow depth fluctuation
h_c	Critical depth
H_s	Depth from the upstream total energy line (at the reservoir) to the local water depth
k	Turbulence kinetic energy
k_A	Constant related to the perturbation's crest volume ($k_A \approx 0.234$)

k_{in}	Coefficient related to the flow entering the perturbation's control volume ($k_{in} \approx 0.298$)
k_Λ	Constant related to the perturbation's submerged volume ($k_\Lambda \approx 0.524$)
k_M	Coefficient related to the perturbation's submerged body ($k_M \approx -0.375$)
k_m	Coefficient related to the perturbation's crest ($k_m \approx 0.290$)
k_p	Coefficient related to the perturbation's submerged body (Eq. 7.12)
k_s	Equivalent sand roughness
k_v	Cavity depth (Eq. 3.8)
K_x	Coefficient of Eq. 5.7 for the streamwise normal stresses $(\overline{u'_x u'_x})$
K_ξ	Modified Bessel function of the second kind
K_y	Coefficient of Eq. 5.7 for the spanwise normal stresses $(\overline{u'_y u'_y})$
K_z	Coefficient of Eq. 5.7 for the normalwise normal stresses $(\overline{u'_z u'_z})$
L_{cav}	Cavity length
l_e	Eddy size

L_i	Distance to the inception point location, generally from the spillway vertex or gate (Fig. 2.1)
L_t	Turbulence lengthscale (Eq. 2.5)
$\mathscr{L}_{zz}$	Transverse integral lengthscale
M	Mass of the perturbation's submerged body (Eq. 7.6)
m	Mass of the perturbation's crest (Eq. 7.3)
m	Power law of the air defect velocity profile (Eq. 5.12)
M_p	Total mass of the perturbation ($M_p = M + m$)
$\mathbf{n}$	Unit vector normal to the control volume outer surface
n	Power law of the water velocity profile
N_Λ	Constant related to the perturbation's submerged body ($N_\Lambda \approx 0.5$)
$\mathscr{P}_p$	Perimeter of an elongated spheroid before breakup
p_σ	Pressure due to surface tension (Eq. 8.20)
P_z	Perturbation's momentum normal to the free surface (Eqs. 7.15 and 7.16)
q	Specific flow rate

R	Reynolds number
R	Radius of curvature (Eq. 8.21 for small displacements, and Eq. 8.22 for large displacements)
r	Radial coordinate inside the perturbation (Eq. 7.2)
r_d^2	Coefficient of determination
$\mathrm{R}_{76,x}$	Coefficient of Eq. 5.8 related to the Reynolds scale effects
$\mathrm{R}_{76,y}$	Coefficient of Eq. 5.8 related to the Reynolds scale effects
$\mathrm{R}_{76,z}$	Coefficient of Eq. 5.8 related to the Reynolds scale effects
S	Perturbation's steepness (Eq. 6.5)
s	Step height
S^*	Shape factor of the velocity profile (Eq. 5.4)
$\mathbb{S}_A$	Area enclosing the upper side of the crest of the perturbation
$\mathbb{S}_b$	Base area of the perturbation's crest ($\pi\lambda^2/4$)
$\mathbb{S}_\Lambda$	Area enclosing the lower side of the submerged body of the perturbation

S_{lim}	Breaking steepness (Eq. 6.7)
$\mathscr{S}_p$	Surface area of an elongated spheroid before breakup
t	Time
$\mathbf{u}$	Instantaneous velocity vector $\mathbf{u} = (u_x, u_y, u_z)$
$\overline{\tilde{u}_i'\tilde{u}_j'}$	Part of the velocity fluctuations that takes place in a scale smaller than the perturbation wavelength
u_{fs}	Free stream velocity
u_p	Perturbation's velocity in the streamwise direction
$\overline{u}_x$	Mean flow velocity
$\overline{u_x'u_z'}$	Velocity fluctuation covariance
u_z'	Velocity fluctuation normal to the free surface $\left(\sqrt{\overline{u_z'u_z'}}\right)$
v_{in}	Vertical component of the velocity entering the perturbation's control volume
$\mathbb{V}_m$	Volume of the perturbation's crest (Eq. 7.3)
$\mathbb{V}_p$	Total volume of the perturbation (Eq. 7.11)
v_p	Perturbation's velocity normal to the free surface
v_r	Bubble rise velocity

X	Coordinate with origin at the perturbation's radial axis, translation of $X = x - x_p$
Y	Coordinate with origin at the perturbation's radial axis, translation of $Y = y - y_p$
z	Normalwise coordinate
z_p	Perturbation's centre of gravity, z component (Eq. 7.8)

Greek Symbols

α	Parameter of the model spectrum (Eq. 8.12)
β	Angle between surface's normal and ultrasonic sensor's axis
δ	Boundary layer thickness (corresponding to the depth at which 0.99 times the free stream velocity is reached)
δ^*	Displacement thickness (Eq. 5.5)
δ^b	Blockage layer thickness (Eq. 6.2)
δ^v	Viscous layer thickness (Eq. 6.1)
ε	Turbulence kinetic energy dissipation
η	Deviation from the expected free surface level ($\eta = h - \overline{h}$)

Γ	Gamma function
θ	Chute slope
θ_m	Momentum thickness (Eq. 5.6)
κ	Perturbation's wavenumber (Eq. 6.6)
κ	von Kármán constant (Eq. 5.1)
κ_e	Eddy wavenumber (Eq. 8.8)
Λ	Amplitude of the perturbation's submerged body (Eq. 7.5)
λ	Perturbation's wavelength
λ_c	Taylor lengthscale (Eq. 6.3)
μ	Dynamic viscosity
ν	Kinematic viscosity
Π	Wake parameter (Eq. 5.1)
π	Ratio of a circle's circumference to its diameter ($\pi \approx 3.141592...$)
ρ	Density
σ	Air-water surface tension
τ	Apparent stress tensor

τ_0	Wall shear stress
χ	Coefficient related to the flow entering the perturbation's control volume (Eq. 7.21)
ξ	Parameter of the model spectrum (Eq. 8.9)
ω	Turbulence kinetic energy specific rate of dissipation

Superscripts

b	Relative to the blockage layer of the Hunt and Graham (1978) free surface description
v	Relative to the viscous layer of the Hunt and Graham (1978) free surface description

Subscripts

90	Relative to $C = 0.90$
a	Relative to the air phase
c	Relative to the Taylor lengthscale (Eq. 6.3)
δ	Relative to the boundary layer
e	Relative to an eddy
i	Relative to the inception point
p	Relative to a perturbation

s	Relative to the free surface
t	Turbulent quantity
w	Relative to the water phase
x	In the streamwise direction
z	In the normalwise direction

Acronyms / Abbreviations

ADM	Acoustic Displacement Meter
ADV	Acoustic Doppler Velocimetry
ArGEnCo	Département d'Architecture, Géologie, Environnement et Construction
ASCE	American Society of Civil Engineers
BW	Butterworth (filter)
CFD	Computational Fluid Dynamics
DES	Detached Eddy Simulation
DNS	Direct Numerical Simulation
E	Step Edge
FH Aachen	Aachen University of Applied Sciences (Fachhochschule Aachen)

HECE	Hydraulics in Environmental and Civil Engineering (research unit at ULiège)
HES	Hydraulics Engineering Section (department at FH Aachen)
IAHR	International Association for Hydro-Environment Engineering and Research
LBM	Lattice-Boltzmann Method
LDA	Laser Doppler Anemometry
LES	Large Eddy Simulation
MAD	Median Absolute Deviation
MED	Median operator
MSE	Mean Squared Error
N	Step Niche
ODE	Ordinary Differential Equation
PDE	Partial Differential Equation
PDF	Probability Density Function
PFEM	Particle Finite Element Method
PIV	Particle Image Velocimetry

PMF	Probability Mass Function
PSD	Power Spectral Density (function)
RANS	Reynolds Averaged Navier-Stokes (equations)
SAF	Saint Anthony Falls
SPH	Smoothed Particle Hydrodynamics
SS	Sweet-Spot of an ADV profile measurement
STD	Standard Deviation
ULiège	University of Liège
UQ	The University of Queensland
USS	Ultrasonic Sensor
VOF	Volume of Fluid

Preface

This thesis is the result of a collaboration between the research unit of Hydraulics in Environmental and Civil Engineering (HECE) at the University of Liège (ULiège) and the Hydraulics Engineering Section (HES) of the Aachen University of Applied Sciences (FH Aachen). My affiliation to the FH Aachen started by November 2014 as a Research Assistant and, a few months later (February 2015), I officially enrolled in the PhD programme of the Département d'Architecture, Géologie, Environnement et Construction (ArGEnCo), becoming a PhD candidate at ULiège. Given these particular conditions, most of the work has been conducted at FH Aachen, with regular meetings occurring intermittently at ULiège and FH Aachen. Additionally, I had the chance to spend a research stay at The University of Queensland (UQ) under the supervision of Prof. Dr. Chanson.

The goals of this PhD project remained open for a few months. This certainly provided me with a significant level of flexibility

which I have greatly benefited from. Both, my supervisor (Dr. Erpicum, ULiège) and my co-supervisor (Prof. Dr. Bung, FH Aachen), hold a considerable experimental modelling experience and have contributed to some relevant numerical modelling works. This unusual mixture of research approaches have been very present in my everyday work, thus leading to a few "hybrid" studies, making me well aware of the potential and need of numerical models.

Furthermore, I have a profound interest in the most fundamental aspects of Hydraulics. I can enjoy spending my time performing mind experiments with Partial and Ordinary Differential Equations (PDEs and ODEs), trying to sort them or predict their behaviour. Certainly, these mind experiments have taken more time than those physical and numerical ones I conducted in the laboratory. There is some magic on how the most non-linear behaviour of different types of systems can be comprised, as if encapsulated, in a short line with a few variables, basic sums/multiplications and some integral and differential operators. I am far from an expert though and, therefore, understanding the implications of some equations that I faced has oftentimes required a great effort and large amounts of coffee.

As my fluid mechanics book collection grew during the past years, so did my passion for the topic. Suddenly, I found myself discussing and questioning the most basic and widely accepted theories on self-aeration. Aforementioned circumstances lead

to the work presented in Valero and Bung (2018b), which is the main contribution of this thesis. Nevertheless, other publications have supported some chapters and appendices, as summarized in the following table:

Part	Chapter	Reference
I	1	Valero et al. (2018c)
	2	Valero et al. (2018c)
	3	Valero et al. (2018c)
	4	Valero et al. (2018c)
		Valero et al. (2018b)
II	5	Valero and Bung (2016)
		Valero and Bung (2018c)
	6	Valero and Bung (2018b)
III	7	Valero and Bung (2018b)
	8	Valero and Bung (2018b)
IV	9	Valero and Bung (2018b)
	10	*None*
V	11	*None*
Appendix	A	Zhang et al. (2018)
	B	Valero and Bung (2018b)
	C	Valero et al. (2018a)

This thesis is an attempt to address some relevant questions related to the self-aeration onset, as for instance which is the most relevant turbulence term or which is the structure of the free surface upstream of the inception point. On the question of "when does self-aeration occur?", it is common to talk about free surface "breakup". This can misleadingly induce the reader to think that the free surface – as a solid surface would do – "breaks" or gets damaged under the effect of a big stress. However, one does not see the free surface breaking but deforming; which, for common flows, occurs too fast for the human eye. When self-aeration takes place, some small water volumes jump into the air, but the free surface cannot be "damaged" as a material when dealing with a great stress.

At this point, we may all agree that the free surface contorts and deforms and is not "breaking", despite we can keep on using the term "breakup criterion" as a matter of tradition. The kinematic and dynamic equations derived in this thesis demonstrate the effect that turbulence, gravity and surface tension play. But, "when will the free surface stop growing?" It seems reasonable to think that the free surface will eventually reach an unstable configuration resulting in the collapse of the perturbations. Let's imagine a perturbation with a short wavelength but an enormous amplitude, our intuition says that this cannot remain stable. For wave applications, the steepness (amplitude over wavelength) has been extensively used as a limiting parameter and, despite the scatter, it has proven to be a useful parameter. For hydraulic en-

gineering flows, the obtained equations allow the computation of the slope for different wavelengths and – surprisingly – it can be observed that there are wavelengths that dominate. Values of the perturbations' steepness reach considerable larger magnitudes than those of the breaking sea waves, which can be explained by the stabilizing effect of surface tension at short wavelengths. Moreover, similar steepness ratios can also be observed in high-speed camera images of physical models. Hence, a wavenumber dependence of the thresholding steepness should be expected.

All in all, this thesis is a humble attempt to create a "theory of everything" for the self-aeration onset understanding. It is beyond my means to decide if this has been achieved. However, we can already confirm that, strictly speaking, self-aeration onset must be understood as a turbulent multiphase flow instability. I wish this can enlighten future researchers of our community. It is important to highlight that, strictly speaking, it is not a Kelvin-Helmholtz instability, which arises as a discontinuity of velocities across the interface between two fluids. It is not a viscous Kelvin-Helmholtz instability, similar to the previous one, but accounting for the damping/disturbing effect of viscosity. It is not a Rayleigh-Taylor instability, which would be related to the difference in the density of the fluids. It is neither a Plateau-Rayleigh instability, as in our case the turbulence effect is the driving force of the perturbations' growth. May we talk about a mixture of some of them? Or, differently, shall we start talking about a new type of turbulent multiphase flow instability?

Part I

Background

Chapter 1

Introduction

1.1 White waters

Self-aeration is a small-scale highly turbulent process commonly developing in large-scale hydraulic structures and steep natural streams. The wide range of scales involved makes its determination difficult and challenging. Nonetheless, it is a phenomenon of utmost importance which prevents from cavitation damage at solid surfaces (Falvey, 1990), thus ensuring structural stability of dams and outlet structures.

Downstream of the self-aeration onset, the flow depth and turbulence statistics change, transforming the flow into a complex multiphase flow made of a mixture of water droplets and waves with dispersed air bubbles travelling inside the bulked

flow (Bung, 2011; Chanson, 1996; Chanson and Toombes, 2002; Killen, 1968; Pfister and Hager, 2011; Straub and Anderson, 1958; Wilhelms and Gulliver, 2005). The flow structure is greatly altered with entrained air, being some of the most distinctive flow features the flow bulking and the energy dissipation modification. Turbulence is in turn affected by bubbles and, in high-speed open channel flows, water may be transported as droplets or spray surrounded by air as the carrier phase. Important considerations are also linked to the liquid-gas transfer, as the interfacial area between air and water phases drastically increases compared to the non-aerated open channel flow counterpart. As a consequence of this turbulent process, high quantities of dissolved oxygen are entrained (Bung, 2009; Erpicum et al., 2016; Toombes and Chanson, 2005), which can be crucial for the downstream habitat.

While it is still not clear which is the exact mechanism that results in the inception of air entrainment, its appearance is visually observable as a clear and sudden change on the water flow. The aerated flow is commonly called “white waters” and it is not strange to be observed in nature (e.g., Figs. 1.1 and 1.2). However, this “sudden” nature might only be apparent and self-aeration could be happening as a result of a continuous process which develops all through the non-aerated flow region, as disclosed in this dissertation. Special emphasis is put in this thesis on revealing the true development of the self-aeration onset and its link to the perturbations growing in the non-aerated region.

Differently, air entrainment due to jet impact (as it is the case of hydraulic jumps) may happen as a more localized phenomenon: a high velocity flow meets a slower flow body. However, Ervine (1998) highlighted the important effect of free surface perturbations in the entrained air quantities. Despite this type of aeration is not herein directly addressed, the theories developed in this theoretical work may have important implications as well.

Self-aeration onset has been traditionally described by the boundary layer intersection with the free surface (see Section 2.1), but many inconsistencies to this theory have been experimentally observed. It seems clear that turbulence has a big effect on this process, despite there is still not a clear consensus on which turbulent terms have a greater impact (Chanson, 2013a; Ervine and Falvey, 1987; Meireles et al., 2014). In complex three-dimensional flows, plunging jets and boundary layers occur simultaneously and the purely geometric criterion of the boundary layer interaction with the free surface would result insufficient. In jets convected through the air, no boundary layer can grow in contact with any solid surface but still the self-aeration can be observed.

Air entrainment on large hydraulic structures is of great interest. Particularly, spillway flows (Fig. 1.3) represent a canonical case where the channel geometry is well known and the turbulence effect can be easily studied as it increases gradually through the chute. Any advance on the understanding of self-aeration in

Fig. 1.1 Multnomah Falls, Columbia river gorge, United States of America. Photograph courtesy of Dr. Crookston.

Fig. 1.2 Breaking wave by the English Channel coast, Newhaven, East Sussex, South East Britain. “Sedna” from the collection “Sirens”, photograph courtesy of Rachael Talibart.

Fig. 1.3 Canal del Júcar control tank outlet spillway, Spain. The water surface roughens as the water approaches to the self-aeration onset.

hydraulic structures will also shed light on the understanding of self-aeration processes occurring on natural streams, where the boundary conditions make the problem much more of a three-dimensional puzzle.

1.2 Historic research on air-water flows

1.2.1 Early days

Air-water flow research dates back to the Austrian experimentalist Ehrenberger (1926), who first described air-water flows in chutes. Some of the proposed criteria and methods used were crude as compared to nowadays instrumentation standards. Ehrenberger (1926) defined the flow depth in aerated chute flows as the height above the bottom of the channel at which the uppermost ejected water droplets rebounded with a considerable force against a flat bar held in the channel perpendicular to the flow direction. The penetration of the aeration was determined by direct observation of “white waters” through the glassed chute wall. Air concentration measurements were attempted. Ehrenberger’s flow description already discerned between several layers that corresponded to different flow structures. Further information on this early work can be found in Killen (1968), Rao and Kobus (1975) and Hager (2016).

Lane (1939) first suggested that self-aeration occurs as a consequence of the boundary layer reaching the free-surface in a chute flow, which originated the need of an expression for the boundary layer development. Halbronn (1952) and Bauer (1954) first carried out this work for spillway flows and many more expressions were to come with the years. However, discrepancies were observed for mild and small slopes where self-aeration was not observed even after the intersection of the boundary layer with the free-surface (Anwar, 1994). Such observations probably motivated alternative entrainment theories. Hickox (1945) suggested that the kinetic energy of surface eddies should be sufficient to overcome the surface tension and Michels and Lovely (1953) suggested that a chute should have a minimum velocity and a minimum slope, in addition to the boundary layer criterion, for the air to be entrained. Soo (1956) suggested that the turbulent velocity should be greater than the bubble rise velocity so that bubble diffusion could take place.

A full session was dedicated to "Air entrainment by flowing water" during the 1953 joint meeting of IAHR (5th World Congress) and the Hydraulics Division of the American Society of Civil Engineers (ASCE) at the Saint Anthony Falls Laboratory in Minneapolis. Several authors, among them Viparelli, Halbronn, Straub, Lamb, Jevdjevich, Levin, and Peterka, presented their works related to prototype observations and model data of aerated flows along stepped chutes, vertical shafts and gates.

1.2.2 Selected milestones

The study of Straub and Anderson (1958) firmly embraced the boundary layer and free surface intersection concept as an explanation of self-aeration in chutes: "*it has been reasonably well established by several observers that for flows over a spillway from a quiescent reservoir, incipient aeration does not occur on the slope until a point or region is reached at which the boundary layer thickness is equal to the depth*". Straub and Anderson (1958) also spotted another aspect: "*the characteristic roughening of the water surface immediately upstream of the appearance of white water can be readily observed in such occurrences*". Concerning the main role of turbulence, Straub and Anderson (1958) stated that: "*the aeration phenomena are related to the conditions of turbulence in the flow*". Concerning the onset mechanism of flow aeration, Straub and Anderson (1958) anticipated the relevant role of velocity fluctuations normal to the flow: "*the components normal to the bed of the turbulent velocity fluctuations (...) near the surface that penetrate the surface will carry large clumps and smaller globules of water into the atmosphere against the force of gravity a distance proportional to the square of the individual transverse velocities*".

Straub and Anderson (1958) also properly described the shape of the typical air concentration profile based on measurements. When discussing the air concentration profile, Straub and Anderson (1958) foresaw one important flow feature: "*it*

appears that the complete curve is comprised of two parts which have basically different characteristics. Although there is no sharp demarcation between the two parts, the curves tend to support the description that in the lower regions of the stream air bubbles are suspended in water, while the upper regions consist of water droplets in air. The existence of these water droplets can readily be detected by holding one's hand just above the main flow". With greater detail, Straub and Anderson (1958) also described the aerated flow as: "*(1) an upper region of heterogeneous clumps, globules, and droplets of water ejected from the flowing liquid stream into the atmosphere at more or less arbitrary velocities, and (2) a lower region consisting of air bubbles distributed through the flow by turbulent transport fluctuations (...). Between the two regions is a transition zone defined by a transition depth which is a fluctuating surface necessarily at a statistical mean elevation above the channel bottom*". Straub and Anderson (1958) interpreted the air concentration profile as an equilibrium of turbulence and air buoyancy. Henceforth, the study of Straub and Anderson (1958) set a solid basis for air-water flow research and envisioned some of the major points that years still had to prove. Therefore, Lorenz Straub may not be only considered the founder of the Saint Anthony Falls Laboratory but also the father of air-water flow research by the hydraulic structures community.

Another milestone study is the PhD thesis of Killen (1968). John Killen was possibly the last of the faculty hired by Lorenz

Straub at Saint Anthony Falls (SAF) Laboratory[1] and, like Lorenz Straub and Killen's advisor (Alvin Anderson) previously did, established and reinforced some of the ideas that are still commonly accepted nowadays. Killen (1968) worked on the "waves and bubbles" description of the aerated region, which aims to better characterize the complex multiphase flow occurring in spillways. Also, Killen (1968) indicated that the presence of air bubbles did not alter the usual velocity distribution found in supercritical open channel flows. After the work of Killen (1968), the main contributions from the "school" of SAF Laboratory have come from John Gulliver on gas transfer in aerated flows (Gulliver et al., 1990) and on the air-water flow structure in spillways (Wilhelms and Gulliver, 2005).

In the decade of the 70's, the monograph of Rao and Kobus (1975) on self-aerated free surface flows was released. It covered many works published in technical reports and conferences that nowadays would be difficult to access. Rao and Kobus (1975) included topics such as fundamentals of air-water flows, inception point determination or aeration in spillways and hydraulic jumps. Kobus also played an important role for the air-water flow community by chairing the Esslingen Symposium on Scale Effects in Modelling Hydraulic Structures, which included two complete sessions on air entrainment and air-water mixtures.

[1] According to the obituary of John Mark Killen.

A further key figure in air-water flow research in spillways was Ian Wood, from the University of Canterbury. Wood's PhD students Keller (1972) and Cain (1978) performed prototype scale experiments on the Aviemore spillway. Based on these prototype scale data and other available laboratory observations, Wood et al. (1983) developed the "general method", which is the most accepted method up to now for the determination of the inception point location in smooth spillways. This method is still based on the original idea of Lane (1939). This "general method" would later be included in the IAHR[2] monograph of Wood (1991), which assisted on the large spread of this methodology. Wood (1985) delivered a Keynote Lecture in Melbourne's 21st IAHR (World) Congress – fully dedicated to air-water flows – which probably served as the basis of Wood (1991) monograph, that also received contributions from Kobus, Koschitzky, Volkart, Rutschmann and Pinto. Wood also supervised the PhD thesis of Chanson (1988) on aeration devices in spillways.

1.2.3 Recent research

After the IAHR monograph of Wood (1991), scientific production in air-water flow research increased considerably at numerous laboratories around the globe. Since the early 1990's, two re-

[2]International Association for Hydro-Environment Engineering and Research, founded in 1935, is a worldwide independent member-based organization of engineers and water specialists working in fields related to the hydro-environmental sciences and their practical application.

search groups stood out, namely the School of Civil Engineering of The University of Queensland (UQ) and the Laboratory of Hydraulics, Hydrology and Glaciology (VAW) at ETH Zurich.

At UQ, where Chanson established air-water flow research in the early 1990's, several milestone contributions on the study of self-aeration were produced (Chanson, 1994a,b, 1997) and the most acknowledged book on air-water flows in hydraulic engineering to date was released (Chanson, 1996). During the last two decades, Chanson contributed to the study of hydraulic jumps (Chanson, 2010; Chanson and Brattberg, 2000; Wang and Chanson, 2015; Zhang et al., 2013), stepped spillways (Chanson and Toombes, 2002; Felder and Chanson, 2009; Zhang and Chanson, 2018), plunging jets (Cummings and Chanson, 1997, 1999; Wang et al., 2018) and produced several studies on scale effects (Chanson, 2009; Chanson and Chachereau, 2013; Chanson and Gualtieri, 2008; Felder and Chanson, 2017; Murzyn and Chanson, 2008).

At ETH Zurich, in the early 1990's, Hager released a well-known monograph on energy dissipators (Hager, 1992) summarizing some of his previous works conducted at the École Polytechnique Fédérale de Lausanne (EPFL) on different types of hydraulic jumps. Hager's research also focused on stepped spillways (Boes and Hager, 2003; Pfister and Hager, 2011), bottom aeration over smooth inverts (Kramer et al., 2006), aerators (Pfister and Hager, 2010a,b; Rutschmann and Hager, 1990), free jets

(Heller et al., 2005; Pfister et al., 2014; Schmocker et al., 2008) and boundary layer development in spillways (Castro-Orgaz and Hager, 2010), among others.

Besides the contributions of the SAF Laboratory, University of Canterbury, UQ and ETH Zurich, notable inputs came from other researchers, namely:

- Rajaratnam, with studies on stepped spillways (Chamani and Rajaratnam, 1999; Rajaratnam, 1990) and hydraulic jumps (Liu et al., 2004; Long et al., 1991; Rajaratnam, 1965).
- Ervine, with studies on jets aeration (Ervine, 1998; Ervine and Falvey, 1987; Ervine et al., 1980).
- Matos, with studies on stepped spillways (Matos, 2000; Meireles and Matos, 2009; Meireles et al., 2012).
- Ohtsu and Yasuda, with studies on stepped spillways and hydraulic jumps (Chanson et al., 2002; Ohtsu and Yasuda, 1991; Ohtsu et al., 2004).
- Falvey, with relevant insights on aeration (Falvey, 1980) and cavitation (Falvey, 1990).
- Boes, with studies on stepped spillways and scale effects (Boes, 2000; Boes and Hager, 2003).

- Schleiss, with main contributions to rock erosion due to aerated jets (Bollaert and Schleiss, 2003).

1.3 Reviews, books and monographs on air-water open channel flows

To this day, several literature reviews, books and monographs on air-water flows have been published. Table 1.1 summarizes the main contributions of these types to air-water flow research. For completeness, Table 1.2 includes some other reviews, books and monographs not directly dealing with air-water flows but with an impact on this community.

Rajaratnam (1967) first presented a review on hydraulic jumps, covering different types of hydraulic jumps over different channel geometries. One of the earliest monographs that can be found is Rao and Kobus (1975), covering topics such as instrumentation, fundamentals and some practical considerations. Falvey (1980) presented an analysis of air entrainment in open channel flows, closed conduits and free-falling water jets. Falvey (1990) is probably the most widely acknowledged reference on cavitation in hydraulic engineering. Wood (1985) presented a keynote address on air-water flows in spillways in the 21st IAHR (World) Congress in Melbourne. Wood (1991) summarized the main advances in air-water flows up to 1988, with some extra references to later works. Another relevant monograph is that of

Table 1.1 Reviews, books and monographs on air-water flows.

Reference	Type of document
Rao and Kobus (1975)	Monograph
Falvey (1980)	Monograph
Wood (1985)	Review
Wood (1991)	Monograph
Chanson (1996)	Book
Ervine (1998)	Review
Prosperetti and Tryggvason (2009)	Book
Balachandar and Eaton (2010)	Review
Ishii and Hibiki (2010)	Book
Crowe et al. (2011)	Book
Bombardelli (2012)	Review
Kiger and Duncan (2012)	Review
Chanson (2013b)	Vision Paper (review)
Chanson (2015)	Monograph
Chanson (2016)	Review
Valero et al. (2018c)	Review

Table 1.2 Reviews, books and monographs in hydraulic engineering with an impact on the air-water flow community.

Reference	Type of document
Rajaratnam (1967)	Review
Falvey (1990)	Monograph
Hager (1992)	Monograph
Chanson (2002)	Book
Hager and Boes (2014)	Vision Paper (review)

Hager (1992) on hydraulic jumps and energy dissipators (divided into two parts), which is not dealing directly with air-water flows but presenting a complete source for different types of hydraulic jumps. The book of Chanson (1996) is the first book on hydraulic engineering with key focus on air-water flows, containing 19 chapters dealing with most types of air-water flows, covered both from an engineering and a scientific perspective; it is, probably, the most widely acknowledged reference in air-water flow research. The review paper of Ervine (1998) suggested three mechanisms of air entrainment affecting the rate of entrainment in plunging jets. Empirical equations for different parameters were also provided by Ervine (1998).

With the new century, Chanson (2002) focused on stepped spillway design and related air-water flow features, including the reanalysis of results of 45 laboratories and 4 prototype investigations. The first numerical modelling book dealing specifically with air-water flows is that of Prosperetti and Tryggvason (2009). Prosperetti and Tryggvason (2009) is a compendium of contributions by different authors on different aspects related to the numerical modelling of multiphase flows, thereby not specifically focusing on hydraulic structures. Balachandar and Eaton (2010) discussed on the interaction between carrier and dispersed phases. It covers topics such as preferential concentration, turbulence modulation and coupling between air and water phases. The book of Ishii and Hibiki (2010) contains 17 chapters on the fundamentals of multiphase flows, providing great insight on

conceptualization and modelling of multiphase flows. Crowe et al. (2011) is an extensive book on the fluid mechanics of multiphase flows, including experimental and numerical topics together with some air-water flow fundamentals. Bombardelli (2012) presented fundamentals of air-water flow modelling with some applications related to hydraulic structures. Kiger and Duncan (2012) presented a comprehensive discussion on the entrainment mechanisms in plunging jets, with some insights on breaking waves.

The Vision Paper of Chanson (2013b) synthetized air-water flow research with a pronounced hydraulic perspective, dealing with fundamentals, modelling and instrumentation, and offering a discussion on future milestones. The Vision Paper of Hager and Boes (2014) lays its focus on general hydraulic structures, with some comments on air-water flows, authors also present some historical discussion and personal opinions with a (positive) outlook into the future of hydraulic engineering and the remaining need for hydraulic laboratories. The recent monograph of Chanson (2015) contains basic discussions by several authors on air-water flows, but it is mainly focused on energy dissipation in different types of hydraulic structures. The review paper of Chanson (2016) discussed on the capabilities of phase detection probes. It provides an explanation of different signal processing techniques with several exemplary results.

The most recent review paper is that of Valero et al. (2018c), which covered a wide range of areas, including: air-water flow fundamentals, spillways, aerators, hydraulic jumps and stilling basins, aerated jets, instrumentation, scale effects and numerical modelling.

1.4 Recent research output

Research has gone *in crescendo* since the "early days" covered in (Section 1.2.1) and has experienced important boosts with the release of some of the aforementioned milestones. Figure 1.4 shows that significant contributions were released in the decade of the 1990's, probably assisted by the publication of Wood (1991) air-water flow IAHR monograph, which accounts over 200 citations in Google Scholar[3]. Similarly, the publication of the book of Chanson (1996), on general hydraulic engineering air-water flows, and the stepped spillways book of Chanson (2002), probably have had a big impact on the scientific production of the 2000's; both with over 400 citations in Google Scholar. Other works presented in Section 1.2 have also reached relatively high number of citations. However, for some of the classic works, the citation are lower than their impact. Some examples are Lane (1939) with around 20 citations or Killen (1968) remaining below

[3]Checked in November 2018.

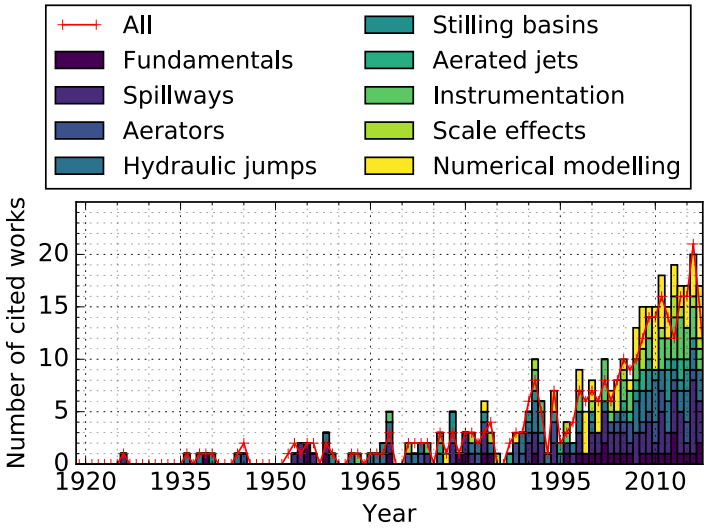

Fig. 1.4 Literature production on air-water flows as referenced by the review paper of Valero et al. (2018c).

30 citations. The main topics of research within the air-water flow discipline and its relative influence are shown in Fig. 1.5.

1.5 Motivation

Self-aeration is of utmost relevance to protect hydraulic structures against cavitation and also has an impact on the downstream dissolved oxygen quantities. The purely geometrical criterion of

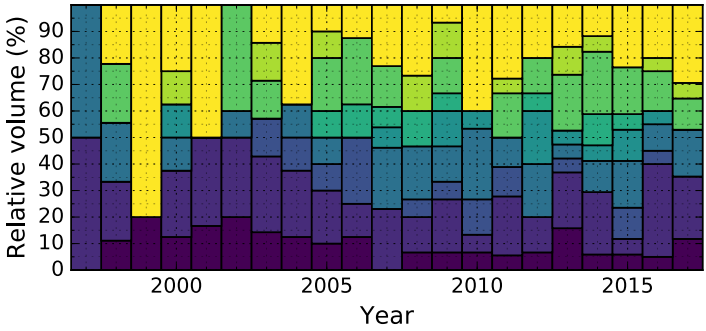

Fig. 1.5 Relative percentage of each research topic in the publication volume of the last 20 years as referenced by the review paper of Valero et al. (2018c), same legend as Fig. 1.4.

the boundary layer and free surface interaction appears to be the most widely accepted onset criterion (apart from experimental relations, largely constrained by scale effects and experimental conditions). Besides, this criterion is restricted to canonical spillway flows.

As shown in Section 1.4, there are numerous contributions on air-water flows. Nevertheless, little attention has been put on understanding how self-aeration is triggered. What is really causing the undisturbed free surface to roughen up to the point of breakup.

While numerical modelling has achieved some milestone advances in hydraulic engineering, it is still to be proven its utility

for large scale air-water flows. Needless to say: no satisfactory numerical model will be formulated for self-aeration without first understanding its driving mechanisms. Therefore, this work is motivated by the lack of understanding of the fluid mechanics related to the self-aeration onset.

1.6 Aims and scope

Given the aforementioned reasons, it seems clear that there is a need to provide with a strong, physically based explanation for the self-aeration onset and, ultimately, to formulate a general model that could be applied to complex three-dimensional flows. This summarizes the final goal of this work, which could be further expanded as:

- To provide a complete – fluid mechanics based – description of the self-aeration inception.
- To formulate, in the same terms, a mathematical framework for the practical determination of the self-aeration onset.
- To assess the validity of the derived equations.

Chapter 2

Fundamental studies

2.1 From high-speed flows to the boundary layer identification

In spillway flows, the distance to the inception point location is commonly measured from the spillway crest to the point where air entrainment occurs (henceforth L_i, as marked in Fig. 2.1). Despite the simplicity of this concept, this first point where air entrainment takes place has been defined in various ways (Meireles et al., 2012): visual observations, sections reaching a predefined mean air concentration or a bottom aeration level; which, together with the unstable and turbulent nature of the process, can yield different estimations in similar studies.

The first conceptualization of self-aeration – as a consequence of the boundary layer intersecting with the free surface – was developed through the milestone studies on smooth chute spillway air-water flows of Straub and Anderson (1958), Halbronn (1952), and Lane (1939). This relatively simple and purely geometric criterion defined the inception point as the location where the outer edge of the boundary layer reaches the free surface, hence leading to the abrupt appearance of white waters. This concept has been largely embraced by the hydraulic engineering community despite some inconveniences, as recently listed by Valero and Bung (2016). It has led to different inception point location formulations based on the same idea. Some examples are Bauer (1954), Keller and Rastogi (1975) and, the most accepted up to date, Wood et al. (1983); further described in Wood (1991). All these formulations aimed to obtain the distance at which the self-aeration occurred in a smooth spillway, thereby not being applicable to other different types of flows or structures.

2.2 Turbulence effect: shear stresses or normal velocity fluctuations?

Nonetheless, the boundary layer concept allowed an easy computation of the inception point location and, if necessary, formulations could be easily tuned by modifying a few coefficients.

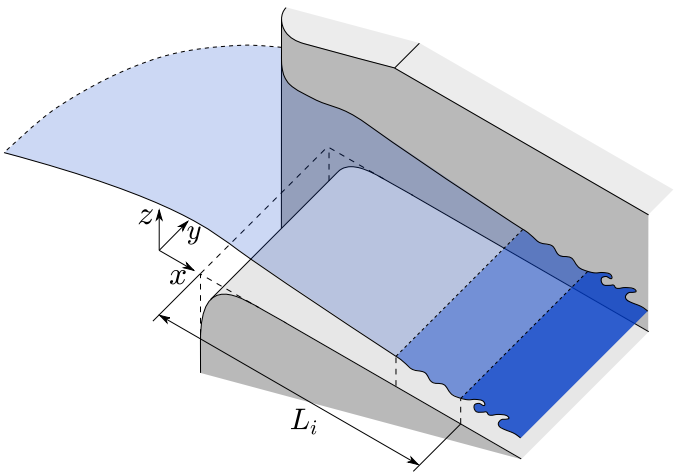

Fig. 2.1 Spillway flow and inception point location (L_i) definition.

The study of Wood et al. (1983) was probably motivated by the discrepancies found when using the available methods to predict self-aeration data of Cain (1978). This original concept was already uncovering the more physically based idea of turbulence as a disturbing force overcoming some resistance exerted by the fluid. Chanson (2009, 2013a) better outlined this concept: bubble entrainment would take place when the shear stress is greater than the surface tension force per unit area preventing the collapse of the free surface. This condition defined by Chanson (2009, 2013a), including both the turbulent and the viscous shear stresses at the free surface, can be expressed as (Valero and Bung, 2016)[1]:

$$\left| \mu_f \frac{\partial \overline{u}_x}{\partial z} - \rho_f \overline{u_i' u_j'} \right| > \sigma \frac{\mathscr{P}_p}{\mathscr{S}_p} \tag{2.1}$$

where σ is the air-water surface tension, f can refer to either the water ($f = w$) or the air ($f = a$) phase and $i \neq j$ (shear terms). μ and ρ are the dynamic viscosity and density, respectively. The coordinate x is aligned with the flow direction and z is normal to

[1]The contribution of Valero and Bung (2016) comes from suggesting that, if shearing is the cause of breakup, then all the sources of shearing should be contemplated, i.e.: shearing due to the velocity gradient resulting from the air-water no-slip condition, the turbulent shear stresses produced at the water boundary layer close to the spillway bed and walls and the shear stresses due to the air drag. Note that the shear at the outer edge of the water boundary layer nulls while, in the air region, the peak values would occur close to the free surface. Nonetheless, the density of the air is roughly three orders of magnitude smaller.

the mean free surface (as marked in Fig. 2.1); thus, $\overline{u}_x$ is the mean streamwise velocity and $\overline{u'_x u'_z}$ the main turbulent shear stress (at the channel centreline). $\mathscr{P}_p$ and $\mathscr{S}_p$ are the perimeter and the surface area of the perturbation[2] before breakup. The criterion defined by Eq. 2.1 considers that the free surface is able to resist up to a shear limit (likewise a solid surface), which is provided solely by the surface tension.

Previously, Ervine and Falvey (1987) and Hino (1961) suggested that self-aeration could occur due to the turbulent velocity fluctuations normal to the free surface. The criterion of Ervine and Falvey (1987) can be expressed as:

$$u'_z \geq \sqrt{\frac{4\,\sigma}{\rho_w\,R}} \tag{2.2}$$

with $u'_z = \sqrt{\overline{u'_z u'_z}}$ the velocity fluctuation normal to the free surface and R the radius of curvature of the free surface undulation. Additionally, u'_z is usually required to be greater than the bubble rise velocity v_r (e.g., Boes and Hager, 2003; Chanson, 1993) which, for a flow over a chute with slope θ, can be written as:

$$u'_z \geq v_r \cos(\theta) \tag{2.3}$$

[2] Which corresponds to an elongated spheroid, according to Chanson (2009).

Equation 2.3 is the mathematical transcription of the Soo (1956) criterion. Chanson (1993), using Eqs. 2.2 and 2.3, computed the necessary u'_z value to overcome surface tension and the rising velocity of a bubble (buoyancy) concluding that values ranging from 0.1 to 0.3 m/s would lead to entrained bubbles of sizes around 8 to 40 mm. Ervine (1998) analysed different studies on plunging jets aeration, pointing out the strong relation between the free surface disturbances and the air entrainment rates.

2.3 An energy based approach and the role of gravity

Brocchini and Peregrine (2001) presented a descriptive analysis of the aeration onset, focusing the discussion on the relation between turbulence (unstabilizing), surface tension and gravitational (stabilizing) energies and their effect on the surface roughness and breakup. With the study of Brocchini and Peregrine (2001), a new framework for the understanding of aeration problems was established whereas large uncertainty was still involved, hence preventing the definition of sharper bounds for the air entrainment onset. Likewise, Hirt (2003) and Souders and Hirt (2004) suggested an energy based criterion, proposing a balance between turbulence kinetic energy (k, as the disturbing phenomenon) and surface tension and gravity (as stabilizing

factors). Thus, it was proposed that air entrainment would occur when:

$$\rho_w k > \rho_w g_z L_t + \frac{\sigma}{L_t} \tag{2.4}$$

being g_z the gravity component normal to the free surface (taken in absolute value) and L_t the turbulence lengthscale as computed by the employed turbulence model. Making use of ε, the kinetic energy dissipation, L_t can be defined on the basis of dimensional analysis:

$$L_t \sim \frac{k^{3/2}}{\varepsilon} \tag{2.5}$$

Equation 2.5 is directly considered as a strict equality by Pope (2000). Otherwise, and depending on the turbulence model used, different authors define a model constant to formulate the equality; see for instance Wilcox (2006) for a review on different turbulence models, the original work of Launder and Spalding (1974) on $k-\varepsilon$ model or the L_t definition of Souders and Hirt (2004) for the criterion of Hirt (2003) coupled with the RNG $k-\varepsilon$ turbulence model.

The model given by Eq. 2.4 is better suited for Computational Fluid Dynamics (CFD) modelling (Meireles et al., 2014; Valero and García-Bartual, 2016) than the geometric method of Wood et al. (1983), allowing air entrainment onset estimation

in complex three dimensional problems. Equation 2.4, together with the Reynolds Averaged Navier-Stokes (RANS) equations, has been used by Bombardelli et al. (2011) and Valero and Bung (2015) to satisfactorily estimate the inception point location in stepped spillway cases, where k shows a faster growth compared to smooth spillways. However, some difficulties can arise for other types of hydraulic structures.

2.4 Other fundamental advances on air-water flow research

While the intrinsic structure of typical single-phase shear flows has been well described over the past decades (e.g., Davidson, 2015; Pope, 2000; Schlichting, 1979; White, 2006), fundamental studies on air entrainment have been scarce and knowledge is far away from the level of comprehension of other disciplines. As an example, the understanding gained in boundary layer flows with the milestone study of Klebanoff (1955) is still to be achieved in uniformly aerated flows. Despite the original study of Straub and Anderson (1958) providing some of the still accepted insights on theoretical air-water flows, up to date, only one book focused thoroughly on the fluid mechanics of air-water flows in common hydraulic structures (Chanson, 1996), being well complemented by the now more than 25 years old IAHR monograph of Wood (1991).

For plunging jets, a high velocity impact on a fluid body causes vorticity production. Entrainment conditions for jets have been proposed for low- and high-viscosity plunging jets (Kiger and Duncan, 2012), including the empirical correlation of Cummings and Chanson (1999). Discussion on the entrainment mechanisms and entrapped air quantities in plunging jets can be found in the review works of Ervine (1998) and Kiger and Duncan (2012). Recent findings on jet velocities, turbulence structures and air concentration profiles can be found in Bertola et al. (2018) and Wang et al. (2018).

The sectional mean air concentration (C_m) varies with the spillway slope (Wood, 1983). The structure of the air-water flow in spillways was first thoroughly investigated by Killen (1968), who distinguished between entrapped and entrained air. Nonetheless, Straub and Anderson (1958) had already described the characteristic free surface roughening upstream of the inception point and distinguished between two regions in the air-water flow cross section: a lower region with air bubbles suspended in water and an upper region with droplets in air; with no sharp transition in between. Wilhelms and Gulliver (2005) extended the study of Killen (1968). Other authors have also provided insight on the different mean concentration levels in air-water flows (Bung, 2013; Felder and Chanson, 2016; Pfister, 2008).

A significant approach related to the vertical air profiles is the conceptualization of air concentrations with an advective-

diffusive theory (Chanson, 1996; Chanson and Toombes, 2002; Wood, 1984). The solution of the diffusive equations can also provide the entrapped air concentration related to the waved flow. Assuming a normal distribution of the free surface location (and no entrained bubbles) an error function type profile can be obtained for the air concentration, as shown by Valero and Bung (2016). The close agreement between the advective-diffusion model for smooth chutes by Chanson and Toombes (2002) and experimental observations of the waved interface in the non-aerated flows on a smooth spillway chute was also recently confirmed (Zhang et al., 2018). Thus, advective-diffusive equations can capture well both regions of air-water flows: dispersed bubbles and waved profiles.

Figure 2.2 shows several air concentration (C) profiles as a function of the dimensionless flow depth ($z/\overline{h}_{90}$), with z the coordinate normal to the flow. The semi-theoretical air concentration profiles of Wood (1984), Chanson (1996), Chanson and Toombes (2002) and the analytical profile for entrapped air of Valero and Bung (2016) are presented for completeness. The waved flow analytical profile of Valero and Bung (2016) is extended over its limitations (also used in profiles where bubbles are expected) and profiles of Wood (1984), Chanson (1996) and Chanson and Toombes (2002) are also used in the non-aerated region to show that free surface roughness can be captured also by a diffusive model, despite falling out of its hypotheses. It can be observed in Fig. 2.2 that Chanson and Toombes (2002) reproduces better

stepped spillway data while Chanson (1996) seems to better fit the smooth spillway data of Straub and Anderson (1958). The profile of Wood (1984) shows a reasonable good fit despite using a constant diffusivity across the entire flow profile.

Several studies have reported bubble chord lengths and related variables, but no universal law has been obtained. Some insight might be gained from the study of the Hinze scale (see Deane and Stokes, 2002; Hinze, 1955), despite recent controversy (Lubin and Chanson, 2017). Establishment of a universal bubble size spectrum and bubble shapes would lead to a more accurate description and understanding of air-water flows, allowing better prediction of its behaviour and an easier input from the multiphase flow community which has focused on a broader range of two-phase flows (e.g., Ishii and Hibiki, 2010).

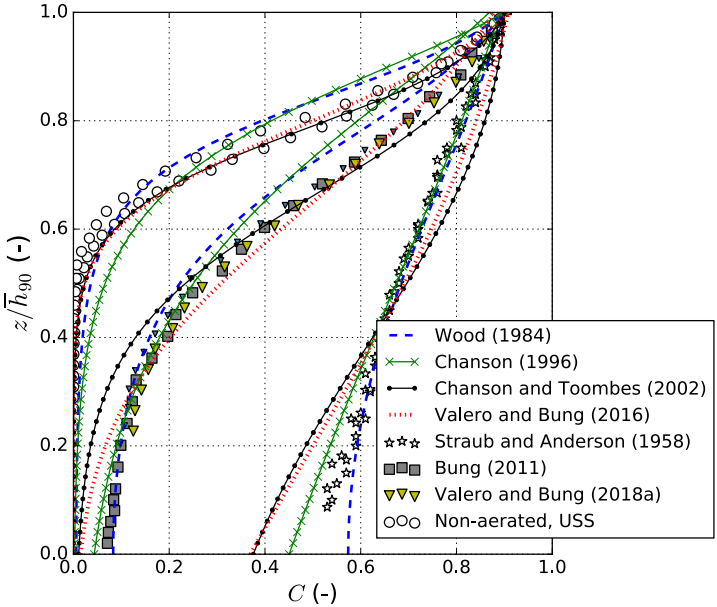

Fig. 2.2 Air concentration profiles for $C_m \approx 0.20$, 0.35 and 0.67. Data on the non-aerated region is included from an ultrasonic sensor (USS). Data of Valero and Bung (2018a) corresponds to a single tip optical fibre probe and data of Bung (2011) to a double tip conductivity probe, both data are from stepped spillways. Data of Straub and Anderson (1958) correspond to the slope of 60 º in a smooth chute.

Chapter 3

Experimental studies

3.1 General remarks

After 60 years from the milestone study of Straub and Anderson (1958), there is still lack of an undisputed inception point formulation (Meireles et al., 2012); remaining as the best alternative the empirical relations proposed for each type of flow. Main handicap of empirical estimations relies on scale effects affecting the models and that every type of flow requires a new and different experiment. Disparity on how this inception point is defined, can also yield discrepancies for similar models from different studies.

3.2 Critical point determination of Wood et al. (1983)

This method, formulated by Wood et al. (1983), became widely accepted after the release of the IAHR monograph of Wood (1991). The method of Wood et al. (1983) is based on the assumption that self-aeration occurs "where the boundary layer reaches the water surface". Thus, the matter of defining an equation for the boundary layer (δ) growth is a key issue, for which Wood et al. (1983) proposed the following expression:

$$\frac{\delta}{x} = 0.0212 \left(\frac{x}{H_s}\right)^{0.11} \left(\frac{x}{k_s}\right)^{-0.10} \tag{3.1}$$

with H_s defined as the drop height[1] at a distance x, and k_s is the spillway roughness. Method of Wood et al. (1983) is based on a multiple regression analysis of the theoretical developments of Keller and Rastogi (1977), covering a range of chute slopes, discharges and roughnesses.

When the free surface profile is known ($\overline{h}$), the aeration criterion can be defined by the following condition: $\delta = \overline{h}$. Wood (1991) proposed the computation of the free surface profile by decomposing it into the boundary layer and free stream flow components:

[1] Depth difference between the reservoir energy level to the flow depth of a section at a distance x.

$$\overline{h} = \delta + (q - q_\delta)/u_{fs} \tag{3.2}$$

being q the specific discharge, u_{fs} the free stream velocity and q_δ the discharge within the boundary layer thickness, which can be computed as (Wood, 1991):

$$q_\delta = \frac{n}{n+1}\delta\sqrt{2gH_s} \tag{3.3}$$

with g the gravity acceleration and n the power law exponent of the velocity profile. It is usually more convenient to directly compute the distance to the inception point location (L_i), which can be done following (Wood et al., 1983):

$$\frac{L_i}{k_s} = 13.6\sin(\theta)^{0.0796}(\mathrm{F}_*)^{0.713} \tag{3.4}$$

being θ the spillway slope and F_* the roughness Froude number, defined as:

$$\mathrm{F}_* = q/\sqrt{g\sin(\theta)k_s^3} \tag{3.5}$$

The flow depth at the inception point location ($\overline{h}_i$), according to Wood et al. (1983), can be computed as:

$$\frac{\overline{h}_i}{k_s} = \frac{0.223}{\sin(\theta)^{0.04}}(\mathrm{F}_*)^{0.643} \tag{3.6}$$

Wood (1991) argued that the first point of self-aeration may occur upstream of this critical point as the instantaneous boundary layer thickness shows an irregular profile.

According to Wood et al. (1983), Eq. 3.1 yields a standard error around $+/-$ 3 % for laboratory and field data on smooth spillways. Recently, Hunt and Kadavy (2013) found that the method of Wood et al. (1983) provides reasonable estimations for stepped spillways ($+/-$ 20 % uncertainty), despite originally formulated for smooth spillways. Hunt and Kadavy (2013) suggested that differences may be explained by the different inlet condition (broad crested weir in their study). Findings of Hunt and Kadavy (2013) are also consistent with the distinct coefficients of the empirical relation of Chanson (1994b) for stepped spillways, which was based on the original work of Wood et al. (1983).

3.3 Stepped spillway relation of Chanson (1994b)

Chanson (1994b) analysed prototype stepped spillway data and, following the equation form of Wood et al. (1983), proposed the following expression:

$$\frac{L_i}{k_v} = 9.8 \sin(\theta)^{0.080} (\mathrm{F}_{*,\mathrm{v}})^{0.71} \tag{3.7}$$

with k_v the cavity depth, defined as:

$$k_v = s\cos(\theta) \tag{3.8}$$

being s the step height. Note that the roughness Froude number has also changed as k_v is introduced into F_* of Eq. 3.5 as well, which could otherwise be defined as:

$$\mathrm{F}_{*,\mathrm{v}} = q/\sqrt{g\sin(\theta)k_v^3} \tag{3.9}$$

Here, k_s has simply been substituted by k_v, as it is commonly done in literature, but homology between the sand roughness coefficient and the cavity through should be subject to further discussion.

For the flow depth at the inception point location, Chanson (1994b) proposed:

$$\frac{\overline{h}_i}{k_v} = \frac{0.4}{\sin(\theta)^{0.04}}\left(\mathrm{F}_{*,\mathrm{v}}\right)^{0.64} \tag{3.10}$$

The criterion of Chanson (1994b) was deduced using prototype and model data with spillway slopes between 27 º to 52 º (Chanson, 1994b) and seems to yield a good fit for a wide range of prototype scale stepped spillway data (see Fig. 3.5 of Chanson et al., 2015). It must be noted that data on the inception point location at prototype scale generally correspond to visual observations.

3.4 Stepped spillway relation of Chanson (2002)

Chanson (2002) proposed an expression similar to Eq. 3.7 which accounts for a slightly wider range of slopes (20 º < θ < 55 º):

$$\frac{L_i}{k_v} = 9.719 \sin(\theta)^{0.0796} (\mathrm{F}_{*,\mathrm{v}})^{0.713} \tag{3.11}$$

and for the flow depth at the inception point location:

$$\frac{\overline{h}_i}{k_v} = \frac{0.4034}{\sin(\theta)^{0.04}} (\mathrm{F}_*)^{0.592} \tag{3.12}$$

3.5 Stepped spillway relation of Boes and Hager (2003)

Boes and Hager (2003) studied slopes of 30, 40 and 50 º (1V:1.73H, 1V:1.19H and 1V:0.84H, correspondingly), three different step heights (s = 23.1, 46.2 and 92.4 mm) and the inflow condition corresponded to a jetbox (pressurized inlet). In the experiments of Boes and Hager (2003), the inception point location was mathematically defined as the first section where bottom air concentration reaches 1 % and roughness Froude number (Eq. 3.9) was defined based on the step height s, instead of k_v. Boes and Hager (2003) also found that this criterion agrees well with visual observations of the inception point at the free surface.

Boes and Hager (2003) proposed an empirical relation for the determination of the inception point location based on large scale laboratory data on stepped spillways. The proposed equation can be written as:

$$L_i = \frac{5.90 h_c^{6/5}}{\sin(\theta)^{7/5} s^{1/5}} \tag{3.13}$$

being h_c the critical depth, which can be computed as $\sqrt[3]{q^2/g}$ (Chanson, 2004). Substituting h_c into Eq. 3.13, a relation in the form of previous studies can be obtained (Bung, 2009):

$$\frac{L_i}{k_v} = \frac{5.90\,(\mathrm{F}_{*,\mathrm{v}})^{0.8} \cos(\theta)^{0.2}}{\sin(\theta)} \tag{3.14}$$

The equation proposed by Boes and Hager (2003) remains valid for slopes ranging from 26 º to 75 º and yields a prediction similar to the expression of Chanson (1994b) and, consequently, to the one proposed by Chanson (2002).

3.6 Stepped spillway relation of Bung (2009)

Bung (2009) reported a wide range of air-water flow properties for stepped spillways at both the non-uniform and uniform regions. The inception point was defined as the first section where the mean air concentration reached a value of C_m = 20 %. For the

estimation of the inception point location, the following equation was proposed:

$$\frac{L_i}{k_v} = 5.24\,\mathrm{F}_{*,\mathrm{v}} - 3.72 \tag{3.15}$$

and for the flow depth at the inception point location:

$$\frac{\overline{h}_i}{k_v} = 0.085\,\mathrm{F}_{*,\mathrm{v}} - 0.338 \tag{3.16}$$

Expressions were fitted to data obtained in stepped spillways with slopes of 1V:3H and 1V:2H and two step heights (s = 30 and 60 mm). Roughness Froude number ranged from 2 to 13.

3.7 Stepped spillway relation of Amador et al. (2009)

Amador et al. (2009) studied the development of the boundary layer over a stepped spillway (1V:0.8H slope, step height s = 50 mm), providing an expression for the inception point location as the intersection of the boundary layer with the free surface. Amador et al. (2009) proposed:

$$\frac{L_i}{k_v} = 5.982\,\left(\mathrm{F}_{*,\mathrm{v}}\right)^{0.840} \tag{3.17}$$

and for the water depth:

$$\frac{\overline{h}_i}{k_v} = 0.385\,(\mathrm{F}_{*,\mathrm{v}})^{0.580} \tag{3.18}$$

3.8 Stepped spillway relation of Meireles et al. (2012)

The empirical study of Meireles et al. (2012) focused on the non-aerated region of a stepped spillway with a slope of 1V:0.75H, with steps of s = 20, 40 and 80 mm. The inception point location was defined as (Meireles et al., 2012): "*the observed vertical edge immediately upstream of the step cavity where a continuous presence of white water or air bubbles was noticed from above and also through both side walls along the entire flume width*".

Meireles et al. (2012) proposed the following simple empirical expression for the clear water length:

$$\frac{L_i}{k_v} = 6.75\,(\mathrm{F}_{*,\mathrm{v}})^{0.76} \tag{3.19}$$

and for the depth at the inception point location:

$$\frac{\overline{h}_i}{k_v} = 0.35\,(\mathrm{F}_{*,\mathrm{v}})^{0.59} \tag{3.20}$$

3.9 Stepped spillway relation of Hunt and Kadavy (2013)

The study of Hunt and Kadavy (2013) proposed two relationships for flat to mildly slopped stepped spillways ($\theta \leq 26^{\circ}$), with the following one for the lower range of roughness Froude numbers ($0.1 < \mathrm{F}_{*} \leq 28$):

$$\frac{L_i}{k_v} = 5.19\,(\mathrm{F}_{*,\mathrm{v}})^{0.89} \tag{3.21}$$

and a similar expression for the higher range of roughness Froude numbers ($28 < \mathrm{F}_{*,\mathrm{v}} \leq 10^5$):

$$\frac{L_i}{k_v} = 7.48\,(\mathrm{F}_{*,\mathrm{v}})^{0.78} \tag{3.22}$$

The considered step heights comprehended $s = 19$ and 40 mm, and the spillway inlet consisted of a broad crested weir. In Hunt and Kadavy (2013), the surface inception point was observed visually and recorded photographically. More specifically, the inception point location was determined as the point where white water first appeared across the full width of the free surface.

3.10 Stepped spillway relation of Chanson et al. (2015)

In the new IAHR Monograph of Chanson (2015), a complete chapter was devoted to the reanalysis of experimental data on stepped spillways. In that chapter, Chanson et al. (2015) proposed an empirical relation similar to Chanson (1994b):

$$\frac{L_i}{k_v} = 9.8719 \sin(\theta)^{0.0796} (\mathrm{F}_{*,\mathrm{v}})^{0.713} \tag{3.23}$$

and for the flow depth at the inception point section:

$$\frac{\overline{h}_i}{k_v} = \frac{0.4034}{\sin(\theta)^{0.04}} (\mathrm{F}_{*,\mathrm{v}})^{0.592} \tag{3.24}$$

It is also discussed by Chanson et al. (2015) that for the flow with a gated or pressurized intake, other formulations become necessary due to a different growth of the boundary layer.

Chapter 4

Numerical studies

4.1 General remarks

Numerical modelling has attracted more attention in the recent past as it allows great flexibility in the study of complex hydraulic problems. Whereas a physical laboratory requires large facilities and costly instrumentation, sufficient computing capacity is readily available in most universities and research centres and some numerical codes can be found freely accessible.

Numerical studies on hydraulic structures have benefited from past experiences of aeronautic' and computer scientists' communities with Computational Fluid Dynamics (CFD). However, as opposed to physical modelling, it cannot be considered a mature discipline and sometimes caution must be taken in the

interpretation of results. The numerical study of common environmental fluid mechanics and hydraulic structure flows present some particular characteristics when compared to other communities' use of CFD: scales range from millimetres to kilometres and turbulence is often accepted as a favourable factor, as opposed to the unwanted drag in aerodynamic studies (Blocken and Gualtieri, 2012). Applications where turbulence is oftentimes desired are energy dissipaters or contaminant mass transport.

In monophasic flows, the smaller scales involved in the shear flows impose a constraint on the necessary cell resolution of Direct Numerical Simulations (DNS) or limit the validity of Large Eddy Simulations (LES). Reproducing these flow structures is generally impossible and, according to NASA surveys (Slotnick et al., 2014), an engineering solution is still usually preferred by a great part of the modellers, which propitiates the use of the Reynolds-Averaged Navier-Stokes (RANS) equations. Therefore, the effect of the smallest eddies generated in the shear regions is not necessarily captured by the simulations, but it is the input of a semi-empirical model that is better known as turbulence model.

Literature is rich in examples of applications of various turbulence models, with thorough analysis on their strengths and limitations. Some notable works are: the development of the most commonly used two-equations turbulence models, such as the $k-\varepsilon$ model of Launder and Spalding (1974), the RNG $k-\varepsilon$ model of Yakhot et al. (1992) or the $k-\omega$ model of Wilcox

(2006) and Wilcox (2008), the shear-stress transport model of Menter (1994), the one-equation turbulence model of Spalart and Allmaras (1994), the best practices and general CFD knowledge studies of Bradshaw et al. (1996) and Spalart (2000), the turbulence modelling IAHR monograph of Rodi (1993), the book of Pope (2000) on fluid mechanics and general CFD, the books on numerical methods in CFD of Hirsch (2007) and Versteeg and Malalasekera (2007), the IAHR monograph on LES of Rodi et al. (2013), the more specialized books of Ishii and Hibiki (2010) on modelling of multiphase flows, Prosperetti and Tryggvason (2009) on numerical methods applied to multiphase flows modelling and the keynote address of Bombardelli (2012) dealing with fundamental and applied aspects of the numerical modelling of air-water flow mixtures in hydraulic engineering.

When dealing with the necessary resolution, the approach presented by Fuster et al. (2009) on the octree adaptive mesh refinement is remarkable. The spatial resolution increases close to the interfaces and zones of large vorticity allowing better capture of atomization. An example of the capabilities of this method can be found in the breaking waves work of Deike et al. (2015). Another approach which is of great interest for free surface flows where there is small interaction with the air phase, is the one-fluid formulation, given its simplicity and efficiency[1].

[1]Further description can be found in the Chapter 3 of Prosperetti and Tryggvason (2009).

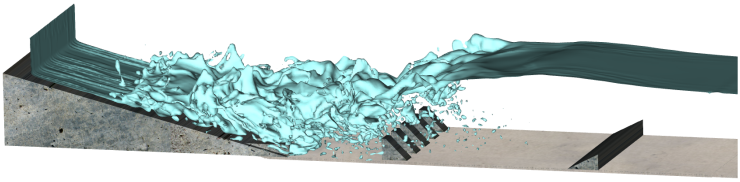

Fig. 4.1 Numerical simulation of a USBR type III stilling basin. Supercritical flow (inlet Froude number F_1 = 6.37). Geometry based on the study of Valero et al. (2018b). Flow from left to right, no turbulence model used.

Figure 4.1 shows an example of bubbles reproduced by a single-phase Volume of Fluid (VOF) model (Hirt and Nichols, 1981) where the cell size limits the air-water flow structures reproduced, as aeration at the basin end could be expected to be higher, spanning at least to the end of the basin.

4.2 Direct Numerical Simulation

In turbulence research, the search for better turbulence models and better parametrization of the flows has driven most of the efforts and, in this regard, DNS has proven to be useful, being capable of complementing the largely accepted experimental research since the early 1970's (Moin and Mahesh, 1998).

A DNS is often referred to as an unsteady simulation where all continuum length and time scales are fully resolved (Prosperetti and Tryggvason, 2009). In addition to fully resolving the turbulence spectra (up to the Kolmogorov scale), a DNS which aims to reproduce air entrainment can be bounded by the bubble scales; despite they should be clearly greater than the smaller turbulence scales.

A DNS usually reproduces extremely simple geometries (e.g., wall bounded flows or a group of a few droplets or bubbles) but, nonetheless, allows extremely accurate solutions. Many questions that need to be addressed are not likely to be explained solely by means of experimental modelling due to practical limitations, as for instance the inability to access the flow field in between the bubbles. Hence, DNS become a tool of utmost interest.

An example is the experimentally observed fact that in smooth spillways, with increasing air concentration, drag reduction takes place (Chanson, 1994a; Wood, 1983). The DNS of Lu et al. (2005) showed that deformability of bubbles is of extreme relevance for this phenomenon. Bubbles of sizes comparable to the buffer layer lead to reduction of wall drag as a result of the suppression of the streamwise vorticity. Spacing of the streamwise vortices also affected the changes that a bubble produced in the turbulence characteristics. However, for the numerical case of less deformable bubbles, drag increased resulting from the

interaction with the viscous layer. Less deformable bubbles were numerically achieved using an unphysical surface tension value (Lu et al., 2005).

Recently, Mortazavi et al. (2016) presented the first DNS of a hydraulic jump at low Froude number and low Reynolds number (F_1 = 2, R = 11,000) with no boundary layer considered in the inlet flow (uniform velocity for the inlet water phase). Their study allowed insight into the energy transfer processes, yielding better understanding of the energy dissipating properties of the jump. Additionally, Mortazavi et al. (2016) observed a strong connection between the vortex shedding process and the air entrainment mechanism, resulting in a quasiperiodic phenomenon with a distinctive frequency. This highlights the relevance of experimental studies focusing on hydraulic jump frequencies as Zhang et al. (2013), Wang and Chanson (2015) and Montano et al. (2018) to better understand the air entrainment process.

Mortazavi et al. (2016) also allowed some insight on scale effects affecting air entrainment by modelling the same hydraulic jump with the same flow parameters, except for the Reynolds number (R = 5,000 and 11,000). Despite the limited Reynolds number range, this type of information might be priceless for the study of scale effects. Mortazavi et al. (2016) also showed that the highest dissipation occurs at the jump impingement.

4.3 Large Eddy Simulation

A LES directly computes the large (energy containing) scales while approximating the influence of the smaller ones (Labourasse et al., 2007). It represents an intermediate approach between DNS and RANS, thus allowing great insight in problems with larger characteristic scales. In the case of LES, various hydraulic studies have been conducted (Rodi et al., 2013). In terms of air-water flow research, the main efforts have been done in coastal applications. Christensen and Deigaard (2001) simulated breaking waves using a LES approach and Lubin et al. (2006) first used LES to thoroughly study the air entrainment occurring in plunging breaking waves. Bung et al. (2009) compared LES and RANS to experimental data of breaking waves, finding better agreement for the LES approach. Lubin et al. (2010) studied the two-phase tidal bore motion, comprehending the free surface dynamics and the inside flow structure and, recently, Lubin and Glockner (2015) studied air fingers appearing under breaking waves, proposing a compelling explanation to a phenomenon observed singularly in nature.

4.4 Reynolds Averaged Simulation

RANS modelling corresponds to a different philosophy than the previously discussed approaches. The RANS approach allows

simulation of larger domains with cell sizes that could only solve the main flow structure. Dependence on the turbulence model is often critical but, in turn, engineering problems can be handled. For flows not strongly affected by viscous effects, solutions can also be insensitive to the turbulence model and including the three-dimensionality of the flow may suffice to allow accurate estimations (Crookston et al., 2018).

Likewise a turbulence model in RANS simulations, a sub-grid air entrainment model can be used to overcome some of the air-water flow prediction deficiencies. However, while the structure of a boundary layer is well-known, the structure of a uniformly aerated flow (representing the equivalent example of simple air-water flow) is still under discussion. Deeper understanding and improved description of air-water flows are still necessary to allow accurate modelling. Additionally, when calibrating or using a sub-grid air entrainment model, proper mesh sensitivity analysis arises as a critical issue (Castro and Carrica, 2013; Valero and García-Bartual, 2016). These models' outputs usually depend non-linearly upon turbulence quantities which exhibit a slower convergence than depths or velocities, as they are connected to the velocity gradients. Mesh sensitivity analysis as recommended by the American Society of Mechanical Engineers (ASME) by Celik et al. (2008) would be preferable, allowing computation of the numerical uncertainty of the variable under study.

Hydraulic jumps have been the object of numerical studies. Carvalho et al. (2008) reproduced the overall structure of a jump using a 2D approach and Witt et al. (2015) studied three Froude numbers in 2D and one in 3D, allowing insight on the necessary resolution to observe aeration. Ma et al. (2011) presented an analysis of a $F_1 = 1.98$ hydraulic jump using both RANS and a hybrid RANS-LES model (Detached Eddy Simulation, DES) coupled with an air entrainment routine. Ma et al. (2011) found better agreement with experimental data for the DES and argued that it is due to the better capture of the jump wave oscillations. The RANS model, otherwise, only reproduced well the lower region of the jump. Bayon et al. (2016) presented a comparison of two CFD packages using two-phase flow RANS modelling and the RNG $k-\varepsilon$ turbulence model. No discussion was presented in terms of aeration; however, Bayon et al. (2016) compared the main mean flow variables of a hydraulic jump with $F_1 \approx 6$ to experimental data and empirical relations, obtaining accuracy levels over 90 % for all of them excepting the roller (recirculation) length, that remained around 80 %. Bayon et al. (2016) also detected a characteristic frequency of the jump toe, similarly to the DNS study of Mortazavi et al. (2016) and numerous previous experimental evidences.

Spillway simulations have been conducted since the studies of Caisley et al. (1999), Ho et al. (2001) and Savage and Johnson (2001), more than 15 years ago, with research activity considerably growing during the recent years. In this type of

flow, the non-aerated region can be predicted reasonably well (Bombardelli et al., 2011; Savage and Johnson, 2001; Toro et al., 2017; Valero and Bung, 2015; Valero et al., 2018b).

Valero et al. (2018b) analysed velocity distributions resulting from RANS modelling over smooth and stepped spillways in the non-aerated region and compared them to experimental data (Fig. 4.2). Figure 4.2 (top) includes the numerical data of Valero et al. (2018b) and the experimental data from Bauer (1951) for different smooth chute slopes, with best fit for the power law exponent of $n = 4.5$; $n = 6$ is a commonly accepted value and therefore has been included as a reference profile. Castro-Orgaz (2010) noted that $n = 6.3$ is a good fit for the prototype data of Cain and Wood (1981). Data of Bormann (1968) for a slope of 1.5H:1V show a similar shape. A thorough analysis and discussion of these data is provided by Castro-Orgaz (2010).

Figure 4.2 (bottom) presents the numerical results of Valero et al. (2018b) for the velocity profiles over stepped chutes. The experimental data (detailed PIV study) of Amador et al. (2006) were included for the flow above the step edges (E) and above the step niches (N, in the middle of two edges). The Amador et al. (2006) edge (E) data fit $n = 3$. Step edge inlet velocity data of Meireles and Matos (2009) were measured using a Pitot-Prandtl tube and best fit corresponds to $n = 5.1$. For completeness, data of Zhang and Chanson (2016b) were also considered, which were obtained over the step edges using Pitot-Prandtl tubes. These

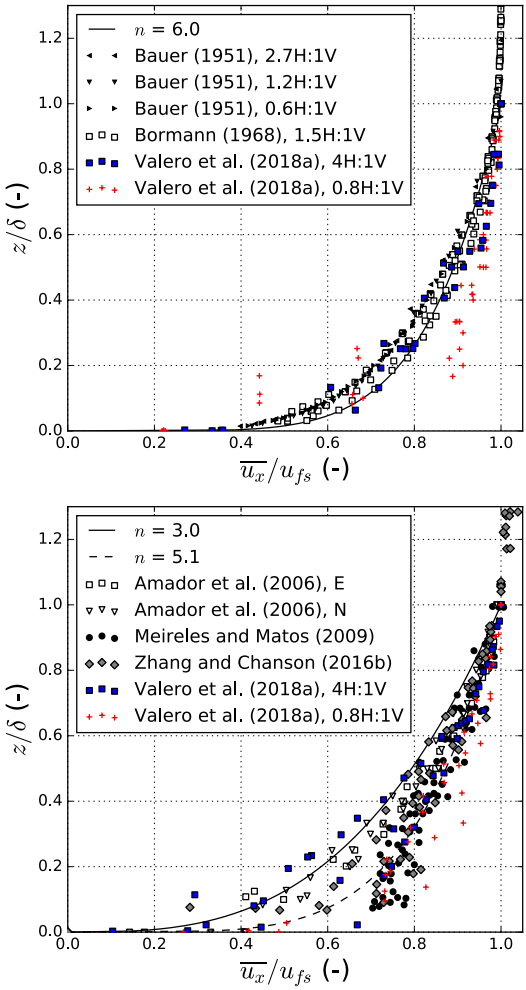

Fig. 4.2 Smooth (top) and stepped (bottom) spillway velocity profiles from experimental (Amador et al., 2006; Bauer, 1951; Bormann, 1968; Meireles and Matos, 2009; Zhang and Chanson, 2016b) and numerical (Valero et al., 2018b) studies. Power law profiles with different n values for reference.

data best fit $n = 4.5$. All data considered in Fig. 4.2 correspond to data gathered in the non-aerated region of the spillways.

In both smooth and stepped spillways, the numerical results of Valero et al. (2018b) for the slope θ = 4H:1V agreed most favourably with experimental data from the milder slope cases. A least squares fitting reveals that $n = 5.85$ best fits the numerical data for smooth spillways ($n = 5.87$ for θ = 0.8H:1V but with considerably larger scatter, see Fig. 4.2 top). For the stepped spillway cases, $n = 4.03$ was obtained for θ = 4H:1V and $n = 7.02$ for θ = 0.8H:1V, which also shows larger deviation from experimental results.

A RANS study on the determination of the inception point location in a stepped spillway was first conducted by Bombardelli et al. (2011) using a 2D RANS model coupled with a sub-grid air entrainment routine presented by Hirt (2003) and Souders and Hirt (2004), finding good agreement with physical modelling observations. Valero and García-Bartual (2016) calibrated the air entrainment model of Hirt (2003) with over 200 simulations on smooth steep spillways, also finding good agreement for the diffusive air concentration profile. Validation was performed by reducing the spillway slope, obtaining reasonable agreement for the mean air concentration trend. Valero and Bung (2015) extended the study of Bombardelli et al. (2011) to 3D, highlighting that large free surface roughness (probably linked to the cavity flow structures) was well reproduced in addition to the inception

point location. However, Valero and Bung (2015) found that the resulting air concentrations were unrealistic.

Sub-grid scale models have been used to reproduce aeration in other types of air-water flows. Ma et al. (2010) studied the aeration in a plunging jet using their sub-grid air entrainment model. Carrica et al. (1999), Moraga et al. (2008) or Ma et al. (2011) are examples of sub-grid air entrainment modelling for the simulation of the air-water flow occurring in waves and wakes around and behind ships. Different approaches to predict the effect of the dispersed phase into the carrier phase can be found in Ishii and Hibiki (2010).

4.5 Other numerical approaches

Meshless methods represent an approach different to those used in all of the aforementioned studies. For these type of methods, the free surface becomes a natural output and no additional methods – as for instance the VOF – are necessary to track it. Two particular methods may be mentioned: the Smoothed Particle Hydrodynamics (SPH) and the Lattice-Boltzmann Method (LBM).

The SPH method is fully Lagrangian and it is subtended over the original contributions of Gingold and Monaghan (1977) and Monaghan (1994). It has experienced a comparably larger activity than other meshless methods. A thorough description on

the SPH method can be found in the specialized book of Violeau (2012). Some recent studies using the SPH method include the stepped spillway modelling of Wan et al. (2017) and Husain et al. (2014), and the hydraulic jump models of De Padova et al. (2017, 2013) and López et al. (2010). A recent review can be found in Violeau and Rogers (2016).

LBM rely on the lattice-Boltzmann equation and some defined particle interactions. Reviews on this method can be found in Chen and Doolen (1998) and Aidun and Clausen (2010). One appealing aspect of meshless methods is the easiness of parallelization due to the explicit nature of most methods, allowing the use of Graphic Computing Units to speed the computations.

The Particle Finite Element Method (PFEM) tries to combine the natural suitability of meshless methods for free surface flows with the Finite Element Method which, however, still requires a mesh. With the PFEM method (Idelsohn et al., 2004; Oñate et al., 2004), particles or nodes are moved but internally a mesh is used to discretize the flow equations. These nodes can however separate from the main flow, thus representing droplets. The included FEM formulation makes it inherently useful for fluid-soil-structure interactions (Oñate et al., 2011). The simulation of simple bubble dynamics can be found in Mier-Torrecilla et al. (2011) and Mier-Torrecilla (2010). An example of a highly aerated flow using the PFEM method can be found in the bottom outlet study of Salazar et al. (2017).

Partial conclusions

Part I was made of four Chapters, which aimed to introduce this dissertation and put it in the general context of past research. In Chapter 1, a critical historic analysis on self-aeration research was presented, starting with the study of Ehrenberger (1926) and advancing up to the most recent developments. Main goals of this dissertation were presented as well. In Chapters 2, 3 and 4, literature review of fundamental, experimental and numerical advances was presented. Focus on studies directly dealing with self-aeration onset determination was preferred, despite other relevant air-water flow milestones were covered as well. The lack of an undisputed, physically based general method for the determination of self-aeration in practical problems has been the motivation of this thesis.

Part II

Non-aerated region

Chapter 5

Non-aerated flow

5.1 Smooth spillway hydrodynamics

5.1.1 Mean flow

Stagnant water in the reservoir is accelerated in the spillway due to gravity. A revision of prototype data of turbulent velocity profiles and boundary layer growth can be found in Castro-Orgaz (2010). The time-averaged streamwise velocity profile ($\overline{u}_x$)[1] of a turbulent boundary layer can be well explained by a wall-wake model (Pope, 2000; White, 2006):

[1] In this chapter, in order to keep subscripts short, the velocity in the streamwise direction is denoted as u_x when it corresponds unmistakably to the water velocity. In the case of ambiguity, $u_{w,x}$ will be used for the water velocity and $u_{a,x}$ for the air velocity.

$$\frac{\overline{u}_x}{u_*} = \frac{1}{\kappa}\ln\left(\frac{z}{k_s}\right) + B + \frac{1}{\kappa}(1+6\Pi)\left(\frac{z}{\delta}\right)^2 - \frac{1}{\kappa}(1+4\Pi)\left(\frac{z}{\delta}\right)^3 \tag{5.1}$$

where u_* is the shear velocity, $\kappa = 0.41$ is the von Kármán constant, B is a constant ($B = 8.5$ for rough wall), k_s is the equivalent roughness height, δ is the boundary layer thickness which represents $z = z(u = 0.99\,u_{fs})$, with u_{fs} the free stream velocity, and $\Pi = 0.2$ is the wake strength parameter determined by Castro-Orgaz (2010) by fitting prototype scale data. In accelerating flows, Π commonly takes a value between 0 and 0.4 (White, 2006). Further considerations on logarithmic velocity profiles can be found in the study of Auel et al. (2014).

For the boundary layer growth, the momentum relation after von Kármán (1921), can be written as:

$$\frac{C_f}{2} = \frac{\mathrm{d}\theta_m}{\mathrm{d}x} + (2+S^*)\,\frac{\theta_m}{u_{fs}}\,\frac{\mathrm{d}u_{fs}}{\mathrm{d}x} \tag{5.2}$$

where C_f is the skin friction coefficient, defined as:

$$C_f = \frac{\tau_0}{1/2\,\rho\,u_{fs}} \tag{5.3}$$

with τ_0 the wall shear stress, and the shape factor is defined as:

$$S^* = \delta^* / \theta_m \tag{5.4}$$

The shape factor can also serve to identify the separation point in a boundary layer flow. The displacement thickness is defined as:

$$\delta^* = \int_0^\delta \left(1 - \frac{\overline{u}_x}{u_{fs}}\right) \mathrm{d}z \tag{5.5}$$

and the momentum thickness is defined as:

$$\theta_m = \int_0^\delta \frac{\overline{u}_x}{u_{fs}} \left(1 - \frac{\overline{u}_x}{u_{fs}}\right) \mathrm{d}z \tag{5.6}$$

For any type of spillway, the free stream velocity u_{fs} can be accurately computed assuming irrotational flow (Castro-Orgaz and Hager, 2010).

Non-null spanwise ($\overline{u}_y$) and normalwise ($\overline{u}_z$) velocities can appear, especially in narrow flumes (width to depth ratios below 5), as a result of secondary currents (Auel et al., 2014). In narrow flumes, the dip phenomenon can cause a decrease in the depth location for the maximum flow velocity (Auel et al., 2014).

5.1.2 Turbulence intensities

Intense velocity fluctuations occur in any turbulent boundary layer, thus resulting in significant mass, momentum and energy fluxes in all three dimensions, despite the essentially one dimensional nature of the flow. Under certain conditions, classic boundary layer data match reasonably well the flows occurring over smooth spillways (see experimental study of Auel et al., 2014). Velocity fluctuations are generated in the inner layer – due to the shearing with the wall – and thus, proper scaling is achieved using the shear velocity u_*, which is a stress in velocity dimensions.

Many studies have been conducted since the early work of Klebanoff (1955). Some are noteworthy, as for instance the Laser Doppler Anemometry (LDA) study of Nezu and Rodi (1986), covering both sub- and supercritical flows, the study of Auel et al. (2014) covering Froude numbers up to 6.1 and the influence of the flume relative width, and the long sampling time (2 h) stereoscopic Particle Image Velocimetry (PIV) study of Cameron et al. (2017).

Nezu (1977) proposed a semi-empirical relation for the stream-, span- and normalwise velocity fluctuations of the form:

$$\frac{\sqrt{\overline{u_i' u_i'}}}{u_*} = D_i \exp\left(-K_i \frac{x_i}{\delta}\right) \tag{5.7}$$

with the subscript i denoting the streamwise (x), the spanwise (y) and the normalwise (z) fluctuations[2]; D_i and K_i are model coefficients. Studies on non-uniform open channel flows suggest that coefficients of Eq. 5.7 are not constant but vary with the acceleration of the flow (Auel et al., 2014; Kironoto and Graf, 1995). Parameters D_i represent a virtual peak that the normal stresses profiles would show at $z/\delta = 0$. Evidently, this is physically meaningless as the profiles must necessarily satisfy $u_i' = 0$ at the solid contour.

Turbulent velocity fluctuations change abruptly in the near wall region, with a peak at around $z/\delta \approx 0.04 - 0.12$ (Dey, 2014), more noticeable for the streamwise velocity fluctuation. This peak value is well-known to be affected by the Reynolds number (Hoyas and Jiménez, 2006; Jiménez, 2018). The presence of the wall affects the fluctuations, leading to anisotropy which is typical of all shear flows (White, 2006).

The streamwise fluctuation is the most energetic term, being unimpeded by the wall and slightly reinforced by the free stream flow. The normalwise component, however, is the smallest term being subject to blockage by the wall. The spanwise component represents an intermediate case between streamwise and normalwise fluctuations.

Several authors have fitted coefficients D_i and K_i to empirical data, as shown in Table 5.1. Most of them did not study

[2]Coordinate system coherent with previous chapters, see Fig. 2.1.

velocity fluctuations in the spanwise coordiante, which would require special experimental arrangements or equipment such as stereoscopic PIV or Acoustic Doppler Velocimeters (ADV). For this component, Nezu (1977) suggested $D_y = 1.63$ and $K_y = 1.00$. The hypothesis of Nezu (1977) on coefficients $K_i = 1.00$ for all three components implies that the same degree of anisotropy prevails over the boundary layer depth, which is unrealistic.

Table 5.2 includes the best fitting coefficients for Eq. 5.7 based on the data of Cameron et al. (2017), given the exceptional characteristics that this dataset holds. Parameters fitting has been done only using data of $0.10 < z/\delta < 0.90$ to avoid including peak values or estimations disturbed by the free surface. For completeness, uncertainty bounds and coefficient of determination are presented as well. Note that both stream- and spanwise components present a slightly superior fitting quality than normalwise fluctuations. This could be due to the bounding effect of the wall, altering the nature of vertical velocity fluctuations and adequacy of Eq. 5.7.

The study of Cardoso et al. (1989) covered low Froude numbers (maximum of 0.21, based on the depth averaged velocity). Kironoto and Graf (1994) studied turbulence quantities in rough[3], uniform open channel flows with submergence up to $k_s/\overline{h} = 0.1$.

[3]The submergences of the studies of Kironoto and Graf (1994) and Dey and Raikar (2007) fall well below common submergences of stepped spillways.

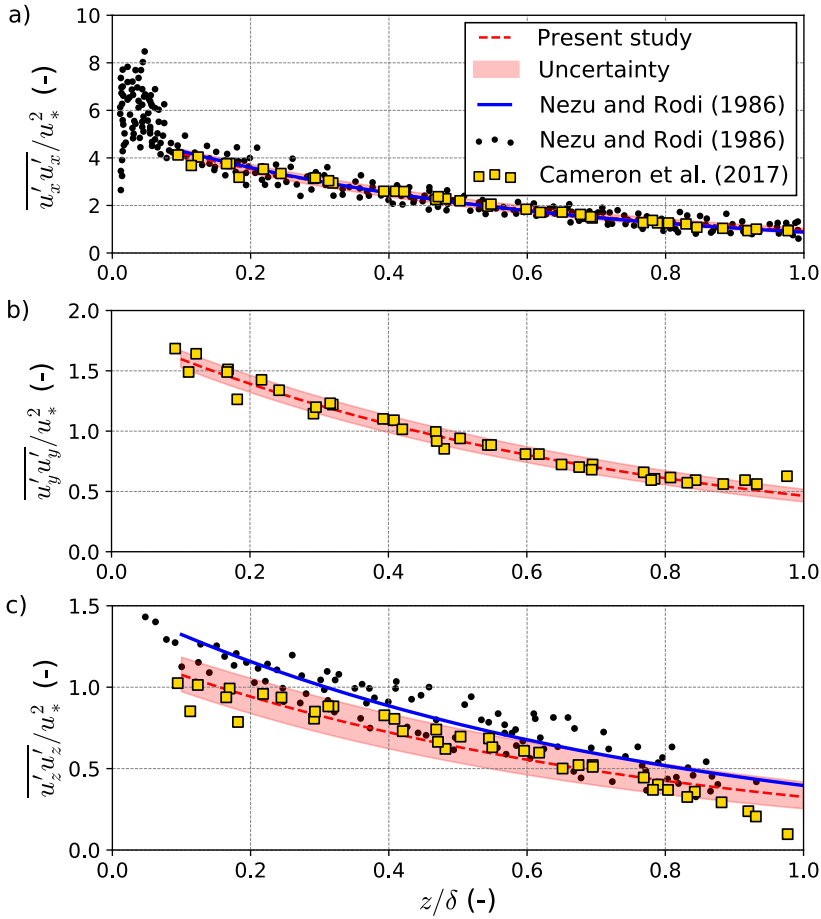

Fig. 5.1 Normal stresses in boundary layer flows over rough channel bed. Exponential fit (Eq. 5.7) with coefficients of Table 5.2 ("present study" and "uncertainty") and Nezu and Rodi (1986) (blue solid line).

Table 5.1 Empirical coefficients of Eq. 5.7, best fit from different experimental studies.

	Streamwise		Normalwise	
Study	D_x	K_x	D_z	K_z
Nezu (1977)	2.30	1.00	1.27	1.00
Nezu and Rodi (1986)	2.26	0.88	1.23	0.67
Cardoso et al. (1989)	2.28	1.08	–	–
Kironoto and Graf (1994)	2.04	1.14	0.97	0.76
Dey and Raikar (2007)	2.07	1.17	0.95	0.69

Table 5.2 Best fitting coefficients of Eq. 5.7 to data of Cameron et al. (2017). Minimum and maximum values correspond to 95 % uncertainty bounds. Coefficient of determination r_d^2 for the obtained coefficients.

	Streamwise		Spanwise		Normalwise	
	D_x	K_x	D_y	K_y	D_z	K_z
Best fit	2.222	0.837	1.354	0.688	1.108	0.663
Minimum	2.181	0.796	1.329	0.650	1.063	0.578
Maximum	2.264	0.877	1.378	0.726	1.153	0.747
r_d^2	0.983		0.978		0.898	

Dey and Raikar (2007) extended that study by covering submergences up to 0.15.

Predictions of Eq. 5.7 with the coefficients suggested by Nezu and Rodi (1986) and those obtained in Table 5.2 are presented in Fig. 5.1. Data of Nezu and Rodi (1986) and Cameron et al. (2017) are in good agreement for the streamwise component, but differences appear for the normalwise velocity fluctuation. It is here suggested that data of Cameron et al. (2017) may hold a lower noise level, which results in a smaller variance of the instantaneous velocities and, hence, in a lower turbulence intensity estimation.

5.2 Stepped spillway skimming flow hydrodynamics

5.2.1 Mean flow

For stepped spillways, detailed description as that provided by Castro-Orgaz (2010) is not available. Additionally, large scatter is found for the velocity exponent of the power law velocity profile across different studies. The high submergence ratios (k_s/δ or k_v/δ), which remain well above other types of flows, make stepped spillway hydrodynamics difficult to predict through open channel flow classic literature.

Table 5.3 Flow conditions corresponding to the study of Valero et al. (2018d).

q (m$^2/s$)	$\overline{h}$ (m)	δ (m)	u_{fs} (m/s)	u_* (m/s)	C_f (-)
0.0345	0.15	0.15	0.3455	0.1014	0.172
0.0517	0.15	0.15	0.5354	0.1490	0.155
0.0862	0.13	0.13	0.9293	0.2238	0.116
0.1207	0.16	0.09	0.9472	0.2009	0.090

The previous Particle Image Velocimetry (PIV) study of Amador et al. (2006), for a stepped spillway (with slope of 1.25V:1H), investigated thoroughly the flow structure over a stepped cavity in the non-aerated region. Flow velocities over a stepped cavity (at least both over niches and edges) in the aerated region of stepped spillways can be found in the studies of Bung (2009), Bung (2011), Felder and Chanson (2011), Bung and Valero (2015), Bung and Valero (2016b), Zhang and Chanson (2016c) and Zhang and Chanson (2018).

For the non-aerated region, the study of Amador et al. (2006) also presented velocity fluctuations. Direct velocity fluctuations in the aerated region were first reported by Bung and Valero (2016a) and Zhang and Chanson (2018). Indirect turbulence intensity estimations were previously conducted by Chanson and Toombes (2002) using a technique based on the shape of the cross-correlation of phase detection probe's signals.

Table 5.4 Flow parameters of the study of Valero et al. (2018d).

q (m$^2/s$)	$k_v/\overline{h}$ (-)	k_v/δ (-)	F (-)	R (-)
0.0345	0.593	0.593	0.3455	34,500
0.0517	0.593	0.593	0.5354	51,700
0.0862	0.677	0.677	0.9293	86,200
0.1207	0.563	0.989	0.9472	120,700

The recent study of Valero et al. (2018d) used an ADV Vectrino Profiler to study the non-aerated flow structure over a stepped geometry (2V:1H, for an equivalent stepped spillway flow) installed in a horizontal channel. The main flow conditions are summarized in the Tables 5.3 and 5.4, being q the specific flow rate, $\overline{h}$ the mean flow depth, k_v the cavity depth and δ the boundary layer thickness. Froude (F) and Reynolds numbers (R) were estimated based on the depth averaged velocity. Both δ and the free stream velocity u_{fs} were extrapolated when falling out of the measuring range of the instrumentation while satisfying continuity. Extrapolation was conducted using the mean velocity gradient equation. In Table 5.3, the shear velocity u_* were obtained also via the mean velocity gradient equation by using data covering a complete cavity for $z/\overline{h} > 0.10$.

Figure 5.2 shows the streamwise velocity for the four flow cases contemplated by Valero et al. (2018d), after data filtering as described by Valero and Bung (2018c). The free stream flow can only be clearly observed in Fig. 5.2d; all other flow cases

had the boundary layer thickness too close to the free surface and out of the measuring range of the ADV Vectrino Profiler.

The minimum velocities measured inside the cavity are on average -12.5 % of the free stream velocity u_{fs}, with all four minimum velocities measured falling between $+/-2$ % of -12.0 % of u_{fs}. Closer inspection of the data of Amador et al. (2006) shows that the minimum velocity corresponded to -15 %, -13 %, -16 % and -17 % of u_{fs}. These values are close to the herein reported but slightly greater, which could be explained by the different cavity geometry (1.25V:1H). Note that the data scatter of Amador et al. (2006) is similar to the scatter of the herein presented data.

Flows with gradients in the flow depth or the channel bed can present non-null vertical velocities (Castro-Orgaz and Hager, 2017, pp. 102). In the case studied by Valero et al. (2018d), the cavity produces a clockwise recirculation (Fig. 5.2), which yield non-null vertical velocities. The data shown in Fig. 5.3 correspond to the median normalwise velocity ($\overline{u}_z$). This velocity component cannot be filtered with the mean velocity gradient method proposed by Valero and Bung (2018c). However, a simple spatial median filter with the same window size ($\sim$ 11 mm) suggested by Valero and Bung (2018c) was used.

The minimum and maximum normalwise velocities take place inside the cavity and occur close to the wall, as a jet type flow after the streamwise flow impacts on the opposing cavity

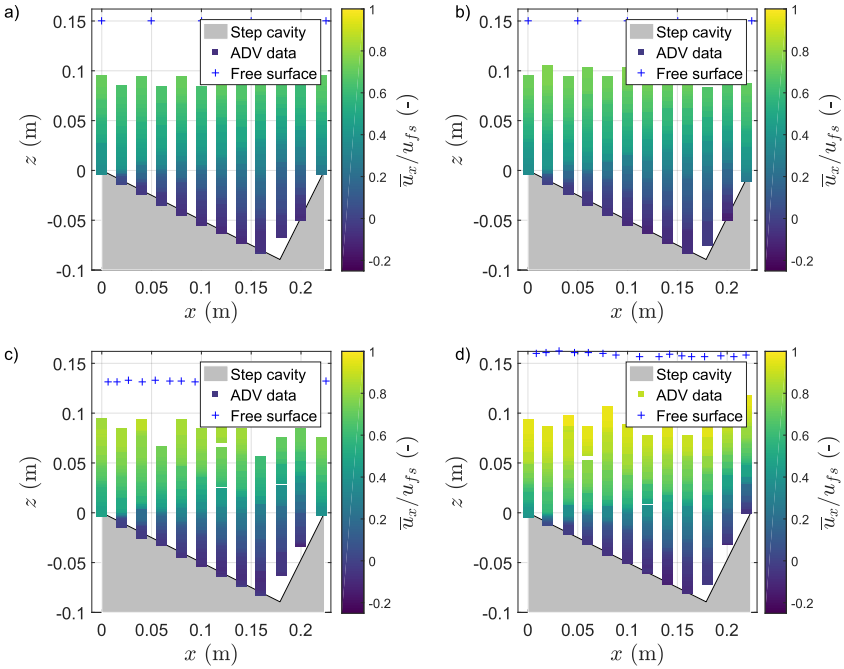

Fig. 5.2 Streamwise velocity in the non-aerated region over a stepped cavity for a) $q = 0.035$ m$^2/s$, b) $q = 0.052$ m$^2/s$, c) $q = 0.086$ m$^2/s$ and d) $q = 0.121$ m$^2/s$. Flow from left to right.

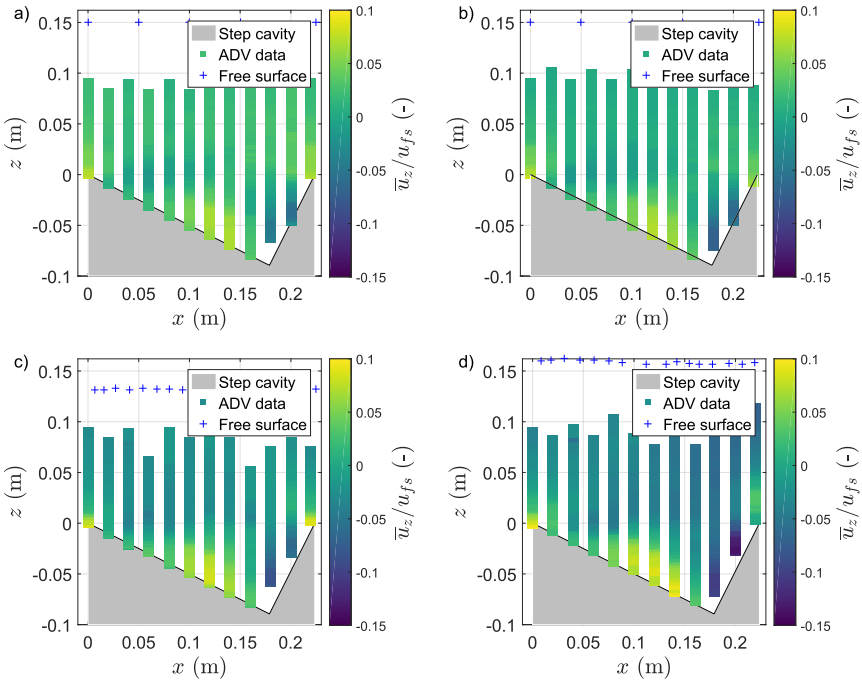

Fig. 5.3 Normalwise velocity in the non-aerated region over a stepped cavity for a) $q = 0.035$ m$^2/s$, b) $q = 0.052$ m$^2/s$, c) $q = 0.086$ m$^2/s$ and d) $q = 0.121$ m$^2/s$. Flow from left to right.

face. The use of the data of a large number of bins around the ADV Sweet-Spot (SS) is of interest to access the velocities closer to the wall. The SS corresponds to the region of best data quality and, expectedly: the farther from the SS, the lower the quality (Brand et al., 2016; Koca et al., 2017; MacVicar et al., 2014; Thomas et al., 2017). A moving spatial median is not applied to these data (differently to the data of Fig. 5.3), hence avoiding the smoothing of the extreme values at the profile ends.

The choice of the extreme velocity values inside the cavity was made based upon the histogram of $\overline{u}_z$ – with data from SS $+/-$ 8 bins, which is the range suggested by Koca et al. (2017) for good quality velocity estimations -– with 100 histogram bins, which allow visual detection of outliers. This estimation may depend upon the number of histogram bins but is more robust than direct (and blind) estimation of the minimum or maximum value of $\overline{u}_z$. Values obtained for the minimum $\overline{u}_z$ corresponded to -11.3 % of u_{fs} and maximum values group around 9.8 % of u_{fs}.

It seems reasonable that the magnitude of the minimum value is larger than that of the maximum value, given that the minimum values are closer to the jet impact on the cavity and follow a more inclined plane (thus the vertical projection is larger). After the impact of the jet on the cavity face, flow acceleration can be observed, which should be accompanied by a local rise of the pressure, as previously observed by Amador et al. (2009)

and Zhang and Chanson (2016b). Jet velocity decay can be also observed inside the cavity (Figs. 5.2 and 5.3), as is typical in turbulent jets (Rajaratnam, 1976); while vertical velocity acceleration is found close to the step edge, where also the maximum flow shearing occurs.

5.2.2 Turbulence intensities

In flows over a rough channel bed, the turbulence intensity is influenced by the boundary roughness close to the wall. With increasing roughness, the streamwise turbulence intensity decreases, transfering some energy to the normalwise turbulence intensity (Dey, 2014). This effect of the boundary roughness disappears in the outer region.

The bed structure of stepped spillways follows a definite pattern, different from that of found on natural streams. Only the previous study of Amador et al. (2006) reported stream- and normalwise velocity fluctuations for a 1.25V:1H cavity geometry in the non-aerated region of a stepped spillway; and Zhang et al. (2016) used a total pressure sensor to estimate the streamwise turbulence in a 1V:1H stepped spillway.

Experimental measurements of Valero et al. (2018d) include instantaneous velocity estimations, which allow direct computation of the normal stresses. The velocity fluctuations have been herein analysed for the cases reported in Tables 5.3 and 5.4. The

resulting profiles have been smoothed with a moving spatial median with a window size of $\sim$ 11 mm. Both the new results and the results of Amador et al. (2006)[4] were used to fit coefficients of Eq. 5.7. The parameters fitting was done using only the data of $0.20 < z/\delta < 0.90$ to avoid including peak measurements or estimations disturbed by the free surface. The coefficients can be found in Tables 5.5 and 5.6. It can be observed in Table 5.6 that, with increasing Reynolds number, the virtual peak (represented by D_i) also increases (see Fig. 5.4). Besides, the data of Amador et al. (2006) show larger velocity fluctuations, yet they remain below data on rough boundary layers (see Table 5.2).

Table 5.5 Empirical coefficients of Eq. 5.7 obtained from data of Amador et al. (2006).

	Streamwise		Normalwise	
R (-)	D_x	K_x	D_z	K_z
110,000	1.638	1.112	0.928	0.7936

It can be observed that the velocity fluctuations grow with increasing Reynolds number, although the trend of D_i stabilizes asymptotically. A function with that behaviour can be written as:

$$D_i = D_{M,i} \tanh\left(\frac{\mathrm{R}}{\mathrm{R}_{76,i}}\right) \tag{5.8}$$

[4]Note that the profiles presented by Amador et al. (2006) were originally dimensionless using the free stream velocity.

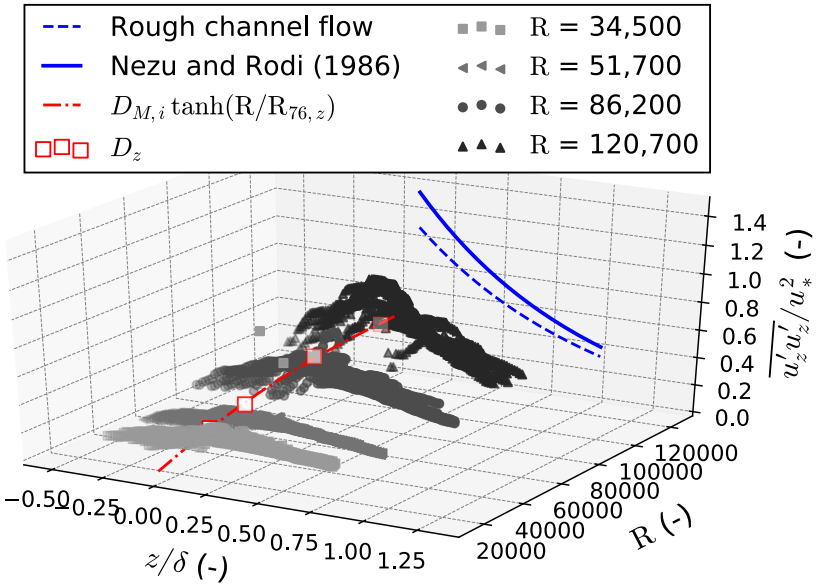

Fig. 5.4 Reynolds scale dependence of the velocity fluctuations in the normalwise direction in flows over a stepped channel bed. Based on the experimental data of Valero et al. (2018d). “Rough channel flow” corresponds to Eq. 5.7 and the coefficients of Table 5.2.

Table 5.6 Empirical coefficients of Eq. 5.7 for flow over stepped macroroughness, obtained from the analysis of data of Tables 5.3 and 5.4.

	Streamwise		Spanwise		Normalwise	
R (-)	D_x	K_x	D_y	K_y	D_z	K_z
34,500	0.303	0.395	0.290	0.446	0.203	0.285
51,700	0.388	0.575	0.365	0.622	0.260	0.444
86,200	0.549	0.713	0.516	0.772	0.385	0.651
120,700	0.571	0.361	0.560	0.487	0.408	0.362

Table 5.7 Fit of $D_{M,i}$ and $\mathrm{R}_{76,i}$ of Eq. 5.8 to experimental data by reducing the Mean Squared Error (MSE).

i	$D_{M,i}$	$\mathrm{R}_{76,i}$	MSE
x	0.609	$6.48 \cdot 10^4$	$1.87 \cdot 10^{-4}$
y	0.596	$6.84 \cdot 10^4$	$1.15 \cdot 10^{-4}$
z	0.445	$7.22 \cdot 10^4$	$1.19 \cdot 10^{-4}$

with i indicating the velocity component, $D_{M,i}$ a parameter which represents the asymptotic value of the fluctuation intensity and $\mathrm{R}_{76,i}$ reproduces the Reynolds number influence. $D_{M,i}$ and $\mathrm{R}_{76,i}$ values have been obtained by reducing the squared differences (Mean Squared Error, MSE). $D_{M,i}$ and $\mathrm{R}_{76,i}$ values are presented in Table 5.7 and the fitting is shown in Fig. 5.5.

It must be noted that the values for the spanwise fluctuation are very similar to those of the streamwise fluctuation, indicat-

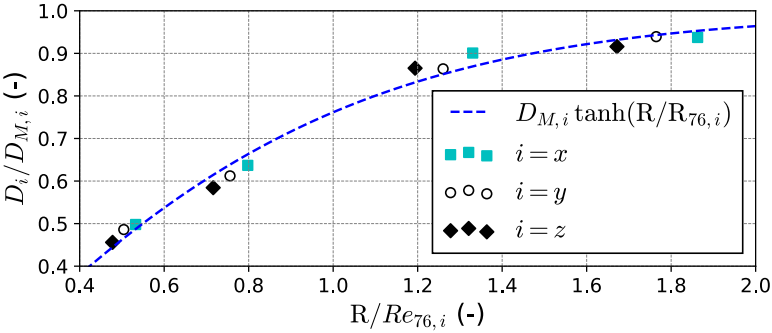

Fig. 5.5 Reynolds number effect on the turbulence intensities over stepped geometries, based on the data of the experimental model of Valero et al. (2018d). Equation 5.8 and parameters from Table 5.7.

ing that transverse fluctuations in stepped spillways can be as energetic as in the stream flow direction. Additionally, this partition of the turbulence kinetic energy is clearly different from that occurring in common rough channel flows. Furthermore, the parameters $\mathrm{R}_{76,i}$ allow the quantification of Reynolds scale effects. For instance, for $\mathrm{R} \approx 1{\cdot}10^5$, which is a well accepted value for Reynolds scale-free models (Boes and Hager, 2003; Kobus, 1984), around 90 % of the maximum velocity fluctuations are present in the flow.

5.3 Interfacial air layer: theoretical considerations

5.3.1 Fundamental evidences

An unbounded air region can be found over the high velocity water region. Between both fluids, an interface exists in the contact surface of both phases. The water flow accelerates due to the gravity, while the velocity (in the x and y directions) at the solid contours is restricted by the no-slip condition. Similarly, the velocity normal to the surface (in the z direction) is also null, as it cannot go through the spillway bed. Thus, all the components of the velocity vector are null: $\mathbf{u}_w(z=0)=0$. These exact mathematical conditions yield a well-known type of flow in fluid mechanics: a boundary layer. The turbulent boundary layer appearing in the water phase due to the existence of solid contours has been discussed in Section 5.1 for smooth spillways and in Section 5.2 for stepped spillways.

Air is in contact with the water region likewise water is in contact with the solid surface. At the surface of contact ($z=h$) between air and water phases, a unique velocity exists for both ($\mathbf{u}_s$, see Fig. 5.6):

$$\mathbf{u}_w = \mathbf{u}_a = \mathbf{u}_s, \qquad \text{at } z = h \tag{5.9}$$

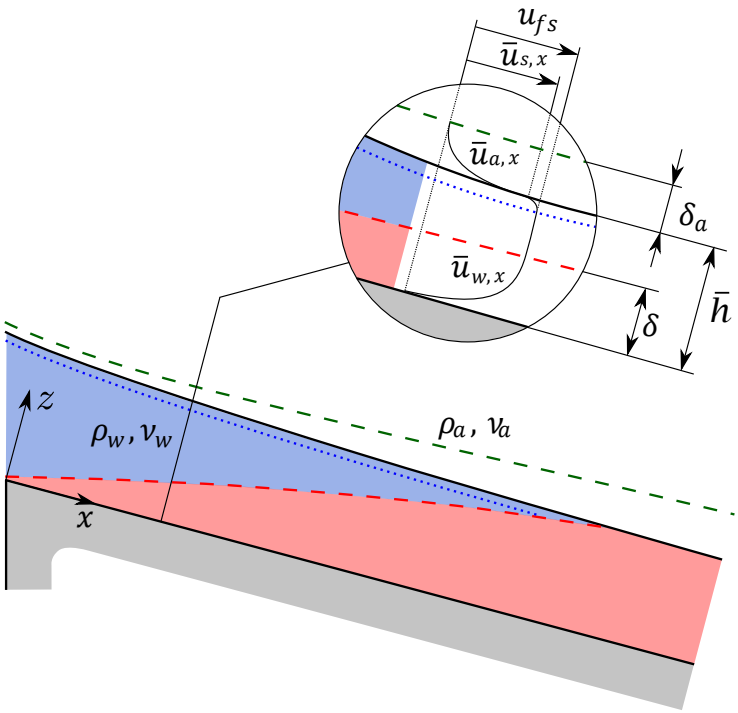

Fig. 5.6 Air and water developing shear layers in a spillway flow.

Water flows at high velocity and as a consequence of the air-water no-slip condition, part of the free stream velocity (u_{fs}) is passed to the air region which, simultaneously, exerts a drag on the water phase, slightly slowing it down in the region closest to the free surface. Applying continuity of stresses at the free surface:

$$\mu_a \frac{\partial u_{a,x}}{\partial z} = \mu_w \frac{\partial u_{w,x}}{\partial z}, \qquad \text{at } z = h \tag{5.10}$$

It is noteworthy that Eqs. 5.9 and 5.10 are formulated in terms of instantaneous variables, but similar reasoning could be conducted for the mean and fluctuating quantities. This type of flow, similar to a boundary layer, is not that well-known. The flow due to the sudden acceleration of a plane is similar to the Stoke's second problem (Landau and Lifshitz, 1987; White, 2006), with a plane oscillating with a certain frequency. However, not much research has been done on that problem and the classic solution is valid only for laminar flows – which is more similar to the shear region generated at the water region (immediately beneath the free surface) due to the velocity difference (between $u_{s,x}$ and u_{fs}) than the boundary layer at the air region. For this water shear region, analogy with the Stoke's second problem can be made and the growth rate can be estimated as (White, 2006):

$$\delta \approx 3.64\sqrt{\nu t} \tag{5.11}$$

with ν the fluid kinematic viscosity and t the time since the start of the plane motion. As the travel time of the water particles at the free surface (t time since they start being accelerated to a given section) is small, δ values of a few millimetres can be expected.

For the interfacial air layer, the difference in velocity between the free surface ($u_{s,x}$) and the air outer edge (null) is considerably larger, and a flow similar to a turbulent boundary layer can be expected, although inverted. Furthermore, the flow acceleration should be similar to that of the spillway's water boundary layer, thus $u_{s,x}(x) \approx u_{fs}(x)$ and therefore the boundary layer pressure gradient; but the roughness of the free surface should be larger than that of a smooth spillway invert.

5.3.2 Implications of its existence: two-phase flow instabilities

When a discontinuity in density, viscosity and/or velocity takes place, Kelvin-Helmholtz instability can appear. This air-water flow instability has been extensively studied since the theoretical works of Helmholtz (1868), Kelvin (1871) and Rayleigh (1878, 1879) on inviscid flows and, above all, the experimental investigations of Reynolds (1883), which initiated the systematic study of viscous shear flows.

Early contributions to the stability theory of two layer flows of different densities and viscosities are the studies of Yih (1963) and Lock (1951). The studies of Miles (1957, 1959) enlightened on the mechanisms of the formation of sea waves and initiated a fruitful line of research over the past decades. His theory on the existence of critical layers has been proven in an open sea installation (Hristov et al., 2003) and is still extensively investigated at laboratory scale.

Rao and Kobus (1975) also suggested the emergence of Kelvin-Helmholtz instabilities in spillways as a consequence of air-water velocities difference. However, little research was later conducted on the effect of the air flow development over the free surface in high-velocity spillway flows. Falvey (1980) and Chanson (1992) discussed the air flow rate in closed conduits, but not its influence on the instabilities taking place in spillway flows. Nevertheless, air flow dynamics in closed conduits may differ as velocities larger than at the free surface may occur due to closed conduit continuity (Falvey, 1980).

Based on a theoretical approach, Funada and Joseph (2001) studied the viscous Kelvin-Helmholtz instability (thus considering the viscosity of both fluids). They noticed that the unstable velocity difference associated to the classic Kelvin-Helmholtz instability ($u_{w,x} - u_{a,x} \approx 6.4$ m/s) is significantly reduced when the existence of a viscous air layer is considered in the formulation.

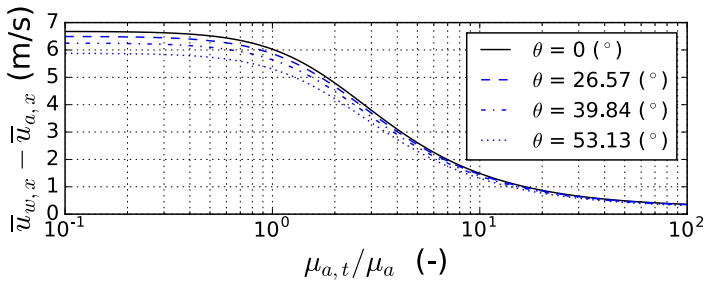

Fig. 5.7 Viscous Kelvin-Helmholtz triggering velocity obtained from analysis of the neutral curves expression of Funada and Joseph (2001) for different air superlayer viscosities.

Thus, viscosity effects close to the free surface may enhance the triggering of those instabilities.

In Fig. 5.7, the formulation of Funada and Joseph (2001) has been used to illustrate the sensitivity of the critical velocity to the value of the air viscosity in the upper layer. When assuming that the air layer, being turbulent, will behave as a more viscous fluid (with turbulent viscosity $\mu_{a,t}$), the triggering velocity drastically decreases. The spillway slope effect is accounted for by reducing the gravity according to its projection normal to the free surface. Using a turbulent viscosity for such flows is often supported in literature for other similar phenomena (Janssen, 2004).

5.4 Interfacial air layer: experimental confirmation

5.4.1 Experimental setup

These investigations were carried out on a 1V:2H ($\theta = 26.6°$) smooth chute located at the Hydraulics Laboratory of the Aachen University of Applied Sciences (FH Aachen). The chute was part of a closed water circuit where water was pumped from a lower tank into a head tank. Then water was conveyed to the spillway through a 1 m long approaching channel, which served as a broad crested weir. At the spillway end, the water was recirculated into the lower tank. The chute width was 50 cm, with a total drop height of 1.74 m and a flume length of 3.90 m. PVC was used to build the flume geometry except for one side wall, which is made of plexiglas to allow visual inspection of the flow. Nevertheless, all walls of the flume should present a similar characteristic roughness ($k_s \approx 0.1$ mm).

The flow depths were determined using ultrasonic sensors over a wide range of discharges (q = 0.050 to 0.230 m^2/s). Air flow measurements were performed for a single water flow discharge of $q = 0.130$ m^2/s. The water discharge was controlled by a frequency regulator and measured by an inductive flow meter (Krohne Waterflux 3100W). Ultrasonic sensors (microsonic mic+130/IU/TC) recorded the flow depth with a sample rate of

50 Hz for 30 seconds in steady flow conditions (0.18 to 0.57 mm accuracy for static measurements). Further information on these sensors and its performance can be found in Appendix A or in Zhang et al. (2018).

The air flow was measured with an air anemometer of 16 mm head diameter (Schiltknecht MiniAir6 Micro) with a sample time of 30 s. Random water droplets were observed, some hitting the anemometer head and dropping the measured velocity to zero and forcing to stop the experiment until the anemometer was completely dry again. The anemometer was installed in a tube of 18 mm inner diameter and 9 cm length) to improve the wetting protection. Comparative measurements without this tube showed that no significant influence on the measured data was occurring. It must be noted that, according to the manufacturer, the anemometer can only provide accurate results for velocities above 0.417 m/s. Lower values will thus be neglected in the subsequent data analysis. The probes were plugged to an universal amplifier (HBM QuantumX MX840A) and moved by a CNC controlling system (isel) with a positioning accuracy of around 0.1 mm.

5.4.2 Air velocities

Air flow develops over the water free surface due to the no-slip condition and stress continuity (Eqs. 5.9 and 5.10). This

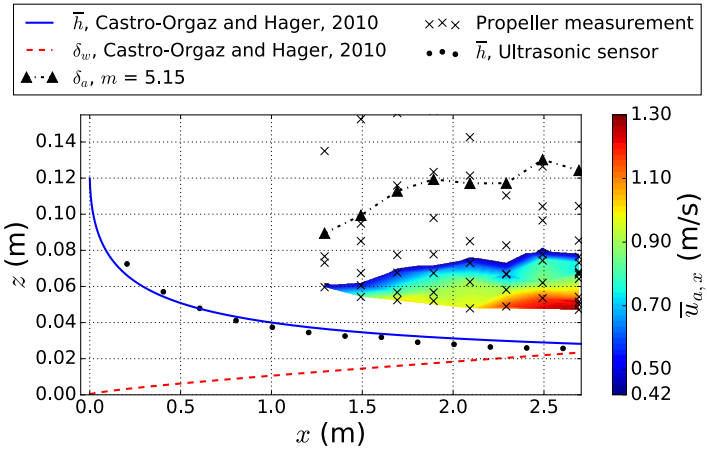

Fig. 5.8 Developing interfacial air flow for $q = 0.130$ m^2/s. Velocities below 0.417 m/s have been neglected due to propeller limitations. Velocities between propeller measurements have been linearly interpolated.

superlayer air flow has been observed for the entire range of flow rates.

Figures 5.8 and 5.9 show the air velocities for $q = 0.130$ m^2/s. It should be noted that velocities closer to the free surface could not be measured due to random impacts of droplets, and velocities under 0.417 m/s cannot be detected due to instrumentation limitations.

In order to compute the boundary layer thickness of the air layer flow (δ_a), the velocity measurements were fitted to a velocity power law for the velocity defect:

$$\frac{u_{fs} - \overline{u}_{a,x}}{u_{fs}} = \left(\frac{z - \overline{h}}{\delta_a}\right)^{1/m} \tag{5.12}$$

where m was calibrated together with δ_a to best fit the measured data (Fig. 5.9), $\overline{h}$ was estimated through the median flow depth and $\overline{u}_{a,x}$ as the median air velocity. Best fit for m yields the value 5.15. Given the accuracy of the employed experimental techniques, $u_{s,x} \approx u_{fs}$ was chosen as an appropriate simplification in Eq. 5.12. The pressure gradient for the air interfacial development is similar to the one of the water flow – same flow acceleration, $u_{s,x}(x) \approx u_{fs}(x)$ – although the interface roughness is considerably larger (i.e., $h' \gg k_s$), which results in a larger growth rate for δ_a.

It may be expected that the drag at the interface increases downstream of the self-aeration inception, resulting in higher velocities and larger momentum transfer from the water to the air flow.

5.4.3 Perturbation amplitudes

All over the spillway, the necessary mathematical conditions are satisfied for both capillary and Kelvin-Helmholtz waves (Young

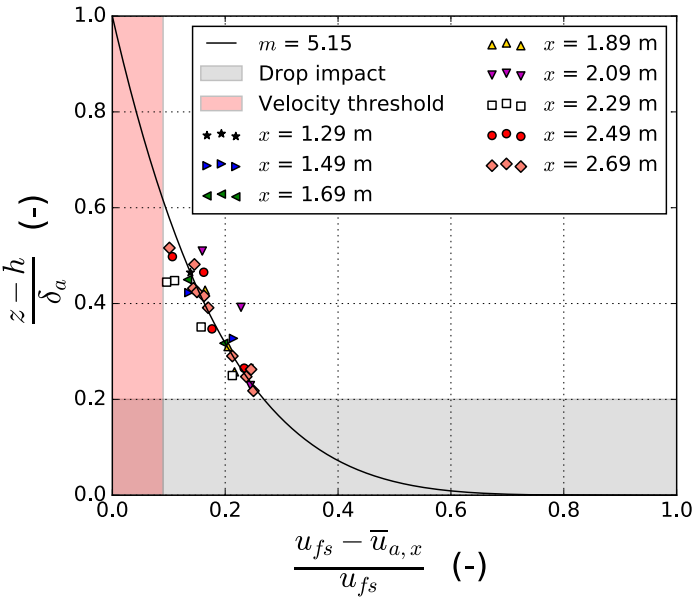

Fig. 5.9 Air velocity profiles over the non-aerated region for $q = 0.130$ m^2/s.

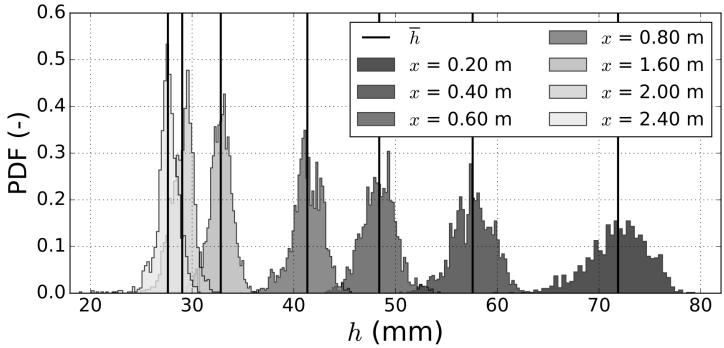

Fig. 5.10 Water depth h histograms for $q = 0.130$ m^2/s. Grayscale from darker for upstream to lighter for downstream measurements.

and Wolfe, 2014), which can coexist together with quickly vanishing modes generated by the inlet conditions.

Figure 5.10 shows some histograms for the water depth h. The stable perturbations ressemble Gaussian Probability Density Functions (PDF) for h, which are in agreement with the previous study of Longo and Losada (2012) for wind driven waves. The perturbations originated in the inlet tend to vanish quickly. This phenomenon has been observed for all the flow rates tested, in the range from $q = 0.050$ to 0.230 m^2/s.

For the non-aerated region, the following equations have been fitted to the obtained data allowing prediction of the growth of the unstable modes:

$$\begin{aligned}
\frac{\overline{h}+h'}{\overline{h}} &= 0.0125\,(x/L_i)+1.03; \qquad x/L_i < 0.8 \\
\frac{\overline{h}+h'}{\overline{h}} &= 0.05\,(x/L_i)+1.00; \\
& \qquad\qquad\qquad\qquad 0.8 < x/L_i < 1.0 \qquad (5.13)
\end{aligned}$$

Figure 5.11 illustrates the growth of the spillway perturbations. After $x/L_i \approx 0.80$, the perturbations growth rate increases drastically up to 4 times its growth; as it can be deduced from the coefficients of Eq. 5.13.

5.4.4 Entrapped air concentrations

In the aerated region, air can be found in two different forms: (a) sparse bubbles in the water flow and (b) air pockets trapped within the water roughness; the so-called entrained and entrapped air, respectively, or "bubbles and waves" (Killen, 1968; Wilhelms and Gulliver, 2005).

When the probability density function of h is known (PDF(h)), the time-averaged entrapped air concentrations ($C\,(z)$) can be obtained; and, consequently, the mean air concentration (C_m) can be estimated by integrating over the flow depth.

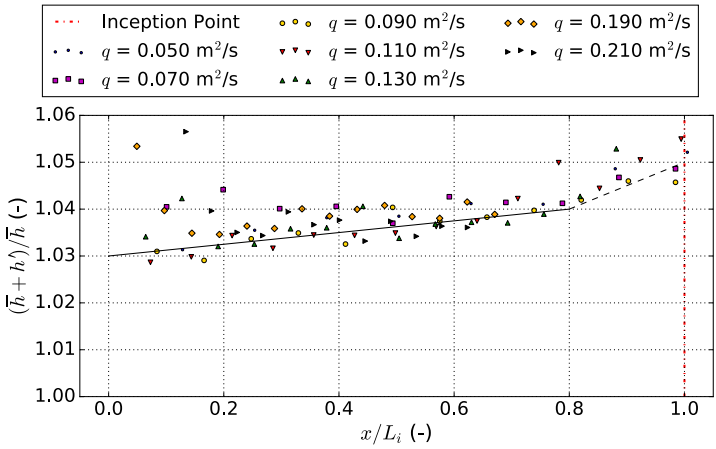

Fig. 5.11 Free surface fluctuations in the non-aerated region of the spillway. Solid and dashed lines correspond to Eq. 5.13

As shown in Fig. 5.10, the PDF(h) could be reasonably approximated by a Gaussian distribution. Its cumulative density function (CDF) has an analytical expression, which can be used to approximate the time-averaged air concentration at a given depth z. This is based on the fact that CDF(h) represents the probability that $z \leq h$, i.e: the probability of having water or air at a given depth. Hence:

$$C\left(z\right) = \frac{1}{2}\left[1 + \mathrm{erf}\left(\frac{z - \overline{h}}{h'\sqrt{2}}\right)\right] \tag{5.14}$$

Therefore, for a flow section where air is not found in the shape of bubbles, the total air concentration is directly given by the entrapped air concentration. Equation 5.14 represents an analytical profile based on the observation that the free surface oscillations can be represented by a Gaussian distribution.

The herein deduced profile, applicable for the entrapped air, bears some resemblance with the more general advective diffusion profile of Chanson (1997) and the profiles for the air concentration of jets discharging into the atmosphere, also from Chanson (1997). Additionally, the shape looks similar to the low aerated concentration profiles, as previously shown in Fig. 2.2.

Chapter 6

Free surface conceptualization

6.1 General remarks

While fluids at rest are separated by a smooth undisturbed interface, under the action of a perturbation it will move from equilibrium, propagating this motion through the domain due to gravity and surface tension (Landau and Lifshitz, 1987). During last decades, several studies have attempted to uncover the true relationship between the interface dynamics and the turbulence occurring nearby (Brocchini and Peregrine, 2001; Dabiri, 2003; Gibson and Rodi, 1989; Gulliver and Halverson, 1987; Guo and Shen, 2010; Handler et al., 1993; Mouaze et al., 2005;

Nichols et al., 2016; Savelsberg and Water, 2009; Tamburrino and Gulliver, 2007; Wang and Chanson, 2015; Zhong et al., 2016). Notwithstanding that, complete understanding is not yet available, thus becoming a bottleneck in many environmental applications and a challenge for scientists and researchers. Naturally, in highly turbulent water flows, self-aeration arises as an extreme case of the aforementioned turbulence and free surface interaction, being large displacements common at the air-water interface.

6.2 Conceptualization

In open channel flows, a free surface is usually idealised as a smooth surface pseudo-parallel to the channel bed, simply separating the water and air flow regions. Free surface curvatures are commonly considered only when transcritical flows occur.

Since an interface has vanishing mass, it cannot store momentum nor energy. Similarly to a solid wall, velocities match at both sides of the contour, implying that water velocity is automatically transferred to the air region that reciprocally exerts a drag on the water phase, simultaneously transferring shear to both fluids (Eqs. 5.9 and 5.10). Differently from a solid wall, vorticity normal to the free surface is not necessarily null. Additionally, coherent fluid volumes can move impacting the free surface, or parallel close to it, and the interface can be disturbed.

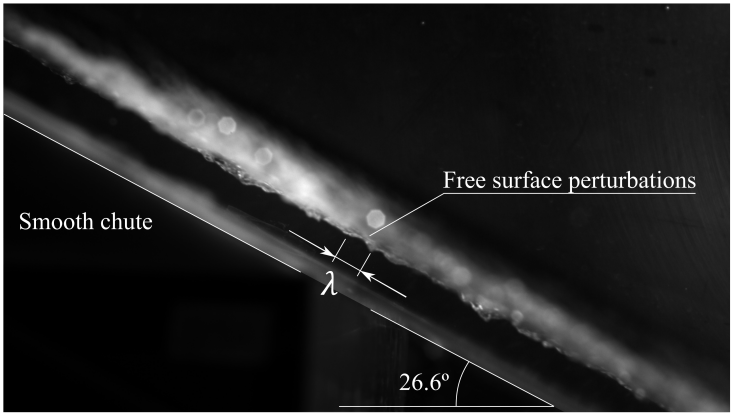

Fig. 6.1 Free surface perturbations in the non-aerated region of a smooth chute flow, adapted from Valero and Bung (2016). Flow from left to right, mean flow depth ($\overline{h}$) of 35.2 mm.

Roussinova et al. (2008), following the earlier study of Nezu (2005), suggested that the free surface behaves as a "weak wall", where normal velocity fluctuations are countered by surface tension as the interface deforms. In this manner, turbulence near the free surface can lead to wave generation (Brocchini and Peregrine, 2001).

More complex effects induced by a free surface need to be borne in mind, such as turbulence anisotropy together with shear reduction (Gibson and Rodi, 1989; Guo and Shen, 2010; Handler et al., 1993). Roussinova et al. (2008) also observed that presence of a free surface can induce secondary flows, which is

in agreement with the conclusions from the study of Tamburrino and Gulliver (2007).

Longo and Losada (2012) observed that, when compared to a solid wall, reduction of turbulence production and enhancement of turbulence transport can be expected. While Longo and Losada (2012) do not propose any physical explanation, this could be due to the pressure-velocity correlation term of the turbulence kinetic equation (see Wilcox, 2006, for a complete derivation of this equation), which is damped at a solid surface but will find a larger path at the free surface while deforming it.

Some studies have tried to address analytically the changes produced by the free surface over the turbulence quantities. Probably, the most widely acknowledged theory describing the near free surface turbulence changes is that of the theoretical framework of Hunt and Graham (1978) which, by assuming a flat wall moving with the flow velocity, showed that two layers within the fluid region take place: a blockage region (also known as source region) and a viscous region; being the prior the thickest. The original rapid distortion model of Hunt and Graham (1978) was later extended by Teixeira and Belcher (2000), accounting for non-linear interactions at the viscous region.

One interesting finding of Teixeira and Belcher (2000) is that in the blockage region, the free stream flow properties remain unchanged whereas the greatest turbulence changes take place only inside the viscous layer. The viscous region thickness δ^v

was found to grow with time (t) as (Hunt and Graham, 1978; Teixeira and Belcher, 2000)[1]:

$$\delta^v \sim \sqrt{\nu t} \tag{6.1}$$

For common hydraulic structure flows, it can be deduced from Eq. 6.1 that δ^v will have a dimension considerably smaller than those of the wavelengths commonly observed at the free surface. Differently, the blockage region will start where eddies (of size l_e) approaching the free surface end, this suggests:

$$\delta^b \sim l_e \tag{6.2}$$

with δ^b the blockage layer thickness. Both theoretical models of Hunt and Graham (1978) and Teixeira and Belcher (2000) shed accurate predictions when compared to Direct Numerical Simulation (DNS) data, where the free surface was considered flat as well. Necessarily, in such case, normal velocity fluctuations are constrained at the free surface and its energy is spread over the velocity components parallel to the free surface.

Nevertheless, when turbulence effects are comparable or greater than the gravity and surface tension actions, the turbulent eddies will strain the air-water interface and the free surface

[1]Note the homology with a laminar boundary layer developing beneath the free surface, in the water flow region, predicted by Eq. 5.11.

will significantly deviate from flat – and, obviously, the velocity fluctuations normal to the free surface will not necessarily vanish. Under strong turbulence conditions, the free surface will be more penetrated by the approaching turbulence and the normal velocity fluctuations suppression predicted by Hunt and Graham (1978) and Teixeira and Belcher (2000) may be weaker; at least in the blockage region (δ^b), outside of the viscous region (δ^v).

In spillway flows, free surface distortion has been often reported upstream of the inception point location for several decades (as shown in Fig. 6.1), starting with the study of Straub and Anderson (1958). In the study of Valero and Bung (2016), other studies observing this characteristic free surface roughness were listed.

6.3 Relevant parameters

When the free surface exhibits a strong turbulent behaviour, it seems useful to discriminate between the mean free surface $\overline{h}$ and the perturbations travelling over, which are herein referred as η (see Fig. 6.2). The mean free surface can be determined in a variety of ways. For one-dimensional flows, gradually varied flow equations (Chanson, 2004) or the turbulent boundary layer approach of Castro-Orgaz (2010) and the drawdown curve of Castro-Orgaz and Hager (2010) can result in accurate predictions. More computationally expensive approaches are also available

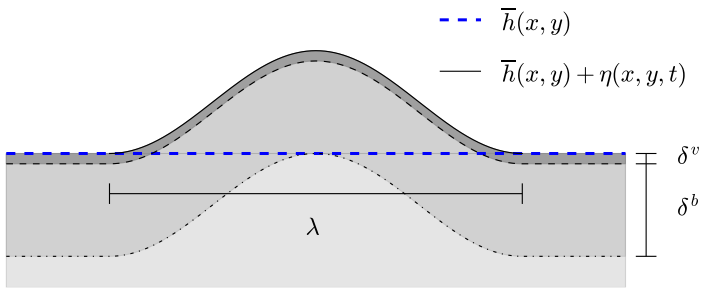

Fig. 6.2 Definition sketch of the two layers conceptualization of Hunt and Graham (1978) (viscous layer (δ^v) and blockage layer (δ^b) to a rough free surface disturbed by a turbulent eddy of size l_e comparable to the perturbation wavelength λ.

to determine the mean free surface in complex three-dimensional flows (e.g., Bayon et al., 2016; Bombardelli et al., 2011; Savage and Johnson, 2001; Valero et al., 2018b).

The free surface perturbations can show a wide range of wavelengths λ, which can be caused by the step cavity in stepped spillways, by boulders in a river flow or simply by the inherent eddies of a boundary layer flow. It is herein supposed that eddies of size l_e will produce free surface perturbations of a similar size.

One characteristic wavelength of great importance in the formation of bubbles and droplets is the Taylor lengthscale. It can be derived through the analysis of the inviscid Kelvin-Helmholtz instability (Ishii and Hibiki, 2010, p. 51):

$$\lambda_c \equiv 2\pi \sqrt{\frac{\sigma}{g\,(\rho_w - \rho_a)}} \approx 1.71\,\text{cm} \tag{6.3}$$

The Taylor lengthscale has also important implications in the study of the Rayleigh-Taylor instability, which can be considered a special case of the Kelvin-Helmholtz instability (see Ishii and Hibiki, 2010).

Kelvin-Helmholtz instability happens due to the velocity discontinuity across the interface of two fluids. However, for real fluids, viscosity prevents this discontinuity to happen and a more physically consistent description is the one of the viscous Kelvin-Helmholtz. This has been analytically studied by Funada and Joseph (2001). When viscosity is considered at the interface, the most unstable wavelengths for air-water flows can differ; for instance, Funada and Joseph (2001) obtained values ranging between 1.44 to 1.61 cm (see Table 1 of Funada and Joseph, 2001).

The term "ripples" is commonly used to refer to waves with wavelengths larger than λ_c. If the wave is large enough ($\lambda \gg \lambda_c$), surface tension effect becomes negligible. Contrarily, if the wavelength is comparably smaller, it is believed to be the capillary force governing the wave motion. In spillway flows, wavelengths of a comparable order to λ_c can be easily observed, which suggests that both gravity and surface tension can play an important effect on the stability of the free surface disturbances.

Given Eq. 6.1, obtained by the two layers theory of Hunt and Graham (1978), and Eq. 6.3, it can be expected viscous layers thinner than most of the eddies (l_e) present in the flow, or than the Taylor lengthscale. This suggests that the viscous layer plays a minor role on the free surface dynamics. Therefore, assuming that eddies of the size of the wavelengths are originating those wavelengths, the viscous region will deform parallel to the free surface (Fig. 6.2).

The aforementioned conditions will be supporting the mathematical derivations of the sequent chapter and can be written as:

$$\lambda \sim l_e, \qquad \delta^b \sim l_e, \qquad \lambda \gg \delta^v \tag{6.4}$$

6.4 Breakup criteria

Intuitively, it is reasonable to assume that an individual perturbation may no longer sustain its shape and break when its height A becomes too large with respect to its length. This distortion can be expressed in terms of the perturbation slope (or steepness):

$$S \equiv A/\lambda \tag{6.5}$$

This geometric relationship has been widely studied in breaking waves to describe their onset. It must be noted that some of these studies defined the steepness by using the wavenumber k and the wave amplitude (for a sinusoidal wave, half the wave height) as (Perlin et al., 2013): $\kappa A/2$; which differs from that steepness of Eq. 6.5, given that the relationship between wavelength and wavenumber is:

$$\kappa = 2\pi/\lambda \tag{6.6}$$

Hence, care must be taken when comparing wave literature to the herein described perturbations, as the breaking steepness reported can be π times bigger than that defined by Eq. 6.5. Criterion as defined by Eq. 6.5 is a more geometrically intuitive slope.

In wave applications, intense research activity has taken place after the milestone study of Stokes (1880). More contemporary works of Duncan (1981) and Melville (1982), among others (Perlin et al., 2013), have contributed to a fruitful research on breaking waves. As a result, different criteria have been formulated based on theoretical analyses, numerical simulations or experimental results, the former at both laboratory and prototype scale.

These breaking criteria could be classified as: breaking criteria at shallow waters, where the wave is affected by the limited

water depth and a ratio of the type $A/\overline{h} \approx 0.78$ is oftentimes formulated (Novak et al., 2007); and breaking waves in deep and intermediate waters. For the latest case, three types of methods can be distinguished (Barthelemy et al., 2018; Perlin et al., 2013):

1. Geometric criteria: which comprehends breaking criteria based on thresholds for variables such as wave steepness (Eq. 6.5), wave asymmetry, maximum theoretical steepness or steepness at the front face of the wave crest.

2. Kinematic criteria: based on thresholds for variables such as the Lagrangian crest acceleration or the ratio between crest fluid speed and phase speed.

3. Dynamic criteria: based on energetic considerations such as the evolution of the intragroup energy flux, which causes the tallest crest of an unsteady wave group to break when a local stability threshold is exceeded. Nonetheless, these criterion can simplify to a straightforward kinematic relation (e.g., Barthelemy et al., 2018).

The farther we move down in the previous list, the more we need to know about the wave characteristics. Notwithstanding that, some assumptions make dynamic or kinematic criteria to take the written form of kinematic or geometric criteria, correspondingly. Thus, the rationale behind a dynamic criteria can be represented – in a simpler way – by a purely geometric criteria provided that the necessary assumptions are done.

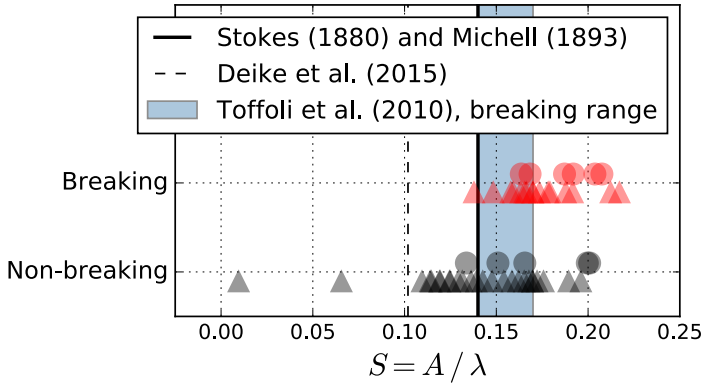

Fig. 6.3 Breaking slope for waves at intermediate and deep waters. Data of Barthelemy et al. (2018), △ for two-dimensional waves and ◯ for three-dimensional waves.

In Fig. 6.3, several two- and three-dimensional waves, breaking and non-breaking waves, from the study of Barthelemy et al. (2018) are presented jointly with the breaking criterion of Stokes (1880) and Michell (1893), and the criteria of Deike et al. (2015) for gravity waves. Better data clustering could be obtained with an appropriate dynamic criterion, as shown by Barthelemy et al. (2018). Seek for more complex breaking criteria is justified by Barthelemy et al. (2018) given the scatter that the data holds. However, that scatter is probably below the uncertainty that other hypotheses introduced in other parts of this analysis and simpler breakup criteria are hence justified.

Differences exist between coastal waves and self-aerating flows in hydraulic engineering applications. For spillway applications, large perturbation steepness values can be readily observed on images reported in the literature, as for instance in Fig. 6.1. Consequently, homology between waves and free surface perturbations should be made with care, due to the following two reasons:

1. Little is known on how these perturbations behave. No empirical results exist so far on aspects such as velocity fields inside the perturbations or their exact geometry. Hence, kinematic and dynamic criteria would be difficult to apply.

2. Breaking criteria formulated for deep and intermediate waters (i.e., short wavelengths) usually comprehend waves with wavelengths over 0.5 to 1 m, where surface tension plays no effect (Barthelemy et al., 2018). However, for self-aeration applications, short wavelengths are of a few millimetres and, consequently, surface tension could exert a relevant stabilizing effect.

3. Perturbations in hydraulic engineering flows are subject to considerable levels of shearing, which may lead to perturbations' shape distortion and a stability reduction.

Hence, limited by the current knowledge on free surface perturbations, there is no reason to use breaking onsets more

complicated than those simply defined by a threshold for the steepness, nor to take the thresholds directly (and with blind faith) from open sea applications. Thus, as the slope holds below a limiting steepness (S_{lim}), the flow is herein supposed to remain non-aerated:

$$S_{lim} > S \tag{6.7}$$

Just as a reference, Stokes (1880) predicted that a regular two-dimensional wave would become unstable when the particle velocity at the crest exceeds the phase velocity. In deep waters, Michell (1893) related Stoke's criterion to $S_{lim} = 0.14$; which, as can be deduced from review work of Perlin et al. (2013), is an intermediate value clustering different experimental data. It is noteworthy the well-known criterion of Miche (1944):

$$S_{lim} = \frac{1}{7} \tanh\left(\frac{2\pi\overline{h}}{\lambda}\right) \tag{6.8}$$

which, for deep waters, results in:

$$S_{lim} = \frac{1}{7} \approx 0.14 \tag{6.9}$$

More recently, Toffoli et al. (2010) reported characteristic values for maximum S_{lim} around 0.14 to 0.17 in open ocean three-dimensional waves. For asymmetrical waves, front crest steepness can reach higher values (Perlin et al., 2013). These

studies, however, clearly disregard the stabilizing effect of surface tension for short wavelengths.

Recently, Deike et al. (2015) used DNS to study waves where capillary – surface tension – effects play an important role. Deike et al. (2015) noticed that surface tension considerably stabilizes the waves and higher values of the steepness are necessary to lead to a wave breaking regime. Wave breaking regime was defined as the state of the wave where a completely vertical face can be seen in the wave.

Deike et al. (2015) studied the relationship between the Bond number and the critical wave steepness for breaking and plunging waves. When the water to air density ratio is fixed (998/1), gravity is constant (9.8 m/s^2) and surface tension too (0.0829 N/m), Bond number can be unmistakably related to the wavenumber and, consequently, to the wavelength; which allowed to reanalyse data of Deike et al. (2015), as presented in Fig. 6.4. The capillary range detected by Deike et al. (2015) for breaking waves seems to hold for wavelengths below 10.9 cm, which in terms of the Taylor wavelength is λ/λ_c = 6.37. For plunging waves, the limit grows up to λ/λ_c = 14.30; which means λ = 24.5 cm.

For $\lambda/\lambda_c < 6.37$, the following expression has been fitted to the data of Deike et al. (2015):

$$S_{lim} = 0.35 \left(\frac{\lambda}{\lambda_c}\right)^{-2/3} \tag{6.10}$$

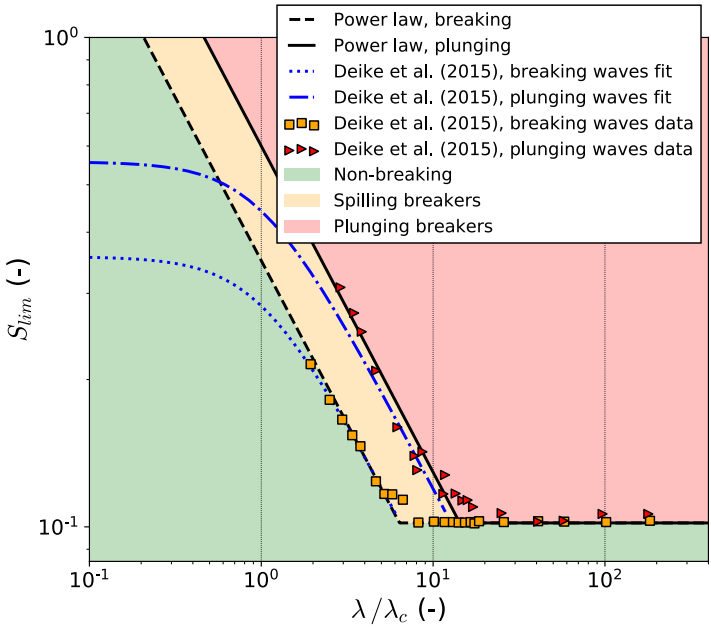

Fig. 6.4 Breaking slope for waves subject to significant surface tension effects. Black lines for: breakup steepness of Eq. 6.10, plunging steepness of Eq. 6.11 and asymptotic limit of Eq. 6.12.

which fits data of Deike et al. (2015) but does not present a power slope change at lower wavelengths, as fit of Deike et al. (2015) does. It must be noted that in spillway applications, expected wavelengths can be considerably smaller and thus, an expression with a change of slope out of the fitting range is not convenient.

For the plunging limit, data was selected when showing a horizontal wave face below the crest, situation imminent to occurring a jet with considerable air entrainment. The following fit has been obtained for $\lambda/\lambda_c < 14.30$:

$$S_{lim} = 0.60 \left(\frac{\lambda}{\lambda_c}\right)^{-2/3} \tag{6.11}$$

Again, the proposed fit holds a constant power law scaling out of the range of data fitting, differently from that proposed by Deike et al. (2015). Both breaking and plunging waves over the formerly defined limits reach a constant S_{lim} at large wavelengths:

$$S_{lim} = 0.102 \tag{6.12}$$

The main rationale of fitting constant power law equations (instead of using fits of Deike et al., 2015) is that at $\lambda \to 0$, one may expect the stability of the wave to also grow, instead of stabilize at an arbitrary plateau out of the fitting range.

Deike et al. (2015) discussed that below the breaking limit, non-breaking or parasitic waves can be observed, being the latest

only observable for wavelengths below 10 cm. For waves with steepness values between breaking and plunging, spilling breakers can be observed – which produce little or no aeration (see Fig. 4 of Deike et al., 2015) –. For steepness values over the plunging limit, plunging breakers can be observed, which lead to high levels of aeration.

Partial conclusions

Part II analysed the non-aerated region to provide the subsequent chapters with a solid foundation. This part was intentionally divided into two chapters, with the intention to highlight the relevance of a commonly forgotten feature: the free surface. Hence, Chapter 5 dealt with the water and air phases in the spillway non-aerated flow region while Chapter 6 was entirely dedicated to provide an accurate description and conceptualization of what a free surface is. A breakup criterion was proposed in Section 6.4, based on the assumption that perturbations may reach unstable configurations and surface tension may seek more stable geometries by breaking the perturbations into droplets. In such case, breakup is assumed to be explained by the steepness ratio A/λ, which can also vary with the perturbation wavelength.

Part III

Turbulent free surface dynamics

Chapter 7

Turbulent free surface equations

7.1 Perturbation geometry

A small amplitude, three-dimensional perturbation is assumed to travel over the mean free surface level. At a given time t, it will have its center at the coordinates x_p and y_p (same coordinate system of Fig. 2.1), wavelength λ and a height (or amplitude) of A. The free surface deviation caused by this perturbation is supposed to be represented by the following expression:

$$\eta(r) = \frac{A}{2}\left[\cos\left(\frac{2\pi r}{\lambda}\right) + 1\right] \tag{7.1}$$

with r the radial coordinate centred at the axis of the perturbation. Using an axis translation to the center of the perturbation ($X = x - x_p$ and $Y = y - y_p$), r can be simply expressed as:

$$r = \sqrt{X^2 + Y^2} \tag{7.2}$$

Equation 7.1 is tangent to the mean free surface at $r = \lambda/2$, yielding a crest base of surface $\mathbb{S}_b = \pi\lambda^2/4$. Equation 7.1 would yield new two-dimensional crests for $r > \lambda/2$, but the present analysis is restricted to the geometry over and below $\mathbb{S}_b$, up to the first $\eta = 0$. Thereafter, the part over $\eta = 0$ will be called perturbation's crest and, the part below, the submerged body. The complete geometry of the perturbation is shown in Fig. 7.1.

Thereof, the perturbation mass can be computed as the sum of the masses of the crest and the submerged body. The perturbation crest mass m can be obtained by integrating its differential volume ($\mathrm{d}\mathbb{V}_m$), multiplied by the fluid density, extended to the bounds $z = 0$ and $z = \eta$:

$$m = \int \rho_w \, \mathrm{d}\mathbb{V}_m = \rho_w k_A \lambda^2 A \tag{7.3}$$

being[1]:

[1]Note that k_A represents the percentage of the volume that the perturbation takes, relative to the minimum prism surrounding it (of volume $\lambda \times \lambda \times A$). A similar logic applies to other coefficients, all analytically obtained.

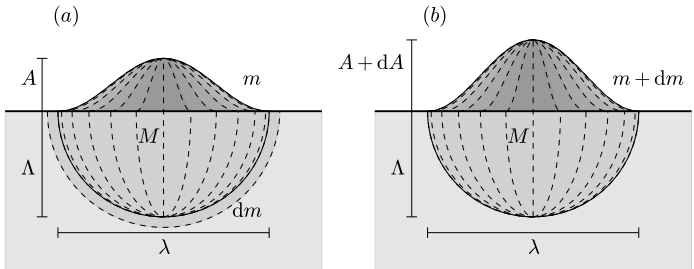

Fig. 7.1 Perturbation geometry. Crest defined by Eq. 7.1, submerged body forming a semi-sphere. Main variables at times: *(a)* t and *(b)* $t + \mathrm{d}t$. $\mathrm{d}m$ is introduced inside the control volume continuously every $\mathrm{d}t$, producing an increment of the amplitude $\mathrm{d}A$. Note that wavelength λ and submerged body depth Λ remain constant.

$$k_A = \frac{(\pi+2)(\pi-2)}{8\pi} \approx 0.234 \tag{7.4}$$

Underneath the perturbation crest, the submerged body volume will move with the same velocity. Assuming that the perturbation is caused by turbulence structures of a size l_e, proportional to λ (Eq. 6.4), the amplitude of the perturbation below the water surface can be expressed as:

$$\Lambda = N_\Lambda \lambda \tag{7.5}$$

where N_Λ could take a value close to 0.5 in order to make the submerged body coinciding with the horizontal perturbation extension.

Assuming $N_\Lambda \approx 0.5$ geometrically implies that the eddies hold axial symmetry when the eddy is impacting with the free surface. As not much information is available on the size and shape of the turbulent structures occurring immediately beneath the free surface, it is simply assumed $N_\Lambda \approx 0.5$ and the submerged body shape is thereby taking the form of a semi-sphere.

The mass of the submerged part of the perturbation can be estimated as:

$$M = \rho_w k_\Lambda \lambda^2 \Lambda \tag{7.6}$$

with:

$$k_\Lambda = \frac{1}{6}\pi \approx 0.524 \tag{7.7}$$

7.2 Perturbation kinematic equation

The herein defined perturbation can have a non-null velocity normal to the free surface (v_p) as it grows with time. This perturbation velocity is not the normal velocity fluctuation observed in common boundary layers reaching the free surface (or other types

of shear flows) but represents the dynamic behaviour of a "blob" as a consequence of all the forces acting immediately around the free surface. From a merely kinematic approach, it can be defined as the displacement of the center of gravity of the perturbation. The centre of gravity z_p can be computed by integrating the z coordinate over the total volume of the perturbation $\mathbb{V}_p$. z_p will be moving with time as a consequence of the growth of the amplitude A:

$$\begin{aligned} z_p &= \frac{1}{\mathbb{V}_p}\int z\,\mathrm{d}\mathbb{V}_p = \frac{1}{\mathbb{V}_m+\mathbb{V}_M}\left(\int z\,\mathrm{d}\mathbb{V}_m + \int z\,\mathrm{d}\mathbb{V}_M\right) \\ &= \frac{k_m A\,\mathbb{V}_m + k_M\,\Lambda\,\mathbb{V}_M}{\mathbb{V}_m+\mathbb{V}_M} \end{aligned} \tag{7.8}$$

For the coefficient related to the crest of the perturbation:

$$k_m = \frac{3\pi^2-16}{8\,(\pi+2)\,(\pi-2)} \approx 0.290 \tag{7.9}$$

and for the coefficient related to the submerged body of the perturbation:

$$k_M = -\frac{3}{8} = -0.375 \tag{7.10}$$

As the submerged body of the perturbation is supposed to depend only on the wavelength (Eqs. 7.5, 7.6 and 7.7), v_p only

depends on dA which, by using the Leibniz rule, can be written as:

$$v_p \equiv \frac{\mathrm{d}z_p}{\mathrm{d}t} = \frac{\mathrm{d}z_p}{\mathrm{d}A}\frac{\mathrm{d}A}{\mathrm{d}t} = k_p \frac{\mathrm{d}A}{\mathrm{d}t} \tag{7.11}$$

being $k_p = \mathrm{d}z_p/\mathrm{d}A$, which expresses how the centre of gravity varies when the amplitude of the perturbation grows:

$$k_p = \frac{k_A\left[k_m A\left(k_A A + 2k_\Lambda \Lambda\right) - k_M k_\Lambda \Lambda^2\right]}{\left(k_A A + k_\Lambda \Lambda\right)^2} \tag{7.12}$$

Equation 7.11 is a kinematic relation between the perturbation displacement and the amplitude growth. Equation 7.12 is quasilinear and its derivative becomes constant for large values of A. For A = 0, equation 7.11 takes the value:

$$v_p = -\frac{k_A k_M}{k_\Lambda}\frac{\mathrm{d}A}{\mathrm{d}t}, \qquad A = 0 \tag{7.13}$$

which remains valid for small amplitude disturbances. In the other extreme, for large displacements, the asymptotic value is given by:

$$v_p = k_m \frac{\mathrm{d}A}{\mathrm{d}t}, \qquad A \to \infty \tag{7.14}$$

7.3 Perturbation dynamic equation

At a given time t, the perturbation defined in Section 7.1 moving with a velocity v_p normal to the free surface has a vertical momentum:

$$P_z(t) = (M+m)\, v_p + \mathrm{d}m\, v_{in} \tag{7.15}$$

where $\mathrm{d}m$ refers to the continuous increment of mass taking place each $\mathrm{d}t$ due to the perturbation growth and v_{in} is the velocity of the fluid entering the perturbation's control volume in the z coordinate. For simplicity, the total mass of the perturbation $M_p = M + m$ will be introduced when possible.

Likewise Eq. 7.15, the momentum after $\mathrm{d}t$ can be written as (see Fig. 7.1):

$$\begin{aligned} P_z(t+\mathrm{d}t) &= (M_p + \mathrm{d}m)(v_p + \mathrm{d}v_p) \\ &= M_p\, v_p + M_p\, \mathrm{d}v_p + \mathrm{d}m\, v_p + \mathrm{d}m\, \mathrm{d}v_p \end{aligned} \tag{7.16}$$

As $\mathrm{d}m\, \mathrm{d}v_p$ is of higher order, it can be neglected. The change of momentum normal to the free surface after $\mathrm{d}t$ can be obtained by subtracting Eq. 7.15 from Eq. 7.16. By applying Newton's

second law, the change of momentum can be related to the forces acting over the control volume:

$$\frac{\mathrm{d}P_z}{\mathrm{d}t} = M_p \frac{\mathrm{d}v_p}{\mathrm{d}t} + (v_p - v_{in}) \frac{\mathrm{d}m}{\mathrm{d}t} = \sum F_z \tag{7.17}$$

being $\sum F_z$ the sum of forces normal to the free surface. The increment of mass $\mathrm{d}m$ can be computed by differencing the previously obtained m (Eq. 7.3):

$$\mathrm{d}m = \rho_w \, k_A \, \lambda^2 \, \mathrm{d}A \tag{7.18}$$

The normalwise velocity (v_{in}) at which $\mathrm{d}m$ enters the control volume can be estimated on the basis of the perturbation's change of volume ($\mathrm{d}\mathbb{V}_p/\mathrm{d}t$) and the vertical component of the submerged body's area, which coincides with the perturbation's base ($\mathbb{S}_b$):

$$v_{in} \equiv \frac{(\mathrm{d}\mathbb{V}_p/\mathrm{d}t)}{\mathbb{S}_b} = k_{in} \frac{\mathrm{d}A}{\mathrm{d}t} \tag{7.19}$$

with:

$$k_{in} = 4 \frac{k_A}{\pi} \approx 0.298 \tag{7.20}$$

The velocity difference of Eq. 7.17 can be written in terms of k_{in} and k_p as:

$$v_p - v_{in} = (k_p - k_{in})\,\frac{\mathrm{d}A}{\mathrm{d}t} = \left(\frac{k_p - k_{in}}{k_p}\right) v_p = \left(1 - \frac{k_{in}}{k_p}\right) v_p = \chi\, v_p \tag{7.21}$$

By introducing Eqs. 7.18 and 7.21 into Eq. 7.17, and rearranging terms, it can be written the following equation for the perturbation dynamics:

$$\frac{\mathrm{d}v_p}{\mathrm{d}t} = \frac{1}{k_\Lambda \Lambda + k_A A}\left[\frac{\sum F_z}{\rho_w \lambda^2} - \chi\, k_A\, v_p \frac{\mathrm{d}A}{\mathrm{d}t}\right] \tag{7.22}$$

It is of interest to rewrite Eqs. 7.11 and 7.22 in the spatial domain, given that the forces and flow variables are commonly distributed over the space. Thus, the advance of the perturbation in the x-direction (streamwise direction, see Fig. 2.1) can be written as:

$$\mathrm{d}x/\mathrm{d}t = u_p \tag{7.23}$$

being u_p the streamwise velocity of the perturbation, parallel to the mean free surface. Kline et al. (1967) discussed on the velocity of the eddies ejected from a boundary layer, concluding that they move at around 80 % of the free stream velocity. This could be due to the generation of the eddies at the lower regions of the boundary layer where velocities remain below the free

stream velocity. However, given the uncertainty shown in their results[2], a good approximation would be to simply assume that the eddies move with the free stream velocity:

$$u_p \approx u_{fs} \tag{7.24}$$

Finally, inserting Eq. 7.23 into the kinematic and the dynamic equations (Eqs. 7.11 and 7.22), it can be obtained:

$$\frac{\mathrm{d}A}{\mathrm{d}x} = \frac{v_p}{k_p u_p} \tag{7.25}$$

$$\frac{\mathrm{d}v_p}{\mathrm{d}x} = \frac{1}{k_\Lambda \Lambda + k_A A}\left[\frac{\sum F_z}{\rho_w \lambda^2 u_p} - \chi\, k_A\, v_p \frac{\mathrm{d}A}{\mathrm{d}x}\right] \tag{7.26}$$

Dynamic equation (Eq. 7.26) and the kinematic equation (Eq. 7.25) form a system of differential equations, with A and v_p the variables to be solved. k_p can be determined using the quasilinear Eq. 7.12, or any of its approximations (Eqs. 7.13 and 7.14) when suitable. Discretization of Eqs. 7.25 and 7.26 is straightforward.

In order to gain further insight, Eq. 7.25 can be substituted into Eq. 7.26, which leads to a second order non-linear differential equation for A:

[2] See Fig. 18 of Kline et al. (1967).

$$\frac{\mathrm{d}}{\mathrm{d}x}\left(k_p\,u_p\,\frac{\mathrm{d}A}{\mathrm{d}x}\right)=\frac{1}{k_\Lambda\Lambda+k_A A}\left[\frac{\sum F_z}{\rho_w\lambda^2 u_p}-\chi\,k_A\,k_p\,u_p\left(\frac{\mathrm{d}A}{\mathrm{d}x}\right)^2\right] \tag{7.27}$$

where both terms on the right-hand are non-linear: the first order derivative of A has a power of 2 (and multiplied by the quasilinear linear k_p) and the sum of forces, that will also depend on A non-linearly. Both terms in the right-hand side of Eq. 7.27 can compensate, which would result in a null curvature of A, but not necessarily a null A. The perturbation wavelength λ is present in many terms of Eq. 7.27, which results in different growth rates for different wavelengths.

Chapter 8

Forces acting on the perturbation

8.1 General remarks

Accurate determination of the perturbation growth strongly depends on the careful estimation of the forces acting over the control volume. In real fluids applications, this is not a trivial task and some terms may require simplification up to an extent. The sum of forces of Eq. 7.26 can be split into the following terms:

$$\sum F_z = F_{\tau z} + F_{\sigma z} + F_{gz} + F_{pz} \tag{8.1}$$

where $F_{\tau z}$, $F_{\sigma z}$, F_{gz} and F_{pz} are, respectively, the vertical forces associated to the turbulent stresses, surface tension, gravity and pressure acting over the control volume.

8.2 Force due to turbulent stresses

In shear flows, velocity fluctuations will reach the free surface deforming it. Different turbulence terms have been suggested by different researchers to be causing free surface breakup, still not being in clear agreement on which is the responsible one[1].

The force caused by the velocity fluctuations is a three components vector, from which the herein presented analysis uses only its z component (momentum balance is assessed normal to the free surface). For the water region, this vector can be computed as:

$$\mathbf{F}_{\tau\mathbf{w}} = \int \tau_{\mathbf{w}} \, \mathbf{n} \, \mathrm{d}\mathbb{S}_{\Lambda} \tag{8.2}$$

Likewise, for the air region:

$$\mathbf{F}_{\tau\mathbf{a}} = \int \tau_{\mathbf{a}} \, \mathbf{n} \, \mathrm{d}\mathbb{S}_{A} \tag{8.3}$$

[1] See Eqs. 2.1 to 2.4, and the studies of Ervine and Falvey (1987), Ervine (1998), Chanson (2009), Chanson (2013a) and Valero and Bung (2016)

where $d\mathbb{S}_\Lambda$ and $d\mathbb{S}_A$ refer, correspondingly, to the outer area of the submerged part of the perturbation and the perturbation's crest, $\mathbf{n}$ is the unit (column) vector normal to the control volume outer surface and τ is the apparent stress tensor, which can be affecting the perturbation from the water region ($\tau_{\mathbf{w}}$) and from the air region ($\tau_{\mathbf{a}}$).

The force due to the vertical component of the turbulent stresses acting on the control volume can be obtained by taking the z component of the vector of total forces:

$$F_{\tau z} = (\mathbf{F}_{\tau\mathbf{w}} + \mathbf{F}_{\tau\mathbf{a}})_z = F_{\tau wz} + F_{\tau az} \tag{8.4}$$

Each element (i, j) of the stress tensor at the water region ($\tau_{\mathbf{w}}$) can be written as:

$$\tau_{wij} = \mu_w \left(\frac{\partial \overline{u}_i}{\partial x_j} + \frac{\partial \overline{u}_j}{\partial x_i} \right) - \rho_w \overline{\tilde{u}_i' \tilde{u}_j'} \tag{8.5}$$

which is made of shear ($i \neq j$, off-diagonal components) and normal stresses terms ($i = j$, diagonal components).

When λ is relatively small (or shearing does not vary in space), the shear distribution around the control volume results in a negligible (or null) force. Differently, the normal velocity fluctuations in the z direction result in a non-null force. This ad-

dresses the ambiguity related to which component of the velocity fluctuations is the main responsible of the free surface breakup.

For $i = j$, the first term of the right-hand side of Eq. 8.5 corresponds to the derivative of the mean velocity normal to the free surface. This term vanishes as this mean velocity component is null, given that the mean free surface is steady. Thus, only $\overline{\tilde{u}'_z \tilde{u}'_z}$ contributes to the velocity fluctuation force ($F_{\tau z}$). Nonetheless, $\overline{\tilde{u}'_z \tilde{u}'_z}$ has not been properly defined yet.

The term $\overline{\tilde{u}'_z \tilde{u}'_z}$ accounts for the part of the velocity fluctuations ($\overline{u'_z u'_z}$) that takes place in a scale smaller or comparable to the scale of the perturbation's wavelength. The rationale behind this assumption is that when a big turbulent structure reaches the free surface with a lengthscale greater ($l_e \gg \lambda$), the smaller perturbation should be advected together with the bigger eddy without effectively absorbing any momentum from it as, likewise, the perturbation surfs over the mean flow[2]. Intuitively, eddies of size l_e should be expected to produce perturbations of a comparable wavelength λ.

To compute $\overline{\tilde{u}'_z \tilde{u}'_z}$ consistently with the aforementioned discussion, it is necessary to define the normal velocity fluctuation by means of the spectrum (Pope, 2000):

[2]In other words, large turbulent structures will produce big waves – or in a similar scale – and small turbulent structures will produce waves with small lengthscales.

$$\overline{u_z' u_z'} = \int_0^\infty E_{zz}(\kappa)\,\mathrm{d}\kappa \tag{8.6}$$

with E_{zz} the one-dimensional velocity spectrum and κ the eddy wavenumber. The energy spectrum is a particularly useful means of distinguishing between the energy held in eddies of different sizes (Davidson, 2015). By setting a wavenumber threshold (κ_e) as the lower integration limit in Eq. 8.6, the spectrum is filtered resulting in the herein defined effective normal velocity fluctuations:

$$\overline{\tilde{u}_z' \tilde{u}_z'} = \int_{\kappa_e}^\infty E_{zz}(\kappa)\,\mathrm{d}\kappa = f_\kappa \overline{u_z' u_z'} \tag{8.7}$$

The wavenumber related to the perturbation wavelength can be estimated as:

$$\kappa_e = 2\pi/l_e \approx 2\pi/\lambda \tag{8.8}$$

Equations 8.6 and 8.7 imply that the turbulence correction factor necessarily satisfies $f_\kappa \leq 1$. In order to compute the related force term, it becomes necessary to define a model spectrum. One that satisfies Kolmogorov hypothesis at high frequencies can be derived on the basis of the non-dimensional spectrum of Pope (2000):

$$E_{zz}(\kappa) = \frac{2\mathscr{L}_{zz}\overline{u_z'u_z'}}{\pi}\left(\frac{\alpha^2}{\alpha^2+\kappa^2}\right)^{(1+2\xi)/2} \tag{8.9}$$

with $\xi = 1/3$ to satisfy that the spectrum has a $-5/3$ slope at high wavenumbers. The shape of the model spectrum defined by Eq. 8.9 is shown in Fig. 8.1. $\mathscr{L}_{zz}$ is the transverse integral lengthscale and is obtained by integration of the transverse autocorrelation function (Pope, 2000).

Schlichting (1979) argued that integral lengthscales are a measure of the extent of the mass which moves as a unit. Equivalently, it can be understood as a measure of the average eddy size, although a wide range of eddies are present in the flow. It must be noted that this characteristic lengthscale is defined in a different manner than L_t of Eq. 2.5 as, for instance, in isotropic turbulence $\mathscr{L}_{zz}$ takes half the value of the longitudinal integral scale (Pope, 2000; Tennekes and Lumley, 1972).

Recent study of Johnson and Cowen (2016) studied streamwise and transverse lengthscales in open channel flows, considering smooth, rough bed and compound channels. Johnson and Cowen (2016) found that there is a strong relation between the transverse lengthscale and the flow depth in fully developed flows ($\mathscr{L}_{zz} \approx 0.5\overline{h}$). For partially developed flows, the boundary layer thickness (δ) is herein proposed to be more likely the appropriate scaling parameter:

$$\mathscr{L}_{zz} \approx 0.5\,\delta \tag{8.10}$$

being this assumption also consistent with the partially developed flow data of Johnson and Cowen (2016).

The $-5/3$ slope is also reasonable even when the free surface acts as a blockage surface. Flores et al. (2017) proposed that the strong vertical shearing of the horizontal velocity would lead to a downscale transfer of energy and to the development of the $-5/3$ spectrum for the horizontal velocities. Notice that in Flores et al. (2017) vertical velocities are suppressed, which is a more restrictive situation than that considered here. Moreover, Johnson and Cowen (2017) obtained a $-5/3$ inertial subrange from surface velocity measurements.

Based on the discussion of Chapter 6, at the outer surface of the control volume the turbulence quantities are taken without correcting them by the influence of the free surface. This implies that $l_e \gg \delta^v$ and, therefore, the analysis will be valid as far as the most unstable wavelength remains greater than δ^v, which can be estimated using Eq. 6.1 and, expectedly, remains around a few millimetres. This is reasonable as the surface tension will considerably stabilize high wavenumbers and most unstable wavelength can be expected to be in the order of λ_c (Eq. 6.3) or greater. Moreover, as the free surface deforms, the submerged control volume is likely to be partially outside of the blockage

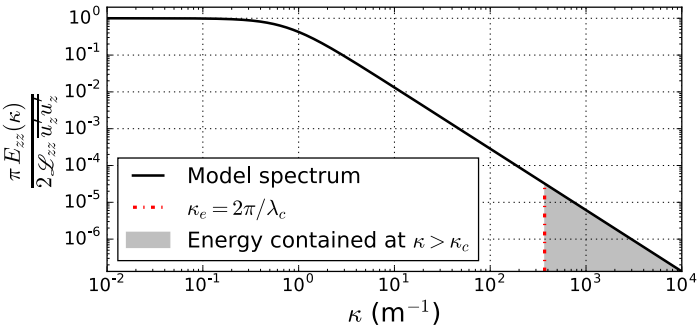

Fig. 8.1 Model spectrum of Eq. 8.9 and energy associated to eddies l_e smaller than the Taylor lengthscale λ_c. Unit transverse lengthscale and normal velocity fluctuations.

layer (Fig. 6.2), where also the biggest part of the vertically projected area is contained.

The corresponding autocorrelation function (B_{zz}) can be obtained by taking the inverse Fourier transform of the model spectrum of Eq. 8.9:

$$B_{zz}(r) = \frac{2\,\alpha\,\mathscr{L}_{zz}\,\overline{u_z'u_z'}}{\sqrt{\pi}\,\Gamma(\xi+1/2)}\left(\frac{1}{2}r\,\alpha\right)^{\xi} K_{\xi}\left(r\,\alpha\right) \tag{8.11}$$

being K_ξ the modified Bessel function of the second kind and Γ the gamma function. In order to satisfy $B_{zz}(0) = \overline{u'_z u'_z}$, the model constant α must take the value:

$$\alpha = \frac{\sqrt{\pi}}{\mathscr{L}_{zz}} \Gamma(\xi + 1/2) / \Gamma(\xi) \tag{8.12}$$

As defined, the model spectrum of Eq. 8.9 satisfies two conditions. The first one related to the transverse lengthscale:

$$\frac{\pi E_{zz}(0)}{2\overline{u'_z u'_z}} = \mathscr{L}_{zz} \tag{8.13}$$

and the second one is that given by Eq. 8.6.

More complicated models for the spectrum could be used, better reproducing the decay region for instance (Pope, 2000). Nonetheless, the change in the energy distribution would be considerably small and wavenumbers related to the decay region may remain stable due to the considerable influence of surface tension. Also, Tennekes and Lumley (1972) discussed that due to continuity, when an eddy uplifts, some backflow is likely to occur, keeping the net mass flux zero and hence producing a negative correlation at large distances, which results in a transverse spectrum with a peak away from the origin. However, use of a more complex spectrum is not justified as the aim is merely to filter out the energy associated to eddies larger than a certain wavelength.

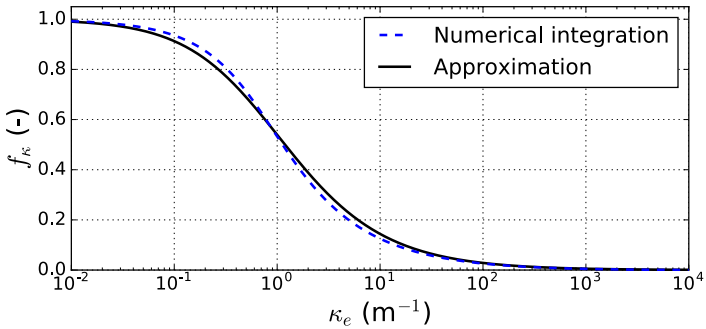

Fig. 8.2 Eddy filtering function f_k corresponding to the proportion of energy associated to a certain perturbation wavenumber κ_e. Numerical integration of Eq. 8.7 and 8.9; and approximation provided by Eq. 8.14.

An approximation to f_κ of Eq. 8.7 is proposed:

$$f_\kappa \approx \left(\frac{\alpha}{\alpha+\kappa_e}\right)^{5/3-0.94} \tag{8.14}$$

The agreement of this approximation with the numerical integration is shown in Fig. 8.2. Its accuracy has been tested for values of $\mathscr{L}_{zz}$ and $\overline{u_z'u_z'}$ in the range of those typical for spillway flows, obtaining always an absolute maximum error below 0.04 when compared to the numerical integration. Moreover, this absolute error compensates at both sides of $f_\kappa \approx 0.5$ and Eq. 8.14 satisfies $f_\kappa(\kappa_e = 0) = 1$. f_κ must be understood as a filtering function that expresses the percentage of the total turbulence quantities interacting with a given perturbation wavelength λ, i.e.: an eddy-perturbation interaction function.

It is remarkable that, in supercritical flows, $\mathscr{L}_{zz}$ is considerably smaller than in subcritical flows. This reduces the maximum E_{zz} values at the lowest wavenumbers while keeping the total energy integral constant for a given $\overline{u_z'u_z'}$ value. This results in higher values of f_k and can explain, together with the higher velocities and the corresponding $\overline{u_z'u_z'}$, why self-aeration is rarely observed in other than supercritical flows.

Finally, an estimation of the value of $\overline{u_z'u_z'}$ approaching the free surface is required. This flow quantity will depend on the type of shear flow under consideration and experimental data can be necessary (or, alternatively, a turbulence model). For flows

over smooth chutes, exponential fit of Nezu (1977), see Eq. 5.7, with coefficients of Nezu and Rodi (1986)[3] yield:

$$\sqrt{\frac{\overline{u_z' u_z'}}{u_*^2}} \approx 1.23 \exp\left(-0.67 \frac{z}{\delta}\right) \tag{8.15}$$

It must be noted that, differently from the shear stresses, normal velocity fluctuation do not vanish at depths larger than the boundary layer thickness (Valero and Bung, 2016). The air drag effect could also explain the free surface roughness far upstream of the boundary layer thickness intersection with the free surface.

Additionally, given Eq. 8.15 and general boundary layer theory (White, 2006), a relation between the spillway roughness (represented by the skin friction coefficient C_f) and the turbulence effect can be established:

$$\overline{u_z' u_z'} \sim u_*^2 = u_{fs}^2 C_f / 2 \tag{8.16}$$

which entails that when the spillway roughness is increased, not only the boundary layer will grow faster but also the turbulence quantities for a given free stream velocity and depth. This results in an earlier self-aeration trigger or even in self-aeration where, for smaller C_f values, would not occur.

[3] See Tables 5.1 and 5.2, together with Eq. 5.7, for similar coefficients from different studies and an uncertainty estimation.

Finally, the force produced in the water region by the apparent stresses can be computed by integrating Eq. 8.2 over the submerged surface of the control volume. If the velocity fluctuation does not vary significantly over $\mathbb{S}_\Lambda$, a good approximation can be obtained by using the normal velocity fluctuation at the center of gravity of the lower surface area $z = \overline{h} - 2\Lambda/\pi$ and multiplying by the vertically projected area (which coincides with $\mathbb{S}_b$):

$$F_{\tau wz} \approx \rho_w \mathbb{S}_b f_\kappa \overline{u_z' u_z'}, \qquad \text{at} \quad z = \overline{h} - \frac{2\Lambda}{\pi} \tag{8.17}$$

At the air region, shearing due to air and water velocity differences will induce normal velocity fluctuations as well. For this situation, limited studies are available. An approximation can be done based on experimental data (see Fig. 5 of Longo and Losada, 2012):

$$\frac{\overline{u_z' u_z'}}{u_{fs}^2} \approx 0.0115 \tag{8.18}$$

In Longo and Losada (2012), $\overline{u_z' u_z'}$ holds constant for the air region that is close to the waved surface. Differently from the water case, the lengthscale of the turbulence will remain small and, consequently, no reduction as proposed with Eq. 8.7 should be necessary. Therefore, the constant estimation of Eq. 8.18 can

be directly multiplied by the projected vertical area to obtain the turbulent stresses force:

$$F_{\tau az} \approx 0.0115\, \rho_a\, \mathbb{S}_b\, u_{fs}^2 \tag{8.19}$$

Equations 8.17 and 8.19 constitute the turbulence contribution to Eq. 8.1, as decomposed in Eq. 8.4.

8.3 Force due to surface tension

The vertical component of the surface tension force $F_{\sigma z}$, due to the free surface curvature, can be computed by integrating the Laplace formula (Landau and Lifshitz, 1987) which provides the distribution of pressure (p_σ) over the perturbation's crest surface:

$$p_\sigma = \sigma \left(\frac{1}{R_x} + \frac{1}{R_y} \right) \tag{8.20}$$

where R_x and R_y are the radii of curvature in the coordinate directions parallel to the mean free surface. Provided that the shape of the perturbation's crest is known, these radii can be computed. This estimation considerably simplifies when the perturbation's surface only deviates slightly from the mean free surface level. In such case, the right-hand side terms of Eq. 8.20 can be written in the most commonly known form (Laplacian equation):

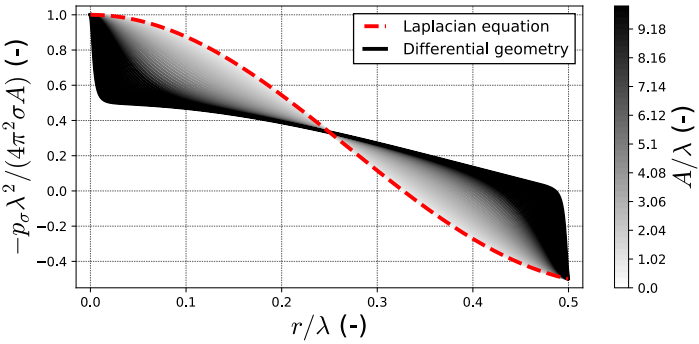

Fig. 8.3 Radial distribution of pressure over the perturbation's crest. Comparison between the small displacements assumption (Eq. 8.21) and the differential geometry approach (Eq. 8.22).

$$\frac{1}{R_x} + \frac{1}{R_y} = -\left(\frac{\partial^2\eta}{\partial x^2} + \frac{\partial^2\eta}{\partial y^2}\right) \tag{8.21}$$

whereas for large displacements, use of differential geometry (Abbena et al., 2006) becomes necessary to accurately determine the surface curvatures. Then, curvature radii can be estimated as:

$$R_x = -\frac{\left[1+(\partial\eta/\partial x)^2\right]^{3/2}}{\partial^2\eta/\partial x^2}; \qquad R_y = -\frac{\left[1+(\partial\eta/\partial y)^2\right]^{3/2}}{\partial^2\eta/\partial y^2} \tag{8.22}$$

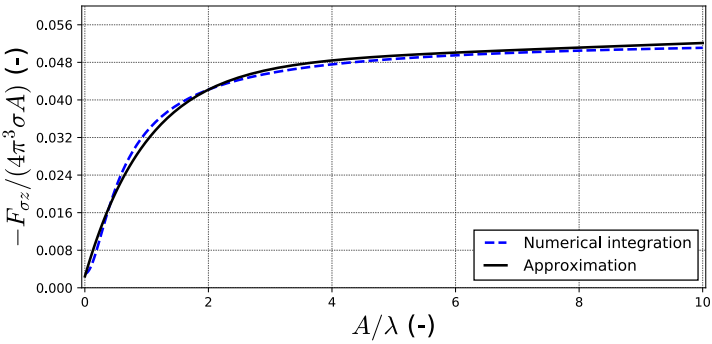

Fig. 8.4 Vertical force due to surface tension varying with the perturbation's amplitude and steepness. Numerical integration of Eq. 8.23 and approximation of Eq. 8.24. Maximum absolute difference occurring is 0.002.

The necessary relations to estimate the radii of curvature (either by using Eq. 8.21 or 8.22) are provided in a simple form in Appendix B.

Figure 8.3 shows significant differences between the use of Eqs. 8.21 and 8.22 in the solution of Eq. 8.20. Differences are evident even for small A/λ ratios, which suggest that for self-aeration related problems, approach of Eq. 8.22 might be preferable.

Finally, $F_{\sigma z}$ can be computed by integrating the pressure obtained with Eqs. 8.20 and 8.22 over the vertical component of the surface of the perturbation's crest:

$$F_{\sigma z} = \int p_\sigma \, n_z \, \mathrm{d}\mathbb{S}_A = p_\sigma \, \mathrm{d}\mathbb{S}_b \tag{8.23}$$

The result of the numerical integration (using Simpson's rule and integrating using radial coordinates) of Eq. 8.23 is shown in Fig. 8.4. For easiness of computation, an approximation is also proposed:

$$F_{\sigma z} \approx -4\pi^3 \sigma A \left\{ a_1 + a_2 \exp^{(-A/\lambda)} + \log_{10}\left(1 + \frac{A/\lambda}{a_3}\right) \right\} \tag{8.24}$$

with $a_1 = 0.0484$, $a_2 = -0.0464$ and $a_3 = 2068$.

8.4 Force due to gravity

Gravity is a body force acting homogeneously distributed over the control volume, affecting both the perturbation's crest and submerged body. As the coordinate system is defined parallel to the free surface, another body force acting on the control volume due to a change in the flow curvature would need to be considered (for instance, in a free-falling jet). For the sake of simplicity, trajectory changes are not addressed in this study but could be considered as a reduction or increment on the net gravity (g'):

$$g' = g + f \tag{8.25}$$

with f the non-inertial acceleration of the center of gravity of the perturbation. Thus, in a free falling jet only the surface tension term would be countering the turbulent forces[4], given that $f = -g$.

Nevertheless, the force due to the gravity over the total volume of the perturbation ($\mathbb{V}_p = \mathbb{V}_M + \mathbb{V}_m$) can be expressed as:

$$F_{gz} = \int \rho_w \, g_z \, \mathrm{d}\mathbb{V}_p = (M + m) \, g_z = M_p \, g_z \tag{8.26}$$

being g_z the z component of the gravity acceleration and taking a negative value for the defined coordinate system. M and m were analytically obtained in Eqs. 7.6 and 7.3 respectively.

8.5 Force due to pressure

The pressure field inside the perturbation would follow a Poisson type equation depending on the velocity field, as can be derived from the governing flow equations (Davidson, 2015; Pope, 2000). However, integration of this equation for each A/λ would result

[4]This can result in the sudden aeration of jets in sky jumps. Aeration would be observed near the section where the jet departs from the hydraulic structure.

excessively complicated and would require assuming a velocity distribution that would also hold a large uncertainty. Provided the lack of experimental and numerical data, some assumptions become necessary.

Under hydrostatic conditions, the pressure exerted by the fluid under the perturbation submerged body would be countering the gravity force F_{gz}. It can be expected that for low A/λ ratios this is a reasonable assumption. Nonetheless, as the geometry distorts, the pressure field may be greatly affected by the changes in the trajectory of the fluid particles. Additionally, considering the perturbation as a mass of water about to depart from the water body, something behaving more "disconnected" from the main water flow than a hydrostatic distribution could be expected.

Herein, it is proposed that the gravity force affecting the submerged body is completely countered due to the hydrostatic pressure, but not at the crest (which remains over the mean free surface depth). Thus, it can be written:

$$F_{pz} = -M\,g_z \tag{8.27}$$

This results in a positive force as $g_z < 0$ (unstabilizing effect of pressure). Eqs. 8.26 and 8.27 could be expressed together as a net stabilizing force:

$$F_{gz} + F_{pz} = m\,g_z \tag{8.28}$$

Therefore, the bigger the perturbation, the more the gravity stabilizes it. More accurate assumptions would require further experimental insight. The proposed hypothesis is in agreement with other energetic methods which consider all the perturbation height to be stabilizing.

Partial conclusions

Part III is the kernel of this dissertation. It is divided into two chapters, the first one (Chapter 7) is dedicated to obtaining the necessary equations governing the turbulent motion of a free surface, the second one (Chapter 8) aims to approximate, as accurately as possible, the forces acting over the free surface perturbations.

In Chapter 7, a simple geometry was proposed for the free surface perturbations (Eq. 7.1) which allowed the formulation of a kinematic relation (Eq. 7.25) and a momentum based non-linear dynamic equation (Eq. 7.26). The proposed perturbation geometry is tangent to the free surface and presents radial symmetry. It is, therefore, a three-dimensional perturbation.

The related geometry parameters (k_A, k_Λ, k_m, k_M and k_{in}) were analytically obtained. These coefficients can be adjusted to fit new experimental evidences without modifying the implications of the derived equations. A few assumptions were made

which must be borne in mind (see Eq. 6.4). Additionally, it is assumed that perturbations only grow with amplitude and do not interact with other perturbations travelling nearby.

In Chapter 8 forces related to turbulence, surface tension, gravity and pressure were studied. It has been argued that turbulence quantities approach the free surface not being significantly modified. This is consistent with the theoretical framework of Hunt and Graham (1978) and Teixeira and Belcher (2000), as far as the studied wavelength is considerably bigger than the viscous region ($\lambda \gg \delta^{\nu}$). In common hydraulic structures flows, this is satisfied by all the wavelengths over a few millimetres and the most unstable wavelengths are likely to be greater.

By proposing a model spectrum (E_{zz}, see Eq. 8.9), a filtering function could be obtained, which accounts for the eddy-perturbation interaction (f_{κ}, see Eq. 8.14). This is a new concept herein introduced which, basically, traduces to: large turbulent structures will produce big waves (in a similar scale) and small turbulent structures will produce waves with smaller lengthscales; hence, perturbations will surf over eddies considerably bigger as they surf over the mean flow.

Different unresolved aspects from self-aeration were explained by the presented mathematical derivations, as why supercritical flows are prone to self-aeration – which is linked to the energy distribution of the turbulence spectrum, in addition to the higher absolute values of turbulence – or the key role of velocity

fluctuations normal to the free surface, which is a turbulent term that does not vanish at $z = \delta$ and that scales with the spillway roughness (Eq. 8.16). The secondary role of shear stresses in perturbation's growth was also disclosed, being only relevant for very large wavelengths.

Whereas isotropy is assumed for the submerged body of the perturbation, the transverse lengthscale is taken from the open channel flow experimental study of Johnson and Cowen (2016), which reflects the large degree of anisotropy of the flow. Turbulence quantities are estimated on the basis of the study of Nezu and Rodi (1986), which also reflects the flow anisotropy.

It has been shown the significant difference on the assessment of surface tension effect between the small displacements formulation and the more rigorous differential geometry approach. Assumptions on the pressure distribution are simplistic, despite they may reproduce the overall physics of the phenomenon and are consistent with previous existing energetic analyses. When changes in the perturbation occur, non-inertial accelerations have to be considered up to the extreme case of a free falling jet, where surface tension becomes the only stabilizing force.

All in all, the theoretical developments here presented constitute a new conceptualization of self-aeration which aims to shed light on some air entrainment unresolved questions. Accounting for the experimental evidence of Ervine (1998) showing that air entrainment on impinging jets depends on the free surface per-

turbations size of the impacting flow, the proposed formulation may also help to reduce the involved uncertainty on the entrained air volumes for partially developed flow conditions in hydraulic jumps or plunging jets. Also, study of the most unstable wavelengths can lead to a better interpretation and prediction of the expected scale effects related to self-aeration on reduced physical models. The proposed formulation can be of interest on the study of the linkage between free surface distortion and the turbulence occurring underneath.

Part IV

Application and empirical evidences

Chapter 9

Prototype scale spillway: the Aviemore dam

9.1 Study of Cain (1978)

Air entrainment is greatly affected by scale effects (Chanson, 2009; Felder and Chanson, 2009, 2017; Heller, 2011), being one of the most complex problems studied in hydraulics, simultaneously involving Froude, Reynolds and Weber number similarities (or alternatively, the Morton number). Recently, Felder and Chanson (2017) presented two experimental cases with both undistorted Froude and Reynolds similitudes, concluding that extrapolation of some parameters, even from large-scale reduced models, to prototype scale might not be possible. Therefore,

in order to test the capabilities of the proposed model, using prototype scale becomes of utmost interest.

Cain (1978) conducted air-water flow measurements in the spillway of the Aviemore dam (shown in Fig. 9.1), located at the Waitaki River, New Zealand. Data of Cain (1978) constitutes, up to now, one of the few available datasets at full prototype scale. The Aviemore spillway is a 1:1 slope spillway with a concrete surface of roughness $k_s \sim 1.5$ mm. The drop height was roughly 37 m during the tests. More information on the geometry of the spillway and the instrumentation used can be found in Cain (1978).

The tests, after serious limitations due to water release restrictions – no spillage occurred within three years prior to the initial tests in April 1975 –, were finally conducted on January 1976. Cain (1978) reported, among other data, the inception point distance L_i for two different gate openings (Table 9.1). Both gate openings were contemplated in the present study: 300 and 450 mm; leading to flow depths immediately downstream of the gate of 196 and 280 mm respectively. Each gate opening corresponds to a specific flow rate of $q = 2.23$ m^2/s and $q = 3.15$ m^2/s. Similarly to the original study (see Fig. 11.3 of Cain, 1978), here the inception point distance is presented as the distance from the gate. For the gate openings considered, this distance was 7.6 m and 13 m (see Fig. 9.2).

Table 9.1 Flow conditions at the Aviemore spillway during tests of Cain (1978). Roughness Froude number (F_*) as defined by Eq. 3.5.

Gate opening (mm)	q (m^2/s)	L_i (m)	F_* (-)	L_i/k_s (-)
300	2.23	7.6	14582	5067
450	3.15	13	20598	8667

Fig. 9.1 Aviemore dam under controlled water release. Notice the spatial variability of the inception point, leading to a considerable uncertainty on its determination. Photograph courtesy of the Otago Daily Times, NZ (reproduced with permission).

9.2 Mean flow depth

For the mean flow depth determination, integral boundary layer approach of Castro-Orgaz and Hager (2010) and Castro-Orgaz (2010) was used with the default parameters obtained from spillway type flows. Numerical integration was performed by using a Runge-Kutta fourth order method. The main advantage of this approach is that it allows simultaneous determination of the boundary layer thickness and the shear velocity u_*, which are both necessary to estimate the normal velocity fluctuations[1].

Water density was taken as $\rho_w = 998$ kg/m^3, water dynamic viscosity $\mu_w = 0.001$ kg/m s, air density $\rho_a = 1.0$ kg/m^3, air-water surface tension $\sigma = 0.0729$ N/m and gravity acceleration $g = -9.8$ m/s^2.

As it can be observed in Fig. 9.2, turbulent boundary layer of Castro-Orgaz and Hager (2010) yields a result similar to Bauer (1954) and Keller and Rastogi (1975) for the intersection of the boundary layer with the free surface. The latest values were directly extracted from Cain (1978). However, and as it is noticed often in literature (see discussion of Valero and Bung, 2016), self-aeration was observed to occur upstream from this intersection.

[1] See Eq. 5.7, Tables 5.1 and 5.2, and Fig. 5.1. In this section, Eq. 8.15 was used, thus accounting for Nezu and Rodi (1986) fit.

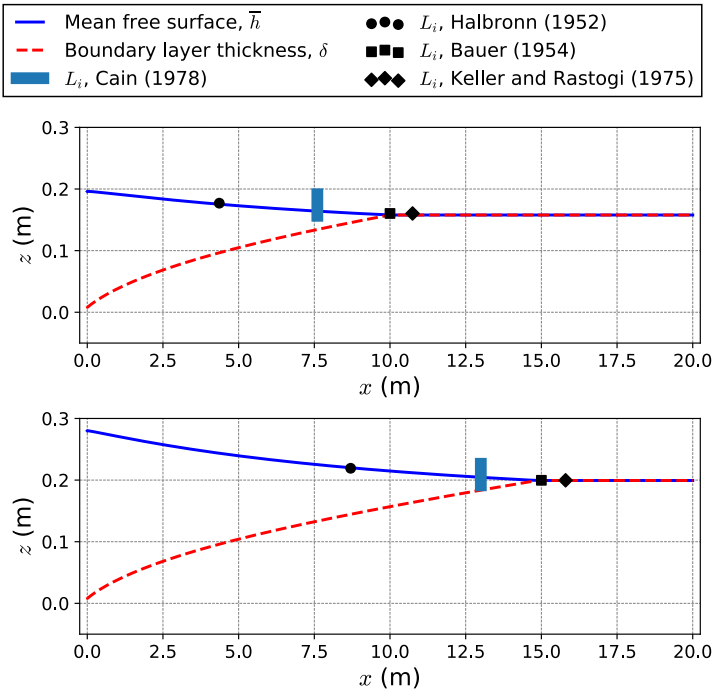

Fig. 9.2 Mean free surface ($\overline{h}$) and boundary layer thickness (δ) obtained using the integral boundary layer approach of Castro-Orgaz and Hager (2010). Inception point observation of Cain (1978). Intersection of the mean free surface with boundary layer approaches of Halbronn (1952), Bauer (1954) and Keller and Rastogi (1975), as extracted from Cain (1978). Top: gate opening of 300 mm. Bottom: gate opening of 450 mm.

9.3 Perturbations growth

For the free surface perturbations growth, kinematic Eq. 7.25 was numerically solved using an explicit Euler scheme. The coefficient k_p was estimated without simplifications, as defined in the quasilinear Eq. 7.12. Perturbations dynamics were computed by numerically solving Eq. 7.26. The streamwise velocity of the perturbations (u_p) was taken to be equal to the free stream velocity u_{fs} (Eq. 7.24). Both the perturbation amplitude (A) and its normal velocity (v_p) – which are the main variables of the system of equations – were initially set to zero at $x = 0$ m (gate location) and forces were evaluated using the previous step values of the flow variables. The spatial step for the numerical integration was $\Delta x = 0.2$ mm, which is small enough to yield a solution insensitive to Δx.

Vertical forces were approximated using Eq. 8.17 for the turbulent force at the water region (and necessarily Eq. 8.15 and the approximation of Eq. 8.14 for the eddy-perturbation interaction function, Eq. 8.10 for the transverse lengthscale), Eq. 8.19 for the turbulent velocity fluctuation force at the air region, Eq. 8.24 for the surface tension force and Eq. 8.28 for the gravity and pressure forces effect.

In the following analysis, special emphasis is given to the Taylor wavelength (λ_c) value of Eq. 6.3, but a wide range of λ values was analysed as well. As the maximum unbounded

lengthscale taking place should be in the order of the flow depth, maximum λ value was limited to the minimum flow depth in the spillway.

9.4 Results

The perturbations grow as they are inflated by turbulence and some wavelike behaviour can be observed with a period different for each wavelength (note that each line in Fig. 9.3 is a different wavelength). It can be observed that small wavelengths ($\lambda \ll \lambda_c$) do not grow significantly as they are effectively stabilized by surface tension. This is consistent with the discussion provided in Chapter 6 and by Ishii and Hibiki (2010) on wavelengths smaller than λ_c.

The most unstable wavelengths observed are in the order of λ_c. However, flow cases with different lengthscales ($\mathscr{L}_{zz}$) would present a different distribution of turbulent normal stresses (see Eqs. 8.9 and 8.12), thus affecting the most unstable wavelength value. Most unstable wavelength is assumed to be that with higher steepness.

Waved patterns shown in Fig. 9.3 resemble those which can be visually observed in spillway studies in the non-aerated region; both at stepped spillways (see Fig. 2 of Zhang and Chanson, 2016a,c) and smooth spillways (Figs. 1.3 and 6.1).

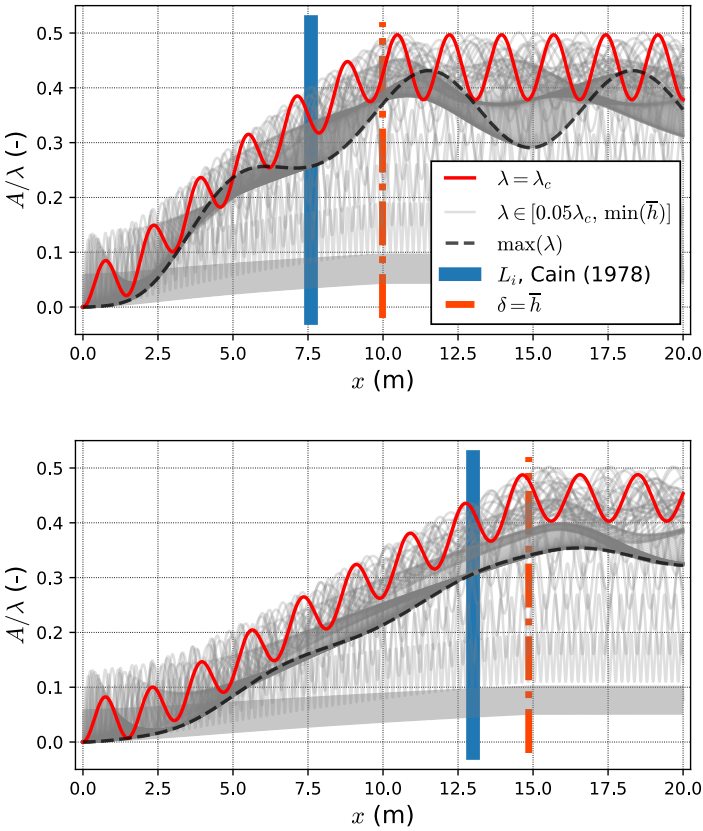

Fig. 9.3 Perturbation growth through the spillway for different wavelengths. Each line corresponds to a different wavelength. Top: gate opening of 300 mm. Bottom: gate opening of 450 mm.

The growing free surface roughness shown in Fig. 9.3 is also consistent with experimental observations of Meireles et al. (2012) and Valero and Bung (2016) for spillway flows: rough free surface with constant growth at the beginning and a faster growing region near the inception point location.

It can be observed in Figs. 9.3 and 9.4 that, for both gate openings, the inception point location occurred at roughly $A/\lambda \approx 0.40$ to 0.44 (Table 9.2), which suggests a larger S_{lim} than those commonly reported for gravity waves (0.14 to 0.17, as suggested by Toffoli et al., 2010), but in the range of surface tension dominated waves (Fig. 9.5).

These breaking steepness are also consistent with experimental observations in spillway flows (e.g., in Fig. 6.1 can be already observed A/λ larger than 0.14 to 0.17) and with bounds defined by the numerical study of Deike et al. (2015) for spilling breakers.

It must be noted that, if instead of using turbulence approximation of Nezu and Rodi (1986), coefficients of Table 5.2 were used, the breaking steepness S_{lim} would have fallen slightly below in Fig. 9.5.

Another issue to consider is that perturbations could already be unstable upstream of the observed inception point location but still propagate a few portions of a period farther downstream (given the high velocities at which they are advected, a considerably large distance) before finally observing droplets and bubbles.

Table 9.2 Most unstable wavelengths for the Aviemore spillway case study at the inception point location.

Gate opening (mm)	λ/λ_c (-)	λ (cm)	$S = A/\lambda$ (-)
300	1.08	1.86	0.40
450	1.02	1.74	0.44

In that case, a large range of lengthscales at the inception point would correspond to wavelengths remaining at unstable configurations when the final breakup occurs.

For both gate opening flow cases, the most unstable wavelength at $x = L_i$, with L_i the observation of Cain (1978), was close to the Taylor wavelength ($\lambda \approx \lambda_c$). However, for the first meters of the spillway where only the air drag distorts the free surface, λ slightly smaller prevailed.

There is not enough evidence on the most unstable wavelength for every flow case; despite for the considered flow cases, as it can be observed in Fig. 9.3, results for the Taylor wavelength described well the overall trend of the most unstable wavelength all through the non-aerated region of the smooth spillway.

The distribution of steepness by wavenumber is shown in Fig. 9.4. The minimum wavenumber corresponds to the bigger perturbation wavelength, which is assumed to be constrained by the flow depth.

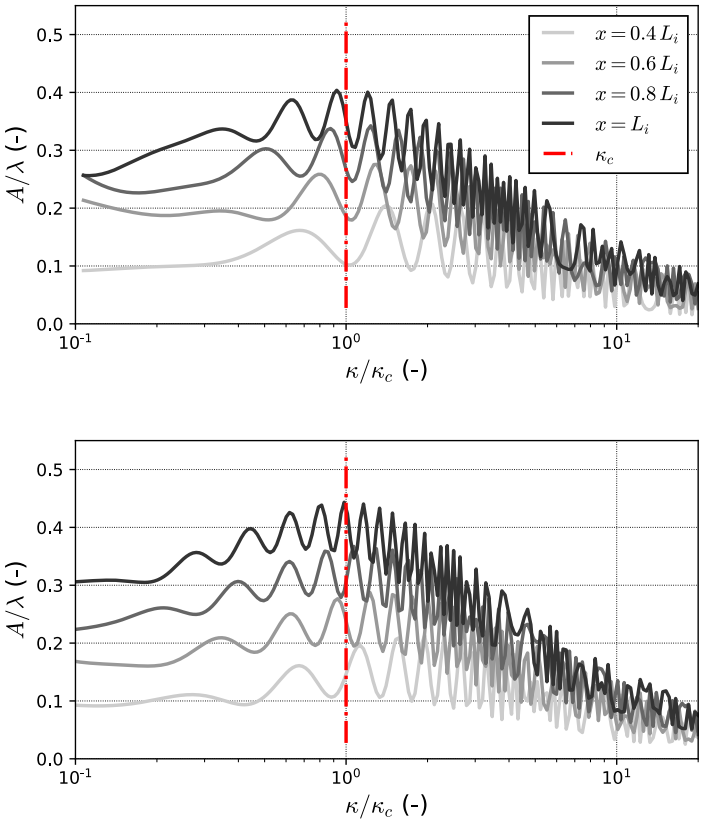

Fig. 9.4 Steepness distribution at different streamwise locations. L_i from Cain (1978) observation. Top: gate opening of 300 mm. Bottom: gate opening of 450 mm.

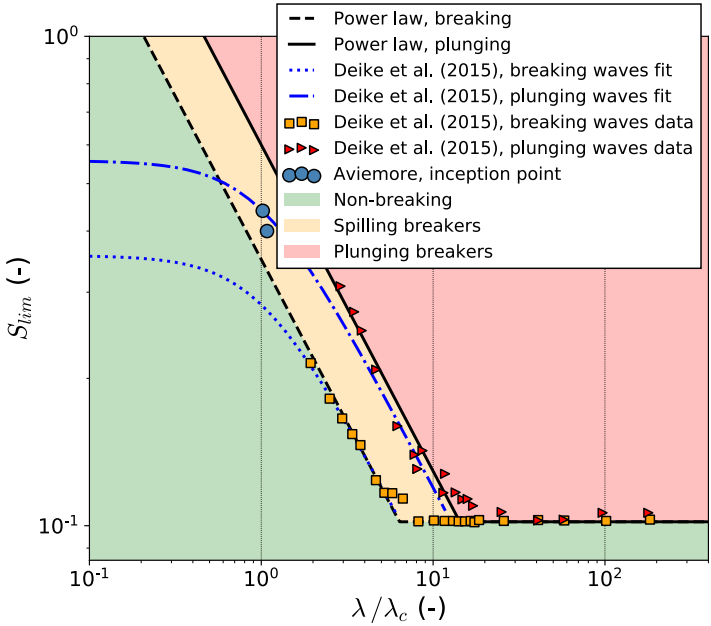

Fig. 9.5 Breaking steepness at the inception point for the Aviemore spillway case. Black lines for: breakup steepness of Eq. 6.10, plunging steepness of Eq. 6.11 and asymptotic limit of Eq. 6.12. DNS data of Deike et al. (2015) on waves subject to capillary effects.

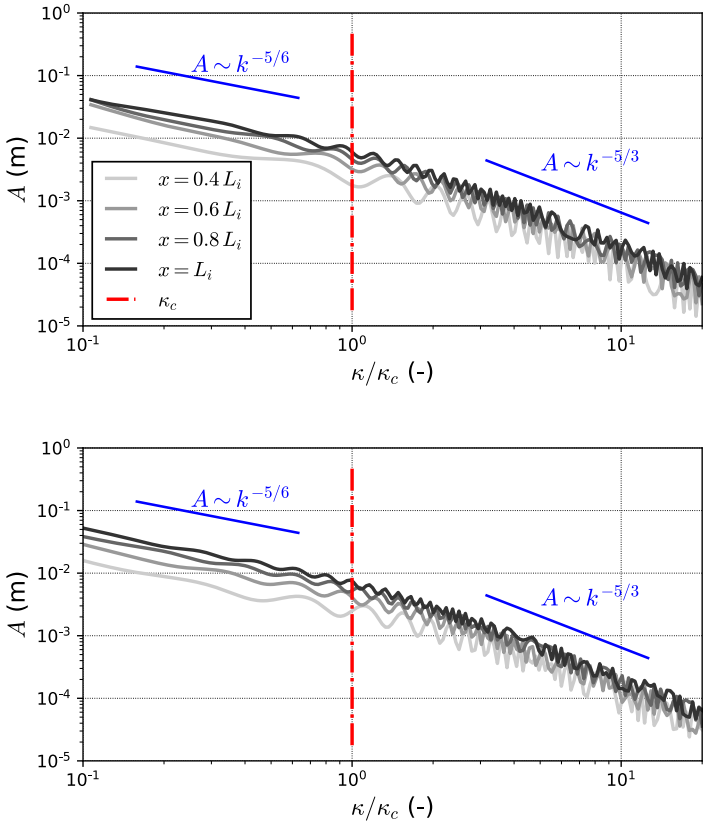

Fig. 9.6 Amplitudes spectra at the Aviemore spillway. Top: gate opening of 300 mm. Bottom: gate opening of 450 mm.

In scaled models, when the flow depth dimension limits the more unstable wavelength, important scale effects shall be expected, as deduced from the presented theoretical analysis: smaller wavelengths or higher wavenumbers are more effectively stabilized by surface tension, as observed in Figs. 9.4 and 9.5.

For the sake of completeness, amplitudes distributions are presented in Fig. 9.6. Two different scaling behaviours can be observed. For $\lambda \gg \lambda_c$:

$$A \propto \kappa^{-5/6} \tag{9.1}$$

whereas, for $\lambda \ll \lambda_c$:

$$A \propto \kappa^{-5/3} \tag{9.2}$$

Thus, the full distribution of amplitudes could be determined by just resolving the case for the most unstable wavelength (when *a priori* known) or two different wavelengths belonging to both different regions. Given that $\eta \sim A$, the same conclusions can be drawn for the distribution of free surface roughness. Figure 9.6 also implies that there is an order, or structure, for the free surface roughness. How this propagates to the self-aerated region, is still to be investigated.

Chapter 10

Large scale spillway: The University of Queensland

10.1 Presentation

The theoretical framework derived in Part III allows for the computation of free-surface dynamics up to the extreme case of self-aeration. There are, however, many reasonable hypotheses embraced which could limit the applicability of the formulated equations. The case study presented in Chapter 9 cannot be understood as a validation, but just as a test of the equations' capabilities.

Nonetheless, many of the results described in Section 9.4 matched previous experimental observations reported in literature. Unfortunately, no specific tests have been conducted in the past to gain insight on some of the most relevant variables brought to light in the past chapters. With the focus put on the free surface dynamics, it seems of utmost relevance to study water level fluctuations in large scale applications.

Excellent inlet conditions are thus necessary to avoid advecting any undesired perturbation from the inlet tank to the spillway flow, hence affecting the experimental observations. The stepped spillway facility herein studied (Fig. 10.1) is located at the Laboratory of Hydraulics of The University of Queensland (UQ), and meets well these characteristics, as the inlet reservoir is large enough to ensure that any disturbance dissipates before reaching the broad crested weir.

10.2 Experimental setup

The present chapter focuses on the non-aerated region of a large scale stepped spillway model of 45 ° slope (1V:1H). The stepped spillway has a wide inlet basin which ensures smooth inlet conditions (Zhang and Chanson, 2016a), a broad crested weir (0.60 m long, 0.985 m wide) which conveys the flow into the stepped spillway, of the same width, composed of steps of height s = 0.10 m (which leads to a cavity length of L_{cav} = 0.141 m). A thorough de-

Table 10.1 Investigated flow conditions at the UQ stepped spillway, with h_c being the critical depth, q the specific flow rate, $F_{*,v}$ the roughness Froude number as defined by Eq. 3.9, L_i the inception point (visual observation) distance from the first edge and k_v as defined by Eq. 3.8.

h_c/s (-)	q (m^2/s)	$F_{*,v}$ (-)	L_i/L_{cav} (-)	L_i/k_v (-)
0.9	0.0845	1.71	3	6
1.1	0.1142	2.31	4	8
1.3	0.1467	2.96	5	10
1.5	0.1819	3.67	6	12
1.7	0.2194	4.43	7	14
1.9	0.2593	5.24	8.5	17
2.1	0.3013	6.09	–	–

scription of this stepped spillway and a complete flow description can be found in Zhang and Chanson (2016a,b). The experimental setup is sketched in Fig. 10.1. Flow cases studied are presented in Table 10.1.

Free surface measurements were dynamically obtained with three microsonic^{TM} Ultrasonic sensors (USS)[1] mic+25/IU/TC. The measuring range recommended by the provider ranges from 30 to 250 mm. The near field of the USS was enclosed with PVC cylinders of the same diameter to prevent the sensors from wetting. This artefact did not affect sensors' recordings, as reported by Kramer and Chanson (2018).

[1] Also known as Acoustic Displacement Meters (ADM).

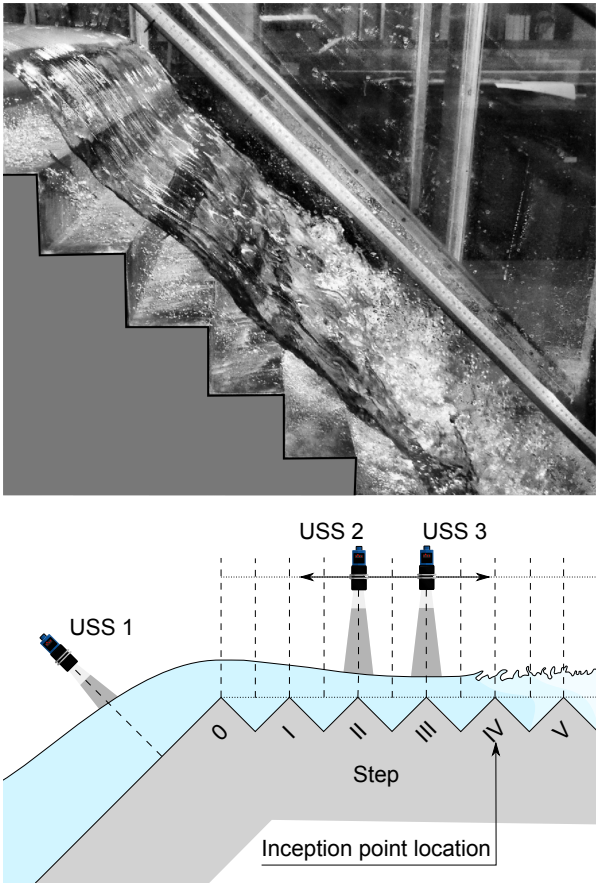

Fig. 10.1 Experimental setup at UQ: (top) Stepped spillway, image taken at 1/1000 shutter speed, processed with Contrast-Limited Adaptive Histogram Equalization (CLAHE, see Bung and Valero, 2015; González et al., 2004); (bottom) Sketch of the experimental setup (rotated 45 ° counterclockwise), steps numbering and sensors measurements location (– –). Flow from left to right.

The USS provide a voltage time series, which can be correlated to a distance to obtain a water level. The three USS were calibrated over a distance range covering the expected water depths to be measured. Calibration was conducted by recording during 300 s at 100 Hz at 11 different distance levels, which covered the range of expected flow depths. Figure 10.2 shows that calibration exhibited a linear relation over the entire sampled range and that the Standard Deviation (STD) of each calibration measurement remained close to 0.10 mm, being this value the accuracy specified by the sensor provider.

The USS 1 was located at a fixed position over the crest, at 0.17 m upstream of the edge of the first step (Step 0, Fig. 10.1). The other two sensors (USS 2 and USS 3) were located over the stepped geometry, separated a distance L_{cav}. Maintaining the distance between sensors constant, both USS 2 and USS 3 were placed parallel to the pseudobottom formed by the step edges, allowing measurement of the flow depths at different spillway locations.

Measurements were conducted both above step edges, for steps 0 to VII, and above step cavities (mid distance between the step edges), as marked in Fig. 10.1. Each recording was conducted at a sampling rate of 100 Hz during 600 s. The total time recorded is shown in Fig. 10.3. Differences occur due to two reasons: overlapping of measurement locations, as the USS

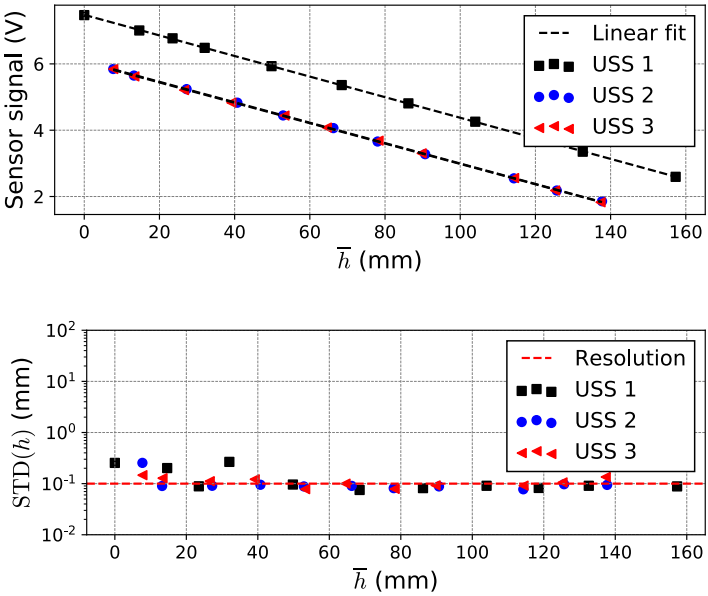

Fig. 10.2 USS performance: (top) calibration curves and (bottom) noise level measured during the USS' calibration curves for a static measurement ("resolution" for the noise level reported by the manufacturer, 0.1 mm).

sensors are moved together, and repetition of some measurements at locations where the free surface was highly roughened.

In Fig. 10.3, the inception point location is marked according to the visual observation of Zhang and Chanson (2016a) and two independent observers. For completeness, empirical formulas estimations of Meireles et al. (2012) and Chanson et al. (2015) are included. Meireles et al. (2012) estimated the inception point location through air concentration profiles. Discussion on differences between visual and air concentration based inception point estimations can be found in Meireles et al. (2012). As shown in Fig. 10.3, all the measurements correspond to the non-aerated region, where the free surface gradually roughens (Felder and Chanson, 2014; Meireles et al., 2012; Valero and Bung, 2016).

10.3 Results

10.3.1 Filtered data

Data has been filtered following the Robust Outlier Cutoff technique proposed in Appendix C. Figure 10.4 shows that close to the first step (step 0) large percentages of data were rejected. This may be explained by the inclination of the detection zone axis of the USS with the normal to the free surface, as the free

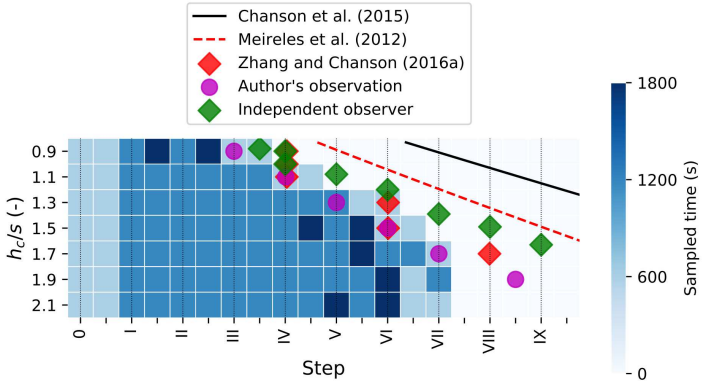

Fig. 10.3 Measurements distribution and sampled time for the studied flow conditions. Visual observation of the inception point location (Zhang and Chanson, 2016a) and empirical formulas of Meireles et al. (2012) and Chanson et al. (2015). Visual observations of the author and an independent observer for completeness, showing the uncertainty involved in the inception point observation.

surface curves at the transition from the broad crested weir to the spillway, resulting in a large amount of lost echoes.

With increasing discharge, the flow depth becomes sensibly parallel to the pseudobottom, differently than for lower discharges for which the flow depth curves encompassing the step edges. Hence, with increasing flow discharge, the normal of the free surface tends to be closer to the axis of the measuring cone of the USS, resulting in fewer outliers in the recorded data. Close to the inception point of self-aeration, the free surface considerably roughens and its dynamic determination can be more challenging for the USS, consequently resulting in a local increase of the outliers contained in the recorded dataset (Fig. 10.4).

10.3.2 Drawdown curve

The median flow depths show a typical drawdown curve for a skimming flow in a stepped spillway (see Fig 10.5). In Fig. 10.5, lighter markers correspond to lower flow rates, which are closer to the transition flow regime. The bump shown in the profile for lower x values ($x/h_c < 1$) corresponds to the change of slope from the broad crested weir to the first step (see Fig. 10.1).

10.3.3 Perturbations growth rate

Flow depth fluctuations (h') have been obtained as the STD of the filtered flow depth time series. Figure 10.6 shows the growth

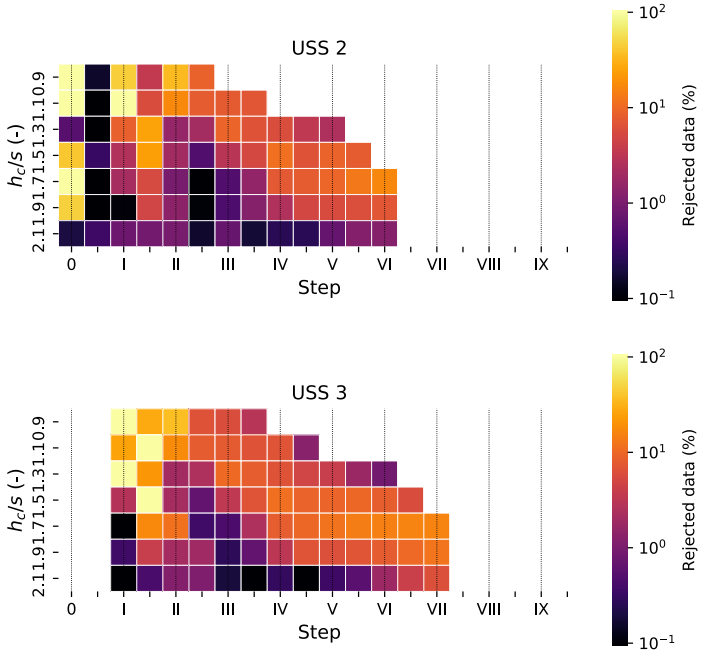

Fig. 10.4 Percentage of rejected data after applying ROC filtering for both USS located over the pseudobottom (USS 2 and USS 3, as positioned in Fig. 10.1).

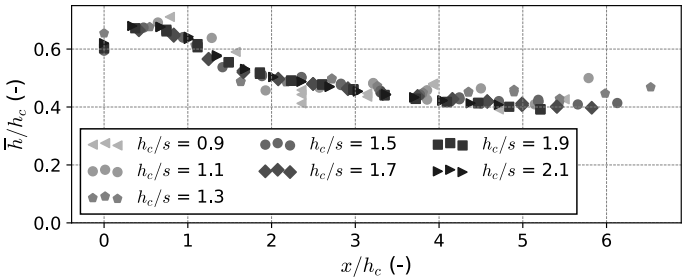

Fig. 10.5 Drawdown curve for the measured flow conditions.

of the free surface perturbations through the spillway. It is remarkable that free surface fluctuations are nearly null at the first sections, resulting from the smooth inlet conditions. Values of h'/h_c did not show any data collapse, but dimensional fluctuations did (i.e., h'). Regardless of the dimensionless form, free surface oscillations showed a clear positive growth trend with increasing streamwise distance, similarly to both flow cases previously considered in the Aviemore spillway study (see Fig. 9.3) and the smooth chute flow cases considered in the FH Aachen facility (Fig. 5.11).

Immediately after $x/h_c > 1$, there is a local increase in the free surface fluctuations which might be due to the flow impact after the change of slope. These fluctuations do not sustain and a reattachment to the main perturbations' growth trend can be observed at around $x/h_c \approx 2$.

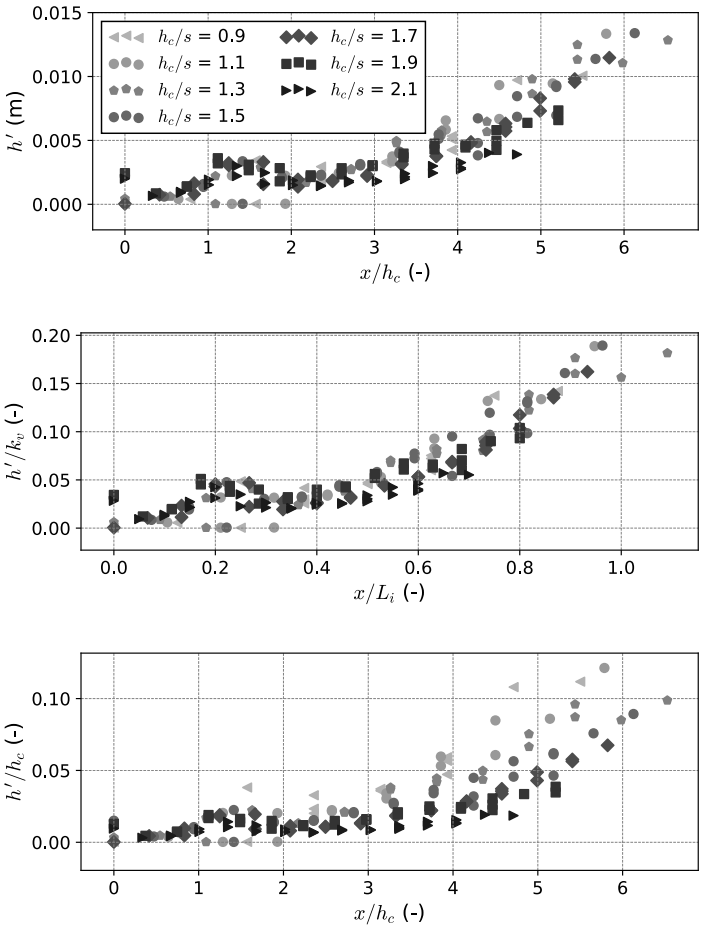

Fig. 10.6 Free surface fluctuations at the UQ setup.

10.3.4 Free surface fluctuations spectra

The one-dimensional spectrum can be defined as (Pope, 2000):

$$E_{\eta\eta} = \frac{2}{\pi} \left\langle \eta^2 \right\rangle \int_0^\infty R_{\eta\eta}(\varsigma) \cos(f\varsigma)\, \mathrm{d}\varsigma \tag{10.1}$$

being $R_{\eta\eta}$ the autocorrelation function of η, ς is the time lag, f the frequency and the expected value of η^2 can be computed using h'. Rejected data was substituted by linear interpolation between the neighbouring points for the computation of the free surface spectra.

In the following, spectra were obtained by means of the well-known Welch (1967) method using the Hann window, as implemented in the SciPy library (Python 2.7). Given the nature of the employed instrumentation, only temporal spectra could be directly estimated. Nonetheless, it must be noted that given a constant advection velocity for perturbations of all wavelengths (e.g., $u_p \approx u_{fs}$), analogy between time and spatial spectra could be done following:

$$\lambda f = u_p \tag{10.2}$$

or, similarly for the wavenumber:

$$2\pi f = \kappa u_p \tag{10.3}$$

Consequently, the following spectra can be compared to that shown in Fig. 9.6 for the Aviemore spillway, which was obtained using the Eqs. 7.25 and 7.26 and the forces approximation of Chapter 8. As USS 2 reported lower levels of rejected data (Fig. 10.4), preference is given to the recordings of USS 2 in the following analysis.

Experimental data examination suggested that three regions should be distinguished, depending on the observed type of spectra. In the first region (Region I, early non-aerated region), the free surface is first disturbed and amplitudes remain small. The spectra shows two power law slopes, with power law of $-5/6$ (Eq. 9.1) for the gravitational slope and $-5/3$ (Eq. 9.2) for the surface tension slope. It must be noted that these two slopes were obtained from the herein derived analytical formulation applied to a 45 ° slope spillway. Figure 10.7 shows spectra for four discharges with same power law scaling as the Aviemore spillway case previously analysed (see Fig. 9.6). The extension of this region holds roughly up to $x/L_i \approx 0.30$.

In the second region (Region II, mid non-aerated region), the gravitational slope starts flattering and some of the energy of this range moves to higher frequencies (Fig. 10.8), sometimes temporarily affecting the surface tension slope ($-5/3$), but it is always recovered a few sections downstream. Some accumulation of energy at the slope change can be often observed as well,

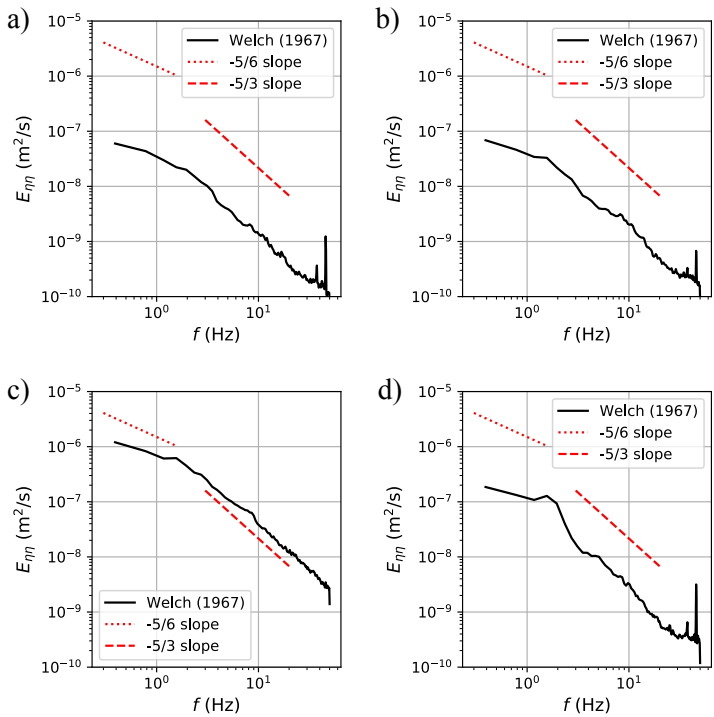

Fig. 10.7 Spectra at the early non-aerated region (Region I). a) $h_c/s = 1.3$ at $x/L_i = 0.09$, b) $h_c/s = 1.7$ at $x/L_i = 0.07$, c) $h_c/s = 1.9$ at $x/L_i = 0.23$ and d) $h_c/s = 2.1$ at $x/L_i = 0.10$.

with a considerable flattering (slope tending to zero) at the nearby slower frequencies.

In the third region (Region III, late non-aerated region), the gravitational slope reaches a null slope (Fig. 10.9), and the slope at the surface tension region ($-5/3$) has been completely recovered. No accumulation of energy at the slope change can be observed. Transition from Region II to III is not that clear as from Region I to II, although a reference value of $x/L_i \approx 0.70$ could serve as reference.

Overall, all the three regions described show that a structure exists, both in the frequency and wavenumber space, as it was previously deduced. Nonetheless, some of the hypotheses related to the bigger wavelengths may not hold valid when large amplitudes are reached.

From Region I to III, there is also a shift towards higher frequencies which could be simply explained by the acceleration of the flow (larger u_p yield larger frequencies for the same wavenumbers, see Eq. 10.3). For completion, classification of the spectra type observed for all the measurements, including both USS 2 and USS 3, are presented in Tables 10.2, 10.3, 10.4 and 10.5. Data of these tables is also summarized in Fig. 10.10. It must be noted that USS 3 was installed one cavity downstream from USS 2, which allowed insight on an additional cavity, while also resulted in missing data in the first upstream cavity.

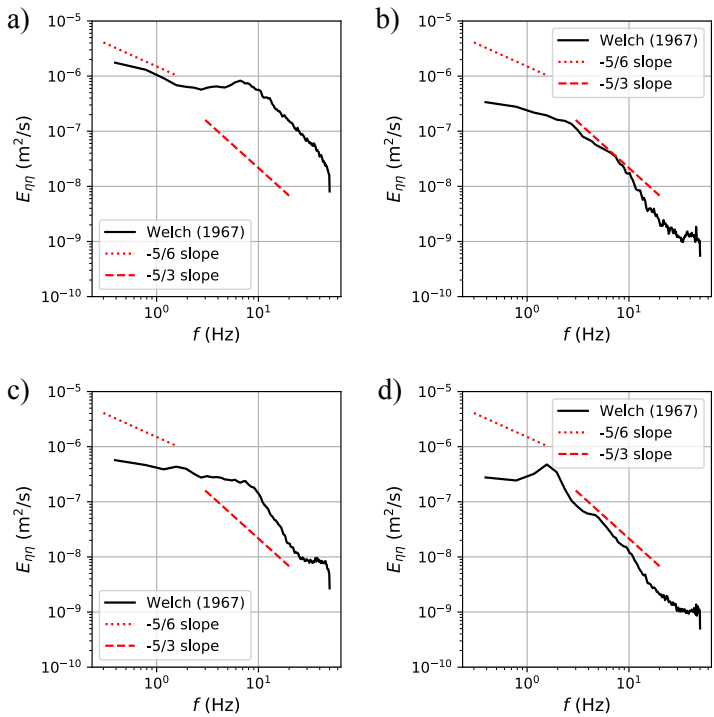

Fig. 10.8 Spectra at the mid non-aerated region (Region II). a) $h_c/s = 1.3$ at $x/L_i = 0.55$, b) $h_c/s = 1.7$ at $x/L_i = 0.27$, c) $h_c/s = 1.9$ at $x/L_i = 0.40$ and d) $h_c/s = 2.1$ at $x/L_i = 0.25$.

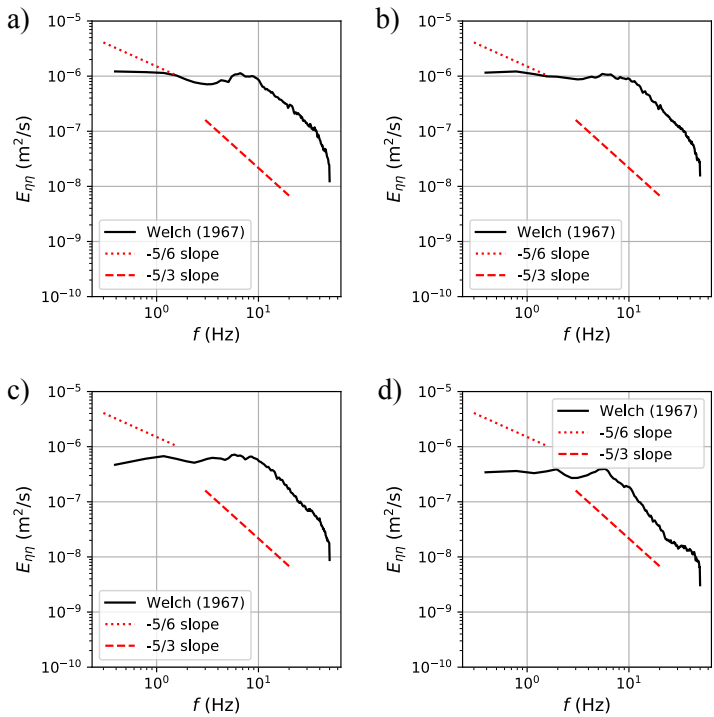

Fig. 10.9 Spectra at the late non-aerated region (Region III). a) $h_c/s = 1.3$ at $x/L_i = 0.73$, b) $h_c/s = 1.7$ at $x/L_i = 0.73$, c) $h_c/s = 1.9$ at $x/L_i = 0.63$ and d) $h_c/s = 2.1$ at $x/L_i = 0.60$.

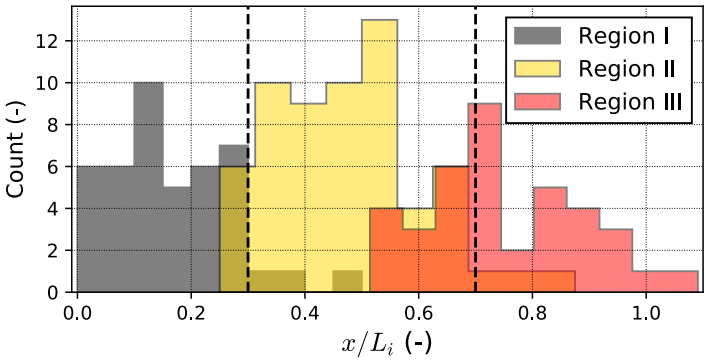

Fig. 10.10 Spectrum type observed in the non-aerated region, according to the three regions classification established. Dashed lines (- -) for the rough boundaries of each region (30 and 70 %).

Table 10.2 Spectrum type observed, according to the region classification (Regions I to II). Data of USS 2.

	Step no.						
	0	0-I	I	I-II	II	II-III	III
h_c/s	*E	N	E	N	E	N	E
0.9	-	I	I	II	II	II	-
1.1	-	I	-	I	II	II	II
1.3	I	I	I	I	II	II	II
1.5	I	I	I	I	I	II	II
1.7	I	I	I	I	II	II	II
1.9	I	I	I	I	I	II	II
2.1	I	I	I	I	I	II	II

*E: edge, N: niche.

Table 10.3 Spectrum type observed, according to the region classification (Regions I to II). Data of USS 3.

	Step no.						
	0	0-I	I	I-II	II	II-III	III
h_c/s	*E	N	E	N	E	N	E
$h_c/s = 0.9$	-	-	-	I	I	II	II
$h_c/s = 1.1$	-	-	I	-	II	II	II
$h_c/s = 1.3$	-	-	-	I	II	II	II
$h_c/s = 1.5$	-	-	I	-	I	II	II
$h_c/s = 1.7$	-	-	I	I	I	II	II
$h_c/s = 1.9$	-	-	I	I	I	II	II
$h_c/s = 2.1$	-	-	I	I	I	I	II

*E: edge, N: niche.

Table 10.4 Spectrum type observed, according to the region classification (Regions II to III). Data of USS 2.

	Step no.						
	III-IV	IV	IV-V	V	V-VI	VI	VI-VII
h_c/s	*N	E	N	E	N	E	N
0.9	-	-	-	-	-	-	-
1.1	III	-	-	-	-	-	-
1.3	II	III	III	III	-	-	-
1.5	II	II	III	III	III	-	-
1.7	II	II	III	III	III	-	-
1.9	II	II	III	III	III	-	-
2.1	II	II	II	II	III	-	-

*N: niche, E: edge.

Table 10.5 Spectrum type observed, according to the region classification (Regions II to III). Data of USS 3.

	Step no.							
	III-IV	IV	IV-V	V	V-VI	VI	VI-VII	VII
h_c/s	*N	E	N	E	N	E	N	E
0.9	II	-	-	-	-	-	-	-
1.1	II	III	III	-	-	-	-	-
1.3	II	III	III	III	III	III	-	-
1.5	II	II	III	III	III	III	III	-
1.7	II	II	II	III	III	III	III	III
1.9	II	II	II	III	III	III	III	III
2.1	II	II	II	II	II	II	III	III

*N: niche, E: edge.

It is also relevant that, given Eqs. 10.2 and 10.3, and that the lower frequencies power slope remains below -1, then the steepness of the perturbations (A/λ) also holds a peak close to the power slopes change. This is in agreement with the results on critical perturbations steepness obtained for the Aviemore spillway in Fig. 9.4. Both findings support the breakup criterion introduced in Eq. 6.7 on the existence of a limiting steepness that causes the final breakup at the self-aeration onset section.

Partial conclusions

Part IV is composed of two chapters. Chapter 9 presents an application where capabilities of the derived equations are exposed at a prototype scale application. Chapter 10 focuses on some empirical evidences gathered at a large-scale stepped spillway at The University of Queensland (UQ).

In Chapter 9, the Aviemore spillway was used as a case study. Capabilities of the proposed analytical formulation were tested against the prototype scale smooth spillway flow observations of Cain (1978) on the Aviemore dam, finding that most unstable wavelengths were close to the Taylor lengthscale. Nonetheless, flow cases with different lengthscales ($\mathscr{L}_{zz}$) would present a different distribution of turbulent normal stresses, thus affecting the most unstable wavelength value.

The characteristic free surface roughness usually observed upstream of the inception point location was explained by the obtained formulation, allowing determination of the water and air

flows contribution to this roughness, not only in magnitude but also in terms of its wavelengths distribution. It was also shown that when self-aeration occurs, there are probably already a wide range of wavelengths standing on unstable configurations, which can explain partly the large range of scales observed downstream the inception point.

Furthermore, it can be observed that perturbations grow up to the intersection of the boundary layer with the free surface, after this point turbulence quantities remain unchanged if self-aeration has not occurred. This must be considered as the limitting case for self-aeration to trigger in a spillway flow. Therefore, determining the boundary layer intersection with the free surface with an accurate method (e.g., Castro-Orgaz and Hager, 2010) can result in a conservative approach in spillway applications, as far as enough free surface distortion takes place which is related to the turbulence perturbing force (and thus the friction factor – or alternatively the skin friction coefficient – and the flow velocity) and the stabilizing effects of surface tension and the magnitude of the gravity projection (g_z, due to the slope). This would yield an additional criterion similar to that of Soo (1956) of Eq. 2.3.

In Chapter 10, an experimental study was conducted in a 45 º slope large-scale stepped spillway. Experimental data was carefully filtered to avoid accounting for the instrumentation error as a turbulence level. Results showed that perturbations grow likewise predicted by the analytical model for the Aviemore

spillway case and that spectra scaling behaviour can be accurately predicted up to a 30 % of the spillway extension. Downstream of the initial 30 % extension, the gravitational scaling tends to flatten and energy is shifted to the surface tension dominated region of the spectra. The $-5/3$ scaling, however, was well predicted by the deduced formulation for all the non-aerated region of the spillway. This may point out in the direction that more complicated hypotheses are necessary for the pressure-gravitational forces approximation for big amplitudes.

Finally, scaling power law slopes observed both in Chapter 9 and 10 seem to highlight that steeper perturbations occur at the inception point location for certain wavelengths, i.e.: most unstable wavelengths exist, which might result in turbulent spots at the inception point location.

Part V

Closure

Chapter 11

Final discussion

11.1 Conclusions

This dissertation started with a quote of Henk Tennekes and John L. Lumley, from one of the first modern books on turbulence. In different words, Tennekes and Lumley (1972) also elucidated that: "*the success of attempts to solve problems in turbulence depends strongly on the inspiration involved in making the crucial assumption*". From where assumptions should come, the second quote opening this thesis was clairvoyant. The Nobel Prize winner Hermann K. Hesse wrote about a man called Siddhartha having a spiritual illumination when looking at the river. Wisdom came from the water. When staring at a fixed point at a spillway, not much can be seen at first. Water runs fast and visual percep-

tion can result insufficient. Try now to follow fast with your head as water flows. Switch from Eulerian to Lagrangian. Set your sight at a fluid particle in the free surface, and follow it as it flows downstream. After a few trials, you will have spotted several perturbations growing and, sometimes, even breaking. They are continuously appearing from “nowhere”. This Lagrangian flow perception inspired fundamental developments of Chapter 7.

The basic assumption of this thesis is that perturbations can exist in the free surface. Later, it is assumed that they break when reaching a limiting steepness, which can be a function of the wavelength. Their geometry is presumed to be the simplest possible three-dimensional form tangent to the free surface, which scales as the perturbation grows. Besides, eddies of a certain wavelength are thought to produce a footprint in the free surface of a similar scale, whereas no interaction between perturbations of different wavelengths is considered. Some geometrical considerations and a balance of forces lead to a dynamic and a kinematic equation, both together describing the growth of the free surface roughness. The used integral approach differs from the classic differential treatment of instabilities, being thus a rather original contribution that allows many practical considerations.

The spectrum shape of the free surface fluctuations has been depicted. It is difficult to foretell how this will help advance knowledge on air-water flows, but it is indisputable how much fluid mechanics advanced since the velocity fluctuations spectra

was well understood. More importantly, it is demonstrated that there is some order on the free surface roughness. How this structure is transferred from the non-aerated region to the aerated region is difficult to foresee. I believe that the most unstable wavelength will impact the waves-type structure while other air-water related lengthscales, such as the Taylor lengthscale, may control how bubbles and droplets take place. On the minimum bubble size, other lengthscales as the Hinze scale could be critical. Shedding light on these relations may allow a universal formulation of the three-dimensional structure or air-water flows, including a complete understanding of scale effects and, finally, allowing formulation of accurate numerical models.

Altogether, a fluid mechanics explanation of self-aeration has been presented. Furthermore, a new mathematical framework for the understanding and prediction of the inception point under arbitrary flow conditions has been established. On the validity of the formulated equations and the hypotheses underneath, a clear insight can be gained from the free surface fluctuations spectrum. Two power law scaling coefficients were analytically obtained, corresponding to the inertial and surface tension dominated ranges (large and small wavelengths correspondingly). For the surface tension dominated scaling, its validity holds up to the inception point location. However, the inertial range flattens at around 30 % of the distance to the inception point, collapsing to a null slope; whereas some energy is transferred to the smaller scales. It is still early to identify which hypotheses need

to be readdressed, despite the pressure-gravity relation might be the most simplistic one at large amplitudes, and the dependence of the critical steepness (S_{lim}) on the wavelength should be assessed from hydraulic engineering applications, and not coastal waves. Also, the shape of the perturbations may differ from the sinusoidal shape assumed, specially at large steepness values.

11.2 Future research

Based on the presented findings, need for new research arises as fundamental.

One relevant point to address is to fully characterize the free surface perturbations geometry in hydraulic engineering applications, including both the crest and the submerged body. This will permit the adjustment of the coefficients that, in this thesis, were analytically obtained for a simplistic geometry, and the accurate estimation of the forces acting over the control volume. Further considerations may be necessary for the most restrictive hypotheses[1]. A full validation for different types of flow cases should also be considered essential.

The breakup criterion may require formulation based on observations in hydraulic engineering applications, which could

[1] Pressure distribution, eddy-perturbation interaction, no interaction between wavelengths and the invariability of the wavelengths with time, which results in no transverse dispersion.

lead to criteria different from those of coastal applications. While normal velocity fluctuations are the main turbulent term responsible for the perturbations' growth, shearing could be assisting on an earlier breakup than that determined solely based on the perturbation's slope.

Addressing satisfactorily these points may lead to a robust model, ultimately capable of predicting self-aeration inception for complex environmental problems. Given the potentially large range of application, the implementation on a Computational Fluid Dynamics toolbox can largely help the community to deal with the self-aeration onset determination.

On how to predict the complete air-water flow features evolution downstream of the inception point, I believe that knowledge is still far from reaching a universal model, but good understanding of the flow structure may be the first step towards it.

11.3 Closing remarks

All in all, this dissertation was an attempt to put self-aeration into the wider topic of fluid mechanics. It is my sincere wish that with the developed theoretical framework, future researchers will find a solid bedrock to support new findings. We can now state that self-aeration can be understood as a multiphase flow instability.

It is important to highlight that, strictly speaking, it is not a Kelvin-Helmholtz instability, which arises as a discontinuity of velocities across the interface between two fluids. It is not a viscous Kelvin-Helmholtz instability, similar to the previous one but accounting for the damping/disturbing effect of viscosity. It is not a Rayleigh-Taylor instability, which would be related to the difference in the density of the fluids. It is neither a Plateau-Rayleigh instability, as in our case the turbulence effect is the driving force of the perturbations' growth and, consequently, $\mathscr{L}_{zz}$ affecting the dominant lengthscale of the perturbations. May we talk about a mixture of all of them? Or, differently, shall we start talking about a new type of turbulent multiphase flow instability?

References

Abbena, E., Salamon, S., and Gray, A. (2006). *Modern differential geometry of curves and surfaces with Mathematica*. CRC press.

Aidun, C. K. and Clausen, J. R. (2010). Lattice-boltzmann method for complex flows. *Annual Review of Fluid Mechanics*, 42:439–472.

Amador, A., Sánchez-Juny, M., and Dolz, J. (2006). Characterization of the nonaerated flow region in a stepped spillway by PIV. *Journal of Fluids Engineering*, 128(6):1266–1273.

Amador, A., Sánchez-Juny, M., and Dolz, J. (2009). Developing flow region and pressure fluctuations on steeply sloping stepped spillways. *Journal of Hydraulic Engineering*, 135(12):1092–1100.

Anwar, H. O. (1994). Discussion of "Self-Aerated Flows on Chutes and Spillways" by H. Chanson (1993). *Journal of Hydraulic Engineering*, 120(6):778–779.

Auel, C., Albayrak, I., and Boes, R. M. (2014). Turbulence characteristics in supercritical open channel flows: effects of froude number and aspect ratio. *Journal of Hydraulic Engineering*, 140(4):04014004.

Balachandar, S. and Eaton, J. K. (2010). Turbulent dispersed multiphase flow. *Annual Review of Fluid Mechanics*, 42:111–133.

Barthelemy, X., Banner, M. L., Peirson, W. L., Fedele, F., Allis, M., and Dias, F. (2018). On a unified breaking onset threshold for gravity waves in deep and intermediate depth water. *Journal of Fluid Mechanics*, 841:463–488.

Bauer, W. J. (1951). *The development of the turbulent boundary layer on steep slopes*. PhD thesis, University of Iowa.

Bauer, W. J. (1954). The development of the turbulent boundary layer on steep slopes. *Transactions of the American Society of Civil Engineers*, 119(1):1212–1233.

Bayon, A., Valero, D., García-Bartual, R., Vallés-Morán, F. J., and López-Jiménez, P. A. (2016). Performance assessment of OpenFOAM and FLOW-3D in the numerical modeling of a low Reynolds number hydraulic jump. *Environmental Modelling & Software*, 80:322–335.

Bertola, N., Wang, H., and Chanson, H. (2018). A physical study of air–water flow in planar plunging water jet with large inflow distance. *International Journal of Multiphase Flow*, 100:155–171.

Blocken, B. and Gualtieri, C. (2012). Ten iterative steps for model development and evaluation applied to computational fluid dynamics for environmental fluid mechanics. *Environmental Modelling & Software*, 33:1–22.

Boes, R. M. (2000). *Zwiephasenströmung und Energieumsetzung auf Grosskaskaden*. PhD thesis, ETH Zurich.

Boes, R. M. and Hager, W. H. (2003). Two-phase flow characteristics of stepped spillways. *Journal of Hydraulic Engineering*, 129(9):661–670.

Bollaert, E. and Schleiss, A. (2003). Scour of rock due to the impact of plunging high velocity jets Part I: A state-of-the-art review. *Journal of Hydraulic Research*, 41(5):451–464.

Bombardelli, F. A. (2012). Computational multi-phase fluid dynamics to address flows past hydraulic structures. In *4th IAHR International Symposium on Hydraulic Structures*, pages 9–11.

Bombardelli, F. A., Meireles, I., and Matos, J. (2011). Laboratory measurements and multi-block numerical simulations of the mean flow and turbulence in the non-aerated skimming flow region of steep stepped spillways. *Environmental Fluid Mechanics*, 11(3):263–288.

Bormann, K. (1968). *Der Abfluss in Schussrinnen unter Berücksichtigung der Luftaufnahme*. PhD thesis, Bericht 13. München, Germany: Versuchsanstalt für Wasserbau, Oskar von Miller Institut, Technische Hochschule.

Bradshaw, P., Launder, B. E., and Lumley, J. L. (1996). Collaborative testing of turbulence models. *Journal of Fluids Engineering*, 118(2):243–247.

Brand, A., Noss, C., Dinkel, C., and Holzner, M. (2016). High-resolution measurements of turbulent flow close to the sediment–water interface using a bistatic acoustic profiler. *Journal of Atmospheric and Oceanic Technology*, 33(4):769–788.

Brocchini, M. and Peregrine, D. H. (2001). The dynamics of strong turbulence at free surfaces. Part 1. Description. *Journal of Fluid Mechanics*, 449:225–254.

Bung, D. B. (2009). *Zur selbstbelüfteten Gerinneströmung auf Kaskaden mit gemäßigter Neigung*. PhD thesis, Bergische Universität Wuppertal, Wuppertal, Germany.

Bung, D. B. (2011). Developing flow in skimming flow regime on embankment stepped spillways. *Journal of Hydraulic Research*, 49(5):639–648.

Bung, D. B. (2013). Non-intrusive detection of air-water surface roughness in self-aerated chute flows. *Journal of Hydraulic Research*, 51(3):322–329.

Bung, D. B., Hildebrandt, A., Oertel, M., Schlenkhoff, A., and Schlurmann, T. (2009). Bore propagation over a submerged horizontal plate by physical and numerical simulation. In *Coastal Engineering, 2008*, pages 3542–3553. World Scientific.

Bung, D. B. and Valero, D. (2015). Image processing for Bubble Image Velocimetry in self-aerated flows. In *e-proceedings of the 36th IAHR World Congress, The Hague, The Netherlands*, pages 6594–6601.

Bung, D. B. and Valero, D. (2016a). Application of the Optical Flow Method to Velocity Determination in Hydraulic Structure Models. In *Hydraulic Structures and Water System Management. 6th IAHR International Symposium on Hydraulic Structures, Portland, OR, USA*.

Bung, D. B. and Valero, D. (2016b). Optical Flow estimation in aerated flows. *Journal of Hydraulic Research*, 54(5):575–580.

Cain, P. (1978). *Measurements within Self-Aerated Flow on a Large Spillway.* PhD thesis, University of Canterbury, Christchurch, New Zealand.

Cain, P. and Wood, I. R. (1981). Measurements of self-aerated flow on a spillway. *Journal of the Hydraulics Division*, 107(11):1425–1444.

Caisley, M. E., Bombardelli, F. A., and Garcia, M. H. (1999). Hydraulic model study of a canoe chute for low-head dams in illinois (hes 63). Technical report.

Cameron, S. M., Nikora, V. I., and Stewart, M. T. (2017). Very-large-scale motions in rough-bed open-channel flow. *Journal of Fluid Mechanics*, 814:416–429.

Cardoso, A. H., Graf, W. H., and Gust, G. (1989). Uniform flow in a smooth open channel. *Journal of Hydraulic Research*, 27(5):603–616.

Carrica, P. M., Drew, D., Bonetto, F., and Lahey Jr, R. T. (1999). A polydisperse model for bubbly two-phase flow around a surface ship. *International Journal of Multiphase Flow*, 25(2):257–305.

Carvalho, R. F., Lemos, C. M., and Ramos, C. M. (2008). Numerical computation of the flow in hydraulic jump stilling basins. *Journal of Hydraulic Research*, 46(6):739–752.

Castro, A. M. and Carrica, P. M. (2013). Bubble size distribution prediction for large-scale ship flows: Model evaluation and numerical issues. *International Journal of Multiphase Flow*, 57:131–150.

Castro-Orgaz, O. (2010). Velocity profile and flow resistance models for developing chute flow. *Journal of Hydraulic Engineering*, 136(7):447–452.

Castro-Orgaz, O. and Hager, W. H. (2010). Drawdown curve and turbulent boundary layer development for chute flow. *Journal of Hydraulic Research*, 48(5):591–602.

Castro-Orgaz, O. and Hager, W. H. (2017). *Non-Hydrostatic Free Surface Flows*. Springer, Advances in Geophysical and Environmental Mechanics and Mathematics.

Celik, I. B., Ghia, U., Roache, P. J., Freitas, C. J., Coleman, H., and Raad, P. E. (2008). Procedure for estimation and reporting of uncertainty due to discretization in CFD applications. *Journal of Fluids Engineering*, 130(7).

Chamani, M. R. and Rajaratnam, N. (1999). Characteristics of skimming flow over stepped spillways. *Journal of Hydraulic Engineering*, 125(4):361–368.

Chanson, H. (1988). *A study of air entrainment and aeration devices on a spillway model*. PhD thesis, University of Canterbury, Christchurch, New Zealand.

Chanson, H. (1992). Air entrainment on chute and tunnel spillways. In *11th Australasian Fluid Mechanics Conference*, volume 1, pages 83–86.

Chanson, H. (1993). Self-aerated flows on chutes and spillways. *Journal of Hydraulic Engineering*, 119(2):220–243.

Chanson, H. (1994a). Drag reduction in open channel flow by aeration and suspended load. *Journal of Hydraulic Research*, 32(1):87–101.

Chanson, H. (1994b). Hydraulics of skimming flows over stepped channels and spillways. *Journal of Hydraulic Research*, 32(3):445–460.

Chanson, H. (1996). *Air Bubble Entrainment in Free-surface Turbulent Shear Flows.* Academic Press.

Chanson, H. (1997). Air bubble entrainment in open channels: Flow structure and bubble size distributions. *International Journal of Multiphase Flow*, 23(1):193 – 203.

Chanson, H. (2002). *Hydraulics of stepped chutes and spillways*. CRC Press.

Chanson, H. (2004). *Hydraulics of Open Channel Flow: An Introduction*. Butterworth-Heinemann, 2nd edition.

Chanson, H. (2009). Turbulent air–water flows in hydraulic structures: dynamic similarity and scale effects. *Environmental Fluid Mechanics*, 9(2):125–142.

Chanson, H. (2010). Convective transport of air bubbles in strong hydraulic jumps. *International Journal of Multiphase Flow*, 36(10):798–814.

Chanson, H. (2013a). Advective diffusion of air bubbles in turbulent water flows. In Gualtieri, C. and Mihailovic, D. T., editors, *Fluid Mechanics of Environmental Interfaces*, chapter 7. Taylor & Francis, Leiden, The Netherlands.

Chanson, H. (2013b). Hydraulics of aerated flows: qui pro quo? *Journal of Hydraulic Research*, 51(3):223–243.

Chanson, H. (2015). *Energy Dissipation in Hydraulic Structures*. CRC Press, Taylor & Francis Group.

Chanson, H. (2016). Phase-detection measurements in free-surface turbulent shear flows. *Journal of Geophysics and Engineering*, 13(2):S74.

Chanson, H. and Brattberg, T. (2000). Experimental study of the air–water shear flow in a hydraulic jump. *International Journal of Multiphase Flow*, 26(4):583–607.

Chanson, H., Bung, D. B., and Matos, J. (2015). Stepped spillways and cascades. In Chanson, H., editor, *Energy Dissipation in Hydraulic Structures*, pages 45–64. IAHR Monograph, CRC Press, Taylor & Francis Group.

Chanson, H. and Chachereau, Y. (2013). Scale effects affecting two-phase flow properties in hydraulic jump with small inflow

froude number. *Experimental Thermal and Fluid Science*, 45:234–242.

Chanson, H. and Gualtieri, C. (2008). Similitude and scale effects of air entrainment in hydraulic jumps. *Journal of Hydraulic Research*, 46(1):35–44.

Chanson, H. and Toombes, L. (2002). Air–water flows down stepped chutes: turbulence and flow structure observations. *International Journal of Multiphase Flow*, 28(11):1737–1761.

Chanson, H., Yasuda, Y., and Ohtsu, I. (2002). Flow resistance in skimming flows in stepped spillways and its modelling. *Canadian Journal of Civil Engineering*, 29(6):809–819.

Chen, S. and Doolen, G. D. (1998). Lattice boltzmann method for fluid flows. *Annual Review of Fluid Mechanics*, 30(1):329–364.

Christensen, E. D. and Deigaard, R. (2001). Large eddy simulation of breaking waves. *Coastal Engineering*, 42(1):53–86.

Crookston, B. M., Anderson, R. M., and Tullis, B. P. (2018). Free-flow discharge estimation method for piano key weir geometries. *Journal of Hydro-environment Research*, 19:160–167.

Crowe, C. T., Schwarzkopf, J. D., Sommerfeld, M., and Tsuji, Y. (2011). *Multiphase Flows with Droplets and Particles*. CRC press, 2nd edition.

Cummings, P. D. and Chanson, H. (1997). Air entrainment in the developing flow region of plunging jets—Part 2: Experimental. *Journal of Fluids Engineering*, 119(3):603–608.

Cummings, P. D. and Chanson, H. (1999). An experimental study of individual air bubble entrainment at a planar plunging jet. *Chemical Engineering Research and Design*, 77(2):159–164.

Dabiri, D. (2003). On the interaction of a vertical shear layer with a free surface. *Journal of Fluid Mechanics*, 480:217.

Davidson, P. A. (2015). *Turbulence: An Introduction for Scientists and Engineers*. Oxford University Press, 2nd edition.

De Padova, D., Mossa, M., and Sibilla, S. (2017). SPH modelling of hydraulic jump oscillations at an abrupt drop. *Water*, 9(10):790.

De Padova, D., Mossa, M., Sibilla, S., and Torti, E. (2013). 3D SPH modelling of hydraulic jump in a very large channel. *Journal of Hydraulic Research*, 51(2):158–173.

Deane, G. B. and Stokes, M. D. (2002). Scale dependence of bubble creation mechanisms in breaking waves. *Nature*, 418(6900):839.

Deike, L., Popinet, S., and Melville, W. K. (2015). Capillary effects on wave breaking. *Journal of Fluid Mechanics*, 769:541–569.

Dey, S. (2014). *Fluvial Hydrodynamics*. Springer.

Dey, S. and Raikar, R. V. (2007). Characteristics of loose rough boundary streams at near-threshold. *Journal of Hydraulic Engineering*, 133(3):288–304.

Duncan, J. H. (1981). An experimental investigation of breaking waves produced by a towed hydrofoil. *Proceedings of the Royal Society of London A*, 377(1770):331–348.

Ehrenberger, R. (1926). *Wasserbewegung in steilen Rinnen (Schußrinnen) mit besonderer Berücksichtigung der Selbstbelüftung*. Hydrographisches Zentralbüro im Bundesministerium für Land- u. Forstwirtschaft.

Erpicum, S., Lodomez, M., Savatier, J., Archambeau, P., Dewals, B., and Pirotton, M. (2016). Physical modeling of an aerating stepped spillway. In *Hydraulic Structures and Water System Management. 6th IAHR International Symposium on Hydraulic Structures, Portland, OR, USA*, pages 608–617.

Ervine, D. A. (1998). Air entrainment in hydraulic structures: a review. *Proceedings of the Institution of Civil Engineers - Water Maritime and Energy*, 130(3):142–153.

Ervine, D. A. and Falvey, H. T. (1987). Behaviour of turbulent water jets in the atmosphere and in plunge pools. *Proceedings of the Institution of Civil Engineers*, 83(1):295–314.

Ervine, D. A., McKeogh, E., and Elsawy, E. M. (1980). Effect of turbulence intensity on the rate of air entrainment by plunging water jets. *Proceedings of the Institution of Civil Engineers*, 69(2):425–445.

Falvey, H. T. (1980). *Air-Water Flow in Hydraulic Structures*. Water and Power Resources Service, Engineering Monograph No. 41.

Falvey, H. T. (1990). *Cavitation in Chutes and Spillways*. Water and Power Resources Service, Engineering Monograph No. 42.

Felder, S. and Chanson, H. (2009). Turbulence, dynamic similarity and scale effects in high-velocity free-surface flows above a stepped chute. *Experiments in Fluids*, 47(1):1–18.

Felder, S. and Chanson, H. (2011). Air–water flow properties in step cavity down a stepped chute. *International Journal of Multiphase Flow*, 37(7):732–745.

Felder, S. and Chanson, H. (2014). Air–water flows and free-surface profiles on a non-uniform stepped chute. *Journal of Hydraulic Research*, 52(2):253–263.

Felder, S. and Chanson, H. (2016). Air–water flow characteristics in high-velocity free-surface flows with 50% void fraction. *International Journal of Multiphase Flow*, 85:186–195.

Felder, S. and Chanson, H. (2017). Scale effects in microscopic air-water flow properties in high-velocity free-surface flows. *Experimental Thermal and Fluid Science*, 83:19–36.

Flores, O., Riley, J. J., and Horner-Devine, A. R. (2017). On the dynamics of turbulence near a free surface. *Journal of Fluid Mechanics*, 821:248–265.

Funada, T. and Joseph, D. D. (2001). Viscous potential flow analysis of Kelvin–Helmholtz instability in a channel. *Journal of Fluid Mechanics*, 445:263–283.

Fuster, D., Bagué, A., Boeck, T., Le Moyne, L., Leboissetier, A., Popinet, S., Ray, P., Scardovelli, R., and Zaleski, S. (2009). Simulation of primary atomization with an octree adaptive mesh refinement and VOF method. *International Journal of Multiphase Flow*, 35(6):550–565.

Gibson, M. M. and Rodi, W. (1989). Simulation of free surface effects on turbulence with a reynolds stress model. *Journal of Hydraulic Research*, 27(2):233–244.

Gingold, R. A. and Monaghan, J. J. (1977). Smoothed particle hydrodynamics: theory and application to non-spherical stars. *Monthly Notices of the Royal Astronomical Society*, 181(3):375–389.

González, R. C., Woods, R. E., and Eddins, S. L. (2004). *Digital Imaging Processing using MATLAB*. Prentice Hall.

Goring, D. G. and Nikora, V. I. (2002). Despiking acoustic doppler velocimeter data. *Journal of Hydraulic Engineering*, 128(1):117–126.

Gulliver, J. S. and Halverson, M. J. (1987). Measurements of large streamwise vortices in an open-channel flow. *Water Resources Research*, 23(1):115–123.

Gulliver, J. S., Thene, J. R., and Rindels, A. J. (1990). Indexing gas transfer in self-aerated flows. *Journal of Environmental Engineering*, 116(3):503–523.

Guo, X. and Shen, L. (2010). Interaction of a deformable free surface with statistically steady homogeneous turbulence. *Journal of Fluid Mechanics*, 658:33–62.

Hager, W. H. (1992). *Energy Dissipators and Hydraulic Jump*. Springer Science & Business Media, Water Science and Technology Library.

Hager, W. H. (2016). Rudolf ehrenberger, hydrauliker und wasserbauer. *Österreichische Wasser-und Abfallwirtschaft*, 68(3-4):154–165.

Hager, W. H. and Boes, R. M. (2014). Hydraulic structures: a positive outlook into the future. *Journal of Hydraulic Research*, 52(3):299–310.

Halbronn, G. (1952). Étude de la mise en régime des écoulements sur les ouvrages ò forte pente. *La Houille Blanche*, 5:702–722.

Hampel, F. R. (1974). The influence curve and its role in robust estimation. *Journal of the American Statistical Association*, 69(346):383–393.

Handler, R. A., Swean, T. F., Leighton, R. I., and Swearingen, J. D. (1993). Length scales and the energy balance for turbulence near a free surface. *AIAA Journal*, 31(11):1998–2007.

Heller, V. (2011). Scale effects in physical hydraulic engineering models. *Journal of Hydraulic Research*, 49(3):293–306.

Heller, V., Hager, W. H., and Minor, H.-E. (2005). Ski jump hydraulics. *Journal of Hydraulic Engineering*, 131(5):347–355.

Helmholtz, H. v. (1868). Über diskontinuierliche Flüssigkeitsbewegungen. *Berliner Montatsberichte*.

Hickox, G. H. (1945). Air entrainment on spillway faces. *Civil Engineering*, 15(12):562–563.

Hino, M. (1961). On the mechanism of self-aerated flow on steep slope channels. applications of the statistical theory of turbulence. In *Proceedings 9th IAHR Congress, Dubrovnick, Yugoslavia*, pages 123–132.

Hinze, J. O. (1955). Fundamentals of the hydrodynamic mechanism of splitting in dispersion processes. *AIChE Journal*, 1(3):289–295.

Hirsch, C. (2007). *Numerical computation of internal & external flows: The fundamentals of computational fluid dynamics*. Butterworth-Heinemann.

Hirt, C. W. (2003). Modeling turbulent entrainment of air at a free surface. Technical Report 61-R, FlowScience, Inc.

Hirt, C. W. and Nichols, B. D. (1981). Volume of fluid (vof) method for the dynamics of free boundaries. *Journal of Computational Physics*, 39(1):201–225.

Ho, D. K. H., Boyes, K. M., and Donohoo, S. M. (2001). Investigation of spillway behavior under increased maximum flood by computational fluid dynamics technique. In *14th Australasian Fluid Mechanics Conference, Adelaide University, Adelaide, Australia*.

Hoyas, S. and Jiménez, J. (2006). Scaling of the velocity fluctuations in turbulent channels up to re τ= 2003. *Physics of fluids*, 18(1):011702.

Hristov, T. S., Miller, S. D., and Friehe, C. A. (2003). Dynamical coupling of wind and ocean waves through wave-induced air flow. *Nature*, 422(6927):55–58.

Hunt, J. C. R. and Graham, J. M. R. (1978). Free-stream turbulence near plane boundaries. *Journal of Fluid Mechanics*, 84(02):209–235.

Hunt, S. L. and Kadavy, K. C. (2013). Inception point for embankment dam stepped spillways. *Journal of Hydraulic Engineering*, 139(1):60–64.

Husain, S. M., Muhammed, J. R., Karunarathna, H. U., and Reeve, D. E. (2014). Investigation of pressure variations over stepped spillways using smooth particle hydrodynamics. *Advances in Water Resources*, 66:52–69.

Idelsohn, S. R., Oñate, E., and Pin, F. D. (2004). The particle finite element method: a powerful tool to solve incompressible flows with free-surfaces and breaking waves. *International Journal for Numerical Methods in Engineering*, 61(7):964–989.

Ishii, M. and Hibiki, T. (2010). *Thermo-Fluid Dynamics of Two-Phase Flow*. Springer Science & Business Media.

Janssen, P. (2004). *The interaction of ocean waves and wind*. Cambridge University Press.

Jiménez, J. (2018). Coherent structures in wall-bounded turbulence. *Journal of Fluid Mechanics*, 842.

Johnson, E. D. and Cowen, E. A. (2016). Remote monitoring of volumetric discharge employing bathymetry determined from surface turbulence metrics. *Water Resources Research*, 52(3):2178–2193.

Johnson, E. D. and Cowen, E. A. (2017). Estimating bed shear stress from remotely measured surface turbulent dissipation fields in open channel flows. *Water Resources Research*, 53(3):1982–1996.

Keller, R. J. (1972). *Field measurement of self-aerated high speed open channel flow*. PhD thesis, University of Canterbury. Civil Engineering.

Keller, R. J. and Rastogi, A. K. (1975). Prediction of flow development on spillways. *Journal of the Hydraulics Division*, 101(9):1171–1184.

Keller, R. J. and Rastogi, A. K. (1977). Design chart for predicting critical point on spillways. *Journal of the Hydraulics Division*, 103(12):1417–1429.

Kelvin, L. (1871). Hydrokinetic solutions and observations. In *Philosophical Magazine*, volume 42, pages 362–377.

Kiger, K. T. and Duncan, J. H. (2012). Air-entrainment mechanisms in plunging jets and breaking waves. *Annual Review of Fluid Mechanics*, 44:563–596.

Killen, J. M. (1968). *The surface characteristics of self-aerated flow in steep channels.* PhD thesis, University of Minnesota, Minneapolis, USA.

Kironoto, B. A. and Graf, W. H. (1994). Turbulence characteristics in rough uniform open-channel flow. *Proceedings of the Institution of Civil Engineers. Water, Maritime and Energy*, 106(4):333–344.

Kironoto, B. A. and Graf, W. H. (1995). Turbulence characteristics in rough non-uniform open-channel flow. *Proceedings of the Institution of Civil Engineers - Water, Maritime and Energy*, 112(4):336–348.

Klebanoff, P. S. (1955). Characteristics of turbulence in boundary layer with zero pressure gradient. Technical report.

Kline, S. J., Reynolds, W. C., Schraub, F. A., and Runstadler, P. W. (1967). The structure of turbulent boundary layers. *Journal of Fluid Mechanics*, 30(4):741–773.

Kobus, H. (1984). Local air entrainment and detrainment. In *Symposium on Scale Effects in Modelling Hydraulic Structures*.

Koca, K., Noss, C., Anlanger, C., Brand, A., and Lorke, A. (2017). Performance of the vectrino profiler at the sediment–water interface. *Journal of Hydraulic Research*, 55(4):573–581.

Kramer, K., Hager, W. H., and Minor, H.-E. (2006). Development of air concentration on chute spillways. *Journal of Hydraulic Engineering*, 132(9):908–915.

Kramer, M. and Chanson, H. (2018). Free-surface instabilities in high-velocity air-water flows down stepped chutes. In *7th International Symposium on Hydraulic Structures*.

Labourasse, E., Lacanette, D., Toutant, A., Lubin, P., Vincent, S., Lebaigue, O., Caltagirone, J.-P., and Sagaut, P. (2007). Towards large eddy simulation of isothermal two-phase flows: Governing equations and a priori tests. *International Journal of Multiphase Flow*, 33(1):1–39.

Landau, L. D. and Lifshitz, E. M. (1987). *Fluid Mechanics*, volume 6 of *Course of Theoretical Physics*. Elsevier, Butterworth Heinemann, 2nd edition.

Lane, E. W. (1939). Entrainment of air in swiftly flowing water. *Civil Engineering*, 9(2):89–96.

Launder, B. E. and Spalding, D. B. (1974). The numerical computation of turbulent flows. *Computer Methods in Applied Mechanics and Engineering*, 3(2):269–289.

Leys, C., Ley, C., Klein, O., Bernard, P., and Licata, L. (2013). Detecting outliers: Do not use standard deviation around the mean, use absolute deviation around the median. *Journal of Experimental Social Psychology*, 49(4):764–766.

Liu, M., Rajaratnam, N., and Zhu, D. Z. (2004). Turbulence structure of hydraulic jumps of low froude numbers. *Journal of Hydraulic Engineering*, 130(6):511–520.

Lock, R. C. (1951). The velocity distribution in the laminar boundary layer between parallel streams. *The Quarterly Journal of Mechanics and Applied Mathematics*, 4(1):42–63.

Long, D., Rajaratnam, N., Steffler, P. M., and Smy, P. R. (1991). Structure of flow in hydraulic jumps. *Journal of Hydraulic Research*, 29(2):207–218.

Longo, S. and Losada, M. A. (2012). Turbulent structure of air flow over wind-induced gravity waves. *Experiments in Fluids*, 53(2):369–390.

López, D., Marivela, R., and Garrote, L. (2010). Smoothed particle hydrodynamics model applied to hydraulic structures: a hydraulic jump test case. *Journal of Hydraulic Research*, 48(S1):142–158.

Lu, J., Fernández, A., and Tryggvason, G. (2005). The effect of bubbles on the wall drag in a turbulent channel flow. *Physics of Fluids*, 17(9):095102.

Lubin, P. and Chanson, H. (2017). Are breaking waves, bores, surges and jumps the same flow? *Environmental Fluid Mechanics*, 17(1):47–77.

Lubin, P., Chanson, H., and Glockner, S. (2010). Large eddy simulation of turbulence generated by a weak breaking tidal bore. *Environmental Fluid Mechanics*, 10(5):587–602.

Lubin, P. and Glockner, S. (2015). Numerical simulations of three-dimensional plunging breaking waves: generation and evolution of aerated vortex filaments. *Journal of Fluid Mechanics*, 767:364–393.

Lubin, P., Vincent, S., Abadie, S., and Caltagirone, J.-P. (2006). Three-dimensional large eddy simulation of air entrainment under plunging breaking waves. *Coastal Engineering*, 53(8):631–655.

Ma, J., Oberai, A. A., Drew, D. A., Lahey Jr, R. T., and Moraga, F. J. (2010). A quantitative sub-grid air entrainment model for bubbly flows–plunging jets. *Computers & Fluids*, 39(1):77–86.

Ma, J., Oberai, A. A., Lahey, R. T., and Drew, D. A. (2011). Modeling air entrainment and transport in a hydraulic jump using two-fluid RANS and DES turbulence models. *Heat and Mass Transfer*, 47(8):911.

MacVicar, B. J., Dilling, S., Lacey, R. W. J., and Hipel, K. (2014). A quality analysis of the Vectrino II instrument using a new open-source MATLAB toolbox and 2D ARMA models to detect and replace spikes. In *River Flow*, pages 1951–1959.

Matos, J. (2000). Hydraulic design of stepped spillways over RCC dams. In *International Workshop on Hydraulics of Stepped Spillways*, pages 187–194. Balkema.

Meireles, I., Bombardelli, F. A., and Matos, J. (2014). Air entrainment onset in skimming flows on steep stepped spillways: an analysis. *Journal of Hydraulic Research*, 52(3):375–385.

Meireles, I. and Matos, J. (2009). Skimming flow in the nonaerated region of stepped spillways over embankment dams. *Journal of Hydraulic Engineering*, 135(8):685–689.

Meireles, I., Renna, F., Matos, J., and Bombardelli, F. (2012). Skimming, nonaerated flow on stepped spillways over roller compacted concrete dams. *Journal of Hydraulic Engineering*, 138(10):870–877.

Melville, W. K. (1982). The instability and breaking of deep-water waves. *Journal of Fluid Mechanics*, 115:165–185.

Menter, F. R. (1994). Two-equation eddy-viscosity turbulence models for engineering applications. *AIAA journal*, 32(8):1598–1605.

Miche, M. (1944). Mouvements ondulatoires de la mer en profondeur constante ou décroissante. *Annales de Ponts et Chaussées, 1944, pp (1) 26-78,(2) 270-292,(3) 369-406*.

Michell, J. H. (1893). The highest waves in water. volume 36, pages 430–437. Taylor & Francis.

Michels, V. and Lovely, M. (1953). Some prototype observations of air entrained flow. In *Proceedings: Minnesota International Hydraulic Convention*, pages 403–414. ASCE.

Mier-Torrecilla, M. d. (2010). *Numerical simulation of multi-fluid flows with the Particle Finite Element Method*. PhD thesis, Universitat Politècnica de Catalunya.

Mier-Torrecilla, M. d., Idelsohn, S. R., and Oñate, E. (2011). Advances in the simulation of multi-fluid flows with the particle fi-

nite element method. application to bubble dynamics. *International Journal for Numerical Methods in Fluids*, 67(11):1516–1539.

Miles, J. W. (1957). On the generation of surface waves by shear flows. *Journal of Fluid Mechanics*, 3(02):185–204.

Miles, J. W. (1959). On the generation of surface waves by shear flows part 3. Kelvin-Helmholtz instability. *Journal of Fluid Mechanics*, 6(04):583–598.

Moin, P. and Mahesh, K. (1998). Direct numerical simulation: A tool in turbulence research. *Annual Review of Fluid Mechanics*, 30(1):539–578.

Monaghan, J. J. (1994). Simulating free surface flows with sph. *Journal of Computational Physics*, 110(2):399–406.

Montano, L., Li, R., and Felder, S. (2018). Continuous measurements of time-varying free-surface profiles in aerated hydraulic jumps with a LIDAR. *Experimental Thermal and Fluid Science*, 93:379–397.

Moraga, F. J., Carrica, P. M., Drew, D. A., and Lahey Jr, R. T. (2008). A sub-grid air entrainment model for breaking bow waves and naval surface ships. *Computers & Fluids*, 37(3):281–298.

Mortazavi, M., Le Chenadec, V., Moin, P., and Mani, A. (2016). Direct numerical simulation of a turbulent hydraulic jump: turbulence statistics and air entrainment. *Journal of Fluid Mechanics*, 797:60–94.

Mouaze, D., Murzyn, F., and Chaplin, J. R. (2005). Free surface length scale estimation in hydraulic jumps. *Journal of Fluids Engineering*, 127(6):1191–1193.

Murzyn, F. and Chanson, H. (2008). Experimental assessment of scale effects affecting two-phase flow properties in hydraulic jumps. *Experiments in Fluids*, 45(3):513–521.

Nezu, I. (1977). *Turbulent Structure in Open-Channel Flows*. PhD thesis, Kyoto University.

Nezu, I. (2005). Open-channel flow turbulence and its research prospect in the 21st century. *Journal of Hydraulic Engineering*, 131(4):229–246.

Nezu, I. and Rodi, W. (1986). Open-channel flow measurements with a laser doppler anemometer. *Journal of Hydraulic Engineering*, 112(5):335–355.

Nichols, A., Tait, S. J., Horoshenkov, K. V., and Shepherd, S. J. (2016). A model of the free surface dynamics of shallow turbulent flows. *Journal of Hydraulic Research*, 54(5):516–526.

Novak, P., Moffat, A. I. B., Nalluri, C., and Narayanan, R. (2007). *Hydraulic Structures*. CRC Press, 4th edition.

Ohtsu, I. and Yasuda, Y. (1991). Hydraulic jump in sloping channels. *Journal of Hydraulic Engineering*, 117(7):905–921.

Ohtsu, I., Yasuda, Y., and Takahashi, M. (2004). Flow characteristics of skimming flows in stepped channels. *Journal of Hydraulic Engineering*, 130(9):860–869.

Oñate, E., Celigueta, M. A., Idelsohn, S. R., Salazar, F., and Suárez, B. (2011). Possibilities of the particle finite element method for fluid–soil–structure interaction problems. *Computational Mechanics*, 48(3):307.

Oñate, E., Idelsohn, S. R., Del Pin, F., and Aubry, R. (2004). The particle finite element method—an overview. *International Journal of Computational Methods*, 1(02):267–307.

Perlin, M., Choi, W., and Tian, Z. (2013). Breaking waves in deep and intermediate waters. *Annual Review of Fluid Mechanics*, 45:115–145.

Pfister, M. (2008). Discussion of "Bubbles and waves description of self-aerated spillway flow" by Wilhelms, S. C. & Gulliver, J. S. (2005). *Journal of Hydraulic Research*, 46(3):420–423.

Pfister, M. and Hager, W. H. (2010a). Chute aerators. I: Air transport characteristics. *Journal of Hydraulic Engineering*, 136(6):352–359.

Pfister, M. and Hager, W. H. (2010b). Chute aerators. II: Hydraulic design. *Journal of Hydraulic Engineering*, 136(6):360–367.

Pfister, M. and Hager, W. H. (2011). Self-entrainment of air on stepped spillways. *International Journal of Multiphase Flow*, 37(2):99–107.

Pfister, M., Hager, W. H., and Boes, R. M. (2014). Trajectories and air flow features of ski jump-generated jets. *Journal of Hydraulic Research*, 52(3):336–346.

Pope, S. B. (2000). *Turbulent Flows*. Cambridge University Press.

Prosperetti, A. and Tryggvason, G. (2009). *Computational Methods for Multiphase Flow*. Cambridge University Press.

Rajaratnam, N. (1965). The hydraulic jump as a well jet. *Journal of the Hydraulics Division*, 91(5):107–132.

Rajaratnam, N. (1967). Hydraulic jumps. In *Advances in Hydroscience*, volume 4, pages 197–280. Academic Press.

Rajaratnam, N. (1976). *Turbulent jets*. Elsevier, Developments in Water Sciences 5.

Rajaratnam, N. (1990). Skimming flow in stepped spillways. *Journal of Hydraulic Engineering*, 116(4):587–591.

Rao, N. S. L. and Kobus, H. E. (1975). *Characteristics of self-aerated free-surface flows*, volume 10 of *Water and Waste Water/Current Research and Practice*. Erich Schmidt Verlag, Berlin.

Rayleigh, L. (1878). On the instability of jets. *Proceedings of the London Mathematical Society*, s1-10(1):4–13.

Rayleigh, L. (1879). On the stability, or instability, of certain fluid motions. *Proceedings of the London Mathematical Society*, 1(1):57–72.

Reynolds, O. (1883). An experimental investigation of the circumstances which determine whether the motion of water shall be direct or sinuous, and of the law of resistance in parallel channels. *Philosophical Transactions of the Royal Society of London*, 174:935–982.

Rodi, W. (1993). *Turbulence models and their application in hydraulics*. Taylor & Francis, 3rd edition.

Rodi, W., Constantinescu, G., and Stoesser, T. (2013). *Large-Eddy Simulation in Hydraulics*. CRC Press, Taylor & Francis.

Rousseeuw, P. J. and Croux, C. (1993). Alternatives to the median absolute deviation. *Journal of the American Statistical Association*, 88(424):1273–1283.

Roussinova, V., Biswas, N., and Balachandar, R. (2008). Revisiting turbulence in smooth uniform open channel flow. *Journal of Hydraulic Research*, 46(sup1):36–48.

Rutschmann, P. and Hager, W. H. (1990). Air entrainment by spillway aerators. *Journal of Hydraulic Engineering*, 116(6):765–782.

Salazar, F., San-Mauro, J., Celigueta, M. Á., and Oñate, E. (2017). Air demand estimation in bottom outlets with the particle finite element method. *Computational Particle Mechanics*, 4(3):345–356.

Savage, B. M. and Johnson, M. C. (2001). Flow over ogee spillway: Physical and numerical model case study. *Journal of Hydraulic Engineering*, 127(8):640–649.

Savelsberg, R. and Water, W. V. D. (2009). Experiments on free-surface turbulence. *Journal of Fluid Mechanics*, 619:95.

Schlichting, H. (1979). *Boundary-layer theory*. McGraw-Hill, 7th edition.

Schmocker, L., Pfister, M., Hager, W. H., and Minor, H.-E. (2008). Aeration characteristics of ski jump jets. *Journal of Hydraulic Engineering*, 134(1):90–97.

Slotnick, J., Khodadoust, A., Alonso, J., Darmofal, D., Gropp, W., Lurie, E., and Mavriplis, D. (2014). Cfd vision 2030 study: a path to revolutionary computational aerosciences. Technical Report NASA/CR-2014-218178, NF1676L-18332.

Soo, S. L. (1956). Statistical properties of momentum transfer in two-phase flow. *Chemical Engineering Science*, 5(2):57–67.

Souders, D. T. and Hirt, C. W. (2004). Modeling entrainment of air at turbulent free surfaces. In *World Water and Environmental Resources Congress 2004*, pages 1–10.

Spalart, P. R. (2000). Strategies for turbulence modelling and simulations. *International Journal of Heat and Fluid Flow*, 21(3):252–263.

Spalart, P. R. and Allmaras, S. R. (1994). A one-equation turbulence model for aerodynamic flows. *La Recherche Aérospatiale*, 1:5–21.

Stokes, G. G. (1880). On the theory of oscillatory waves. *Transactions of The Cambridge Philosophical Society*, 8:441–455.

Straub, L. G. and Anderson, A. G. (1958). Experiments on self-aerated flow in open channels. *Journal of the Hydraulics Division*, 84(7):1–35.

Tamburrino, A. and Gulliver, J. S. (2007). Free-surface visualization of streamwise vortices in a channel flow. *Water Resources Research*, 43(11).

Teixeira, M. A. C. and Belcher, S. E. (2000). Dissipation of shear-free turbulence near boundaries. *Journal of Fluid Mechanics*, 422:167–191.

Tennekes, H. and Lumley, J. L. (1972). *A First Course in Turbulence*. The MIT Press.

Thomas, R. E., Schindfessel, L., McLelland, S. J., Creëlle, S., and De Mulder, T. (2017). Bias in mean velocities and noise in variances and covariances measured using a multistatic acoustic profiler: the nortek vectrino profiler. *Measurement Science and Technology*, 28(7):075302.

Toffoli, A., Babanin, A., Onorato, M., and Waseda, T. (2010). Maximum steepness of oceanic waves: Field and laboratory experiments. *Geophysical Research Letters*, 37(5).

Toombes, L. and Chanson, H. (2005). Air–water mass transfer on a stepped waterway. *Journal of Environmental Engineering*, 131(10):1377–1386.

Toro, J. P., Bombardelli, F. A., and Paik, J. (2017). Detached eddy simulation of the nonaerated skimming flow over a stepped spillway. *Journal of Hydraulic Engineering*, 143(9):04017032.

Valero, D. and Bung, D. B. (2015). Hybrid investigations of air transport processes in moderately sloped stepped spillway flows. In *e-proceedings of the 36th IAHR World Congress, The Hague, The Netherlands*.

Valero, D. and Bung, D. B. (2016). Development of the interfacial air layer in the non-aerated region of high-velocity spillway flows. Instabilities growth, entrapped air and influence on the self-aeration onset. *International Journal of Multiphase Flow*, 84:66–74.

Valero, D. and Bung, D. B. (2018a). Artificial neural networks and pattern recognition for air-water flow velocity estimation using a single-tip optical fibre probe. *Journal of Hydro-environment Research*, 19:150–159.

Valero, D. and Bung, D. B. (2018b). Reformulating self-aeration in hydraulic structures: Turbulent growth of free surface perturbations leading to air entrainment. *International Journal of Multiphase Flow*, 100:127–142.

Valero, D. and Bung, D. B. (2018c). Vectrino Profiler Spatial Filtering for Shear Flows Based on the Mean Velocity Gradient Equation. *Journal of Hydraulic Engineering*, 144(7).

Valero, D., Chanson, H., and Bung, D. B. (2018a). Robust estimation of free surface turbulence properties. *Journal of Hydraulic Research*. (Under review).

Valero, D., Crookston, B. M., and Bung, D. B. (2018b). Energy Dissipation of a Type III Basin under Design and Adverse Conditions for Stepped and Smooth Spillways. *Journal of Hydraulic Engineering*, 144(7).

Valero, D., Felder, S., Wang, H., Pfister, M., and Bung, D. B. (2018c). Air-water open channel flows: historical milestones,

current research and future challenges. *Journal of Hydro-environment Research*. (Under review).

Valero, D. and García-Bartual, R. (2016). Calibration of an air entrainment model for cfd spillway applications. In Gourbesville, P., Cunge, J. A., and Caignaert, G., editors, *Advances in Hydroinformatics: SIMHYDRO 2014*, chapter 38, pages 571–582. Springer Water. Springer, Singapore.

Valero, D., Vogel, J., Schmidt, D., and Bung, D. B. (2018d). Three-dimensional flow structure inside the cavity of a non-aerated stepped chute. In *7th IAHR International Symposium on Hydraulic Structures, Aachen, Germany*.

Versteeg, H. K. and Malalasekera, W. (2007). *An introduction to computational fluid dynamics: the finite volume method*. Pearson Education.

Violeau, D. (2012). *Fluid Mechanics and the SPH method: Theory and Applications*. Oxford University Press.

Violeau, D. and Rogers, B. D. (2016). Smoothed particle hydrodynamics (sph) for free-surface flows: past, present and future. *Journal of Hydraulic Research*, 54(1):1–26.

von Kármán, T. (1921). Über laminare und turbulente Reibung. *Journal of Applied Mathematics and Mechanics (Zeitschrift für Angewandte Mathematik und Mechanik)*, 1(4):233–252.

Wahl, T. L. (2003). Discussion of "Despiking acoustic doppler velocimeter data" by Derek G. Goring and Vladimir I. Nikora. *Journal of Hydraulic Engineering*, 129(6):484–487.

Wan, H., Li, R., Gualtieri, C., Yang, H., and Feng, J. (2017). Numerical simulation of hydrodynamics and reaeration over a stepped spillway by the sph method. *Water*, 9(8):565.

Wang, H. and Chanson, H. (2015). Experimental study of turbulent fluctuations in hydraulic jumps. *Journal of Hydraulic Engineering*, 141(7):04015010.

Wang, H., Slamet, N. S., Zhang, G., and Chanson, H. (2018). Intrusive measurements of air-water flow properties in highly turbulent supported plunging jets and effects of inflow jet conditions. *Chemical Engineering Science*, 177:245–260.

Welch, P. (1967). The use of fast fourier transform for the estimation of power spectra: A method based on time averaging over short, modified periodograms. *IEEE Transactions on Audio and Electroacoustics*, 15(2):70–73.

White, F. M. (2006). *Viscous Fluid Flow*. McGraw-Hill, second edition.

Wilcox, D. C. (2006). *Turbulence Modeling for CFD*. DCW industries La Canada, CA, 3rd edition.

Wilcox, D. C. (2008). Formulation of the k-w turbulence model revisited. *AIAA Journal*, 46(11):2823–2838.

Wilhelms, S. C. and Gulliver, J. S. (2005). Bubbles and waves description of self-aerated spillway flow. *Journal of Hydraulic Research*, 43(5):522–531.

Witt, A., Gulliver, J., and Shen, L. (2015). Simulating air entrainment and vortex dynamics in a hydraulic jump. *International Journal of Multiphase Flow*, 72:165–180.

Wood, I. R. (1983). Uniform region of self-aerated flow. *Journal of Hydraulic Engineering*, 109(3):447–461.

Wood, I. R. (1984). Air entrainment in high speed flows. In *Symposium on Scale Effects in Modelling Hydraulic Structures*.

Wood, I. R. (1985). Air water flows. In *21st IAHR Congress*, pages 18–29.

Wood, I. R. (1991). *Air Entrainment in Free-Surface Flows*. CRC Press, Balkema.

Wood, I. R., Ackers, P., and Loveless, J. (1983). General method for critical point on spillways. *Journal of Hydraulic Engineering*, 109(2):308–312.

Yakhot, V., Orszag, S. A., Thangam, S., Gatski, T. B., and Speziale, C. G. (1992). Development of turbulence models for shear flows by a double expansion technique. *Physics of Fluids A: Fluid Dynamics*, 4(7):1510–1520.

Yih, C.-S. (1963). Stability of liquid flow down an inclined plane. *The Physics of Fluids*, 6(3):321.

Young, W. R. and Wolfe, C. L. (2014). Generation of surface waves by shear-flow instability. *Journal of Fluid Mechanics*, 739:276–307.

Zhang, G. and Chanson, H. (2016a). Hydraulics of the developing flow region of stepped spillways. I: Physical modeling and boundary layer development. *Journal of Hydraulic Engineering*, 142(7):04016015.

Zhang, G. and Chanson, H. (2016b). Hydraulics of the developing flow region of stepped spillways. II: Pressure and velocity fields. *Journal of Hydraulic Engineering*, 142(7):04016016.

Zhang, G. and Chanson, H. (2016c). Interaction between free-surface aeration and total pressure on a stepped chute. *Experimental Thermal and Fluid Science*, 74:368–381.

Zhang, G. and Chanson, H. (2018). Application of local optical flow methods to high-velocity free-surface flows: Validation

and application to stepped chutes. *Experimental Thermal and Fluid Science*, 90:186–199.

Zhang, G., Chanson, H., and Wang, H. (2016). Total pressure fluctuations and two-phase flow turbulence in self-aerated stepped chute flows. *Flow Measurement and Instrumentation*, 51:8–20.

Zhang, G., Valero, D., Bung, D. B., and Chanson, H. (2018). On the estimation of free-surface turbulence using ultrasonic sensors. *Flow Measurement and Instrumentation*, 60:171–184.

Zhang, G., Wang, H., and Chanson, H. (2013). Turbulence and aeration in hydraulic jumps: free-surface fluctuation and integral turbulent scale measurements. *Environmental Fluid Mechanics*, 13(2):189–204.

Zhong, Q., Chen, Q., Wang, H., Li, D., and Wang, X. (2016). Statistical analysis of turbulent super-streamwise vortices based on observations of streaky structures near the free surface in the smooth open channel flow. *Water Resources Research*, 52(5):3563–3578.

Appendices

Appendix A

Ultrasonic sensors performance

A.1 Presentation

The microsonic^{TM} mic+130 ultrasonic sensor (USS) has a detection cone with radii ranging approximately between 0.02 m and 0.1 m, depending on the object distance from the sensor. The actual detection zone further depends on material acoustic properties and surface roughness characteristics. The distance measured by the USS is also dependent on the spatial distribution of intensities of the emitted beamlet, which can be characterised by a complex pattern but is always strongest along the sensor

axis. Therefore, the most robust measurements are taken along the central axis.

In first approximation, a roughened water surface may be understood as a set of piecewise linear elemental surfaces on which the ultrasound reflection is specular. The echoes picked up by the USS comprise series of signals reflected by the individual surface elements, which are orthogonal to the direction of propagation of the emitted beam. When multiple echoes are present, preliminary tests (with arrangements of multiple objects at various depths) suggested that the USS strongly favoured the foreground signal (i.e. the first obstacle met by the echoes).

Consequently, USS measurement over a rough water surface would result in a characteristic distance, determined by the integral of the signals reflected from the stationary phase points within the first half Fresnel zone of the acoustic signal, which may vary depending upon the instantaneous water surface geometry covered by the USS footprint (as opposed to the commonly expected average value). A complete study on the accuracy of this sensor for two-dimensional and three-dimensional waves can be found in the study of Zhang et al. (2018).

Herein, the USSs were tested in dry conditions to observe their capabilities and signal characteristics. The voltage responses of three USS were examined by placing a perpendicular solid plastic surface at different distances from the sensor. The voltage – distance relationship was linear throughout the measur-

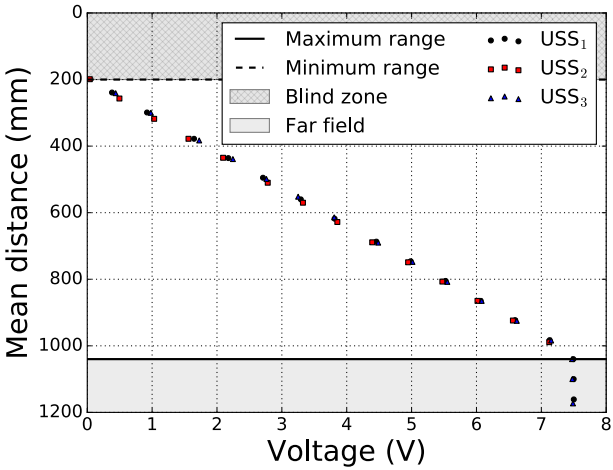

Fig. A.1 Linear calibration curve obtained from static measurements at different distances from the USS without any signal filtering.

ing range of the sensor. A “blind zone” and a “far field” were respectively identified close to and away from the sensor, as per Fig. A.1. The standard deviation of each static measurement was interpreted as the measurement uncertainty, which remained approximately constant over the full detectable range. The results showed no preferential measuring distance despite the maximum detected deviation (around 1 mm) seemed to increase with distance (Fig. A.2). Data from Fig. A.1 and A.2 were sampled over 30 s.

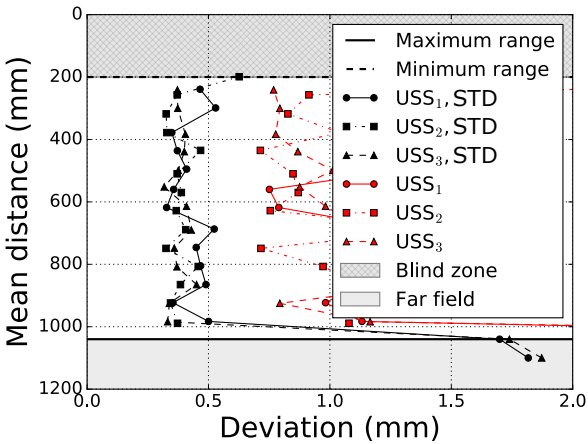

Fig. A.2 Standard deviation (STD) and maximum deviation (red lines) of a static measurement at different distances from the USS without any signal filtering.

The detection cone of the USS is shown in Fig. A.3. The USS footprint was measured by fixing the sensor and introducing a plate at different distances away from the transducer while recording the distance from the centreline at which the USS detected the obstacle. The USS signal changes in a space of around 1 mm. The sensing cone shown in Fig. A.3 spreads with distance at an angle of roughly 4 °.

The sensor allows internal adjustment of the detection zone (options: "normal/slight"), although no significant difference was found between the options (Fig. A.3). The sensitivity of the sensing error to surface slope (β) variations is examined in Fig. A.4. A low number of outliers were observed for surface slopes flatter than 13.5 degrees.

The temperature dependence of the USS was investigated by undertaking long measurements of 12 hours at a sample rate of 1 Hz. In Fig. A.5, only the data for the first 6 hours are shown for clarity. Notably, most significant changes in the sample mean were observed during the first hour. Consequently, a minimum warm-up period of 1 hour is recommended, as advised by the manufacturer, after which the calibration curve shall be obtained, prior to the data acquisition.

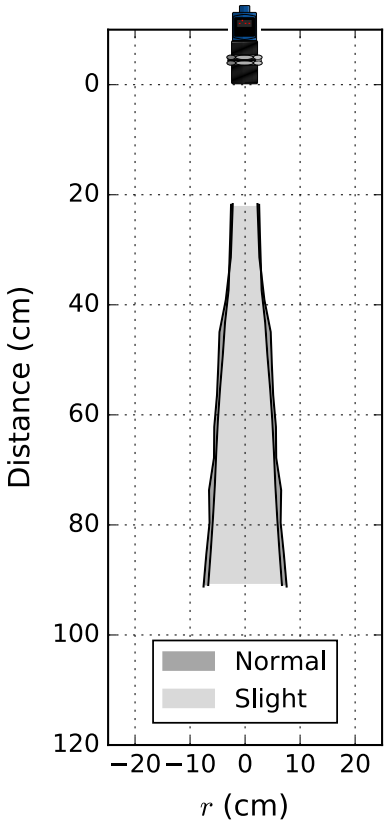

Fig. A.3 Detection cone of a USS measured at the laboratory (present model). Objects are detected when placed within the sensor's detection radius (r), which is a function of the surface roughness.

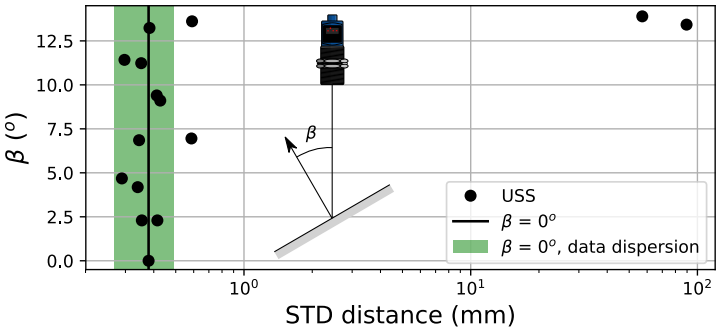

Fig. A.4 USS performance dependence on the surface slope.

A.2 Sample rate, aliasing and noise

The USS operates by measuring the time lag between the emitted and reflected ultrasound pulses. The pulses are emitted at a pre-established interval to ensure that all meaningful echoes are captured before a new pulse is broadcast. The shortest pulse interval determines the maximum frequency that needs to be resolved by the data acquisition system of which the sampling frequency must be appropriately chosen.

The Nyquist sampling theorem requires this to be equal to or greater than twice the maximum frequency present in the signal (i.e., Nyquist frequency). This minimum sampling frequency is known as the Nyquist rate. Failure to satisfy the Nyquist criterion will result in a higher frequency signal with frequency f, manifesting as a lower frequency component with an apparent

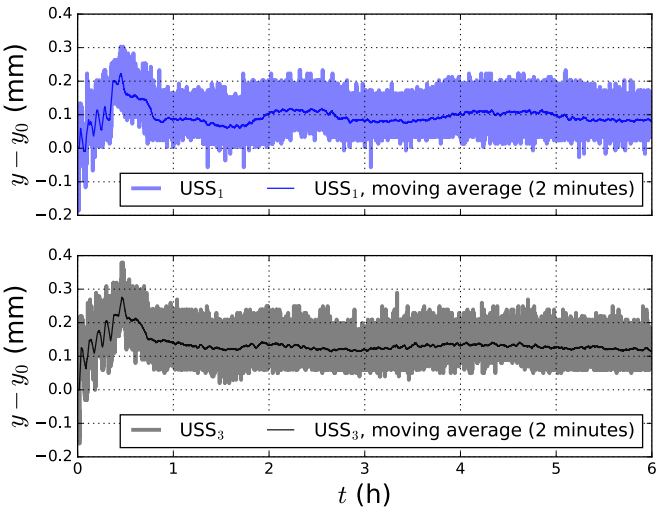

Fig. A.5 Long time record of USS signals for two different sensors. Temperature has significant effects on sensor data during the first hour. The initially measured distance (y_0) is subtracted to the recording (y).

frequency equalling $|f_S - f|$ where f_s is the sampling frequency. As such, the original signal can no longer be reconstructed by low pass filtering without distortion and this is referred to as aliasing.

The effects of sampling rate and analogue filtering were first investigated by examining the USS signal power spectral densities plotted in Fig. A.6. The data were sampled with the USS facing a fixed flat surface perpendicular to the sensor centreline. The signal mean was removed prior to computing the power spectral density functions. The oversampled power spectral density function at 1,200 Hz (Fig. A.6 black/grey lines) shows a steep roll-off above 20 Hz and an isolated peak at 60 Hz. The latter peak likely arose from the connected electronics, as the local main frequency was 50 Hz. The USS signal was therefore approximately band-limited up to 20 Hz, and a minimum sampling rate of 50 Hz is recommended to minimise aliasing distortion. Note that a minimum sampling rate of 10 times the Nyquist frequency (i.e. 250 Hz for a sampling rate of 50 Hz) may be required for accurate waveform reproduction.

Analysis of Fig. A.6 indicates that a minimum sampling rate of 50 Hz may be appropriate. The typical USS noise power spectral density function sampled at this rate, with all filters disabled, is shown in Fig. A.7. The data revealed an aliased peak at 10 Hz due to power fluctuations, which may not be important if the signal-to-noise ratio is large. The power spectral density function was approximately white (i.e., equal intensity

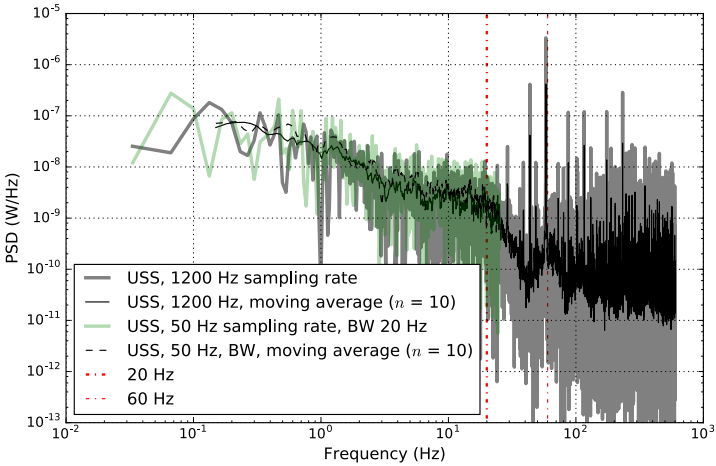

Fig. A.6 Effects of sampling rate and analogue filtering on USS signal power spectral density function (PSD). BW for Butterworth filtered signals.

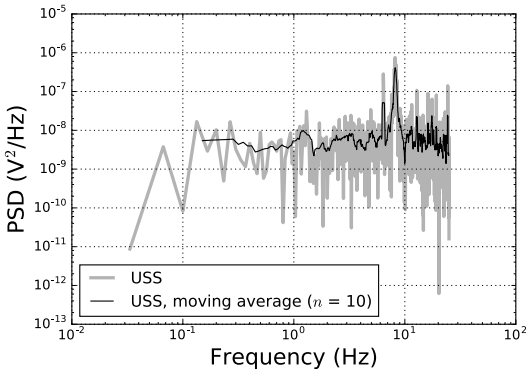

Fig. A.7 Typical noise power spectral density function (PSD) of a USS signal. Sampling rate: 50 Hz. Sampling duration: 30 s.

in all frequencies) up to the Nyquist frequency (25 Hz) due to the combined effects of temperature, surface-characteristics and intrinsic electrical noise of the system.

A.3 Uncertainty

Any USS sensor has a limited response time, which represents a limitation when measuring high frequencies. In order to investigate the performance of the USS at those frequencies, experiments with a vibrating plate were conducted.

A PVC plate was fixed over an aluminium bar (isel^{TM}, universalprofile PU50), whose combination of elasticity modulus

(E = 70 GPa), linear weight (1.22 kg/m), inertias (in both transversal axis, I_x = 10.99 cm^4 and I_y = 2.81 cm^4) and length (initially 3 m) allowed study of frequencies up to 30 Hz.

The bar was fixed to a solid and massive metal structure so that a cantilever resulted with the plastic plate close to the bar extremity. Two USS sensors were placed at 0.50 m above the plastic plate and were separated by 0.20 m to avoid interference. The bar was shortened iteratively, thereby increasing the stiffness of the system. For each length investigated, the bar was stimulated with a fast impact producing oscillations with amplitudes significantly above those of the USS noise.

Two bars were used, profiting from both transversal inertias to cover a wider range of frequencies. The high-speed camera was employed using significantly higher sample rates (over ten times the bar frequency) to obtain the real frequency of the vibrating system. The frequencies in both cases were estimated by counting zero-crossings over the first second after the impact.

A close correspondence is observed between the camera and USS frequencies up to 20 Hz, while frequencies above 20 Hz were increasingly under-estimated by the USS. To gain further insight, a simple case where a plate oscillates as described by the sine equation is considered:

$$h'(t) = A\sin(2\pi f t + \varphi) \tag{A.1}$$

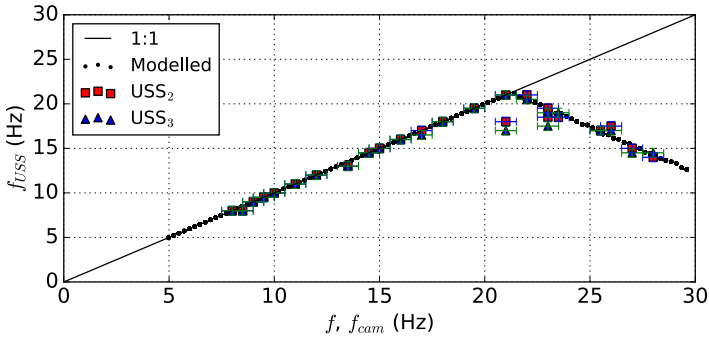

Fig. A.8 Frequency detected by the ultrasonic sensor (f_{USS}) against frequency detected with the high-speed camera (f_{cam}) and modelled frequency (f).

where A is the amplitude, f the frequency of the oscillation, t the time and φ the initial phase shift. If the speed of the plate is considerably smaller than the speed of the sound ($v \ll c$), then it is reasonable to assume that the sensor will see the object at every sampling time as static, i.e.: as a fixed plate at a different height each time.

For different values of f, Eq. A.1 can be used to generate a new signal. A hundred different frequencies, with a hundred different initial phase shifts (randomly initialised), have been used to render synthetic signals with $N = 100$ number of complete periods. Zero-crossings can be counted in a similar manner to that for the vibrating plate tests, thus recovering the same original

frequency. This signal can also be reproduced by subsampling, as an USS naturally does due to its limited sampling. A best match was found for f_{sample} = 43 Hz, which corresponds to a cutoff frequency of 21 Hz, corroborating with the considerations in the previous subsections.

In Fig. A.8, the theoretical response of the USS is shown as "modelled". It must be noted that the expected decay of the frequency detected by the USS agrees with the experimental observations. For frequencies below 21 Hz the response of the USS is satisfactory. In the case of a small N, the under-sampled frequencies ($f > 21$ Hz) would show larger scatter while the lower frequencies still fit perfectly to the 1:1 line.

It is also of interest to analyse how under-sampling would affect the prediction of wave amplitudes for different wave frequencies. The expected absolute value of the fluctuation ($\langle |h'| \rangle$) resulting from this under-sampling is shown in Fig. A.9. The uncertainty grows linearly with the oscillation frequency. It has also been observed that the widths of these bounds are reduced by increasing the number of sampled waves (N). Thus, the uncertainty associated to under-sampling can be compensated by a larger number of sampled processes.

The standard deviation (STD) of a sine wave is given by:

$$\mathrm{STD}\left(h'\right) = A/\sqrt{2} \tag{A.2}$$

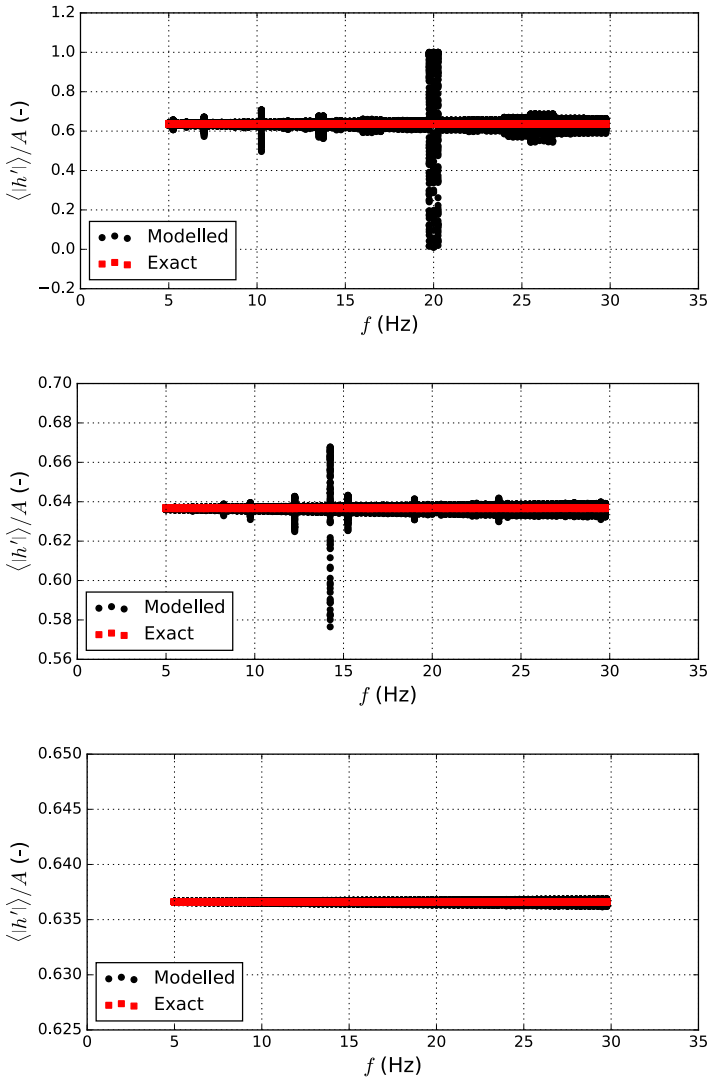

Fig. A.9 Uncertainty in the absolute value of the fluctuation depending on the frequency of the measured oscillating process. Top: $N = 10$; middle: $N = 100$; bottom: $N = 1000$.

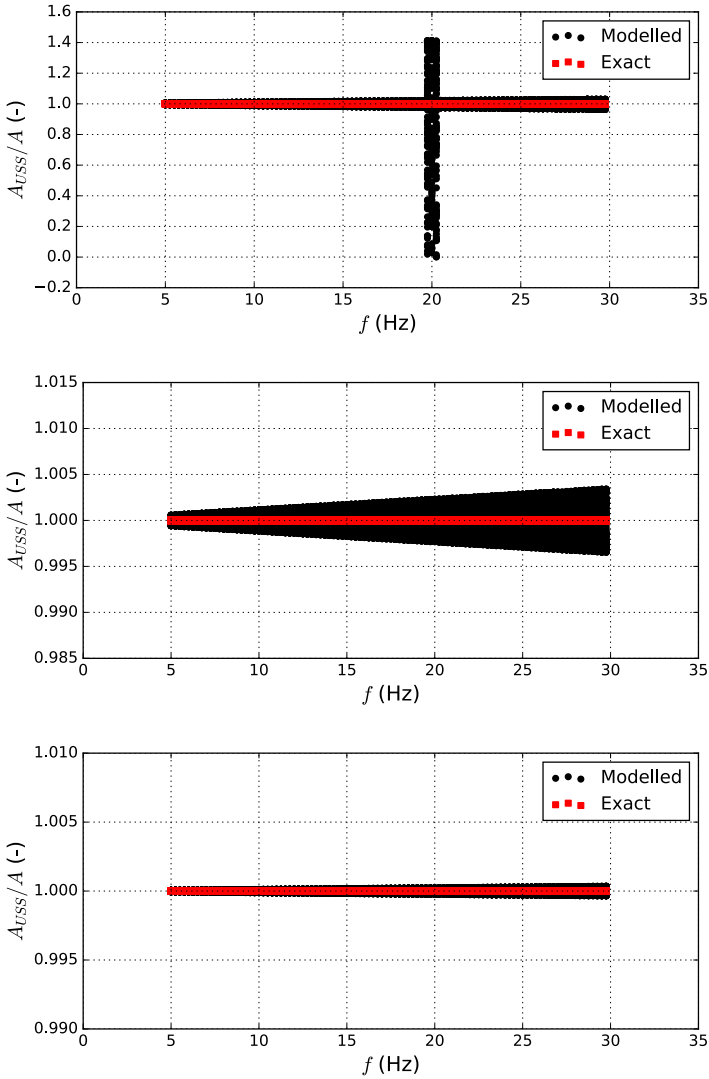

Fig. A.10 Pseudoamplitude resulting from USS under-sampling. Top: N = 10; middle: N = 100; bottom: N = 1000. Note the different range of the amplitude axis.

which can be obtained from the sampled synthetic signals. A pseudoamplitude can be recovered by emulating the amplitude which might be obtained from the USS sampling:

$$A_{USS} = \mathrm{STD}\left(h'\right)\sqrt{2} \tag{A.3}$$

The resulting pseudoamplitude A_{USS} is shown in Fig. A.10. It can be observed, similarly to Fig. A.9, that for small sampling durations a considerably large uncertainty band appears at around 20 Hz. Similar to the absolute amplitude, incrementing the number of sampled events reduces the uncertainty bound.

Appendix B

Perturbation curvature

This appendix contains the necessary equations to easily compute the perturbation's crest surface curvature using the full differential geometry approach of Eq. 8.22.

The perturbation defined in Eq. 7.1 admits analytical determination of its intersection with coordinates planes xz and yz (constant y and x, correspondingly), yielding easy computation of the surface curvatures in each plane.

Using the coordinate system X and Y centred at the axis of the perturbation, the line resulting from the intersection of Eq. 7.1 and the plane yz (i.e., η_{yz}) for $r < \lambda/2$:

$$\eta_{yz} = \frac{A_{yz}}{2} \cos\left(\frac{2\pi Y}{\lambda_{yz}}\right) + \frac{A_{yz}}{2} \tag{B.1}$$

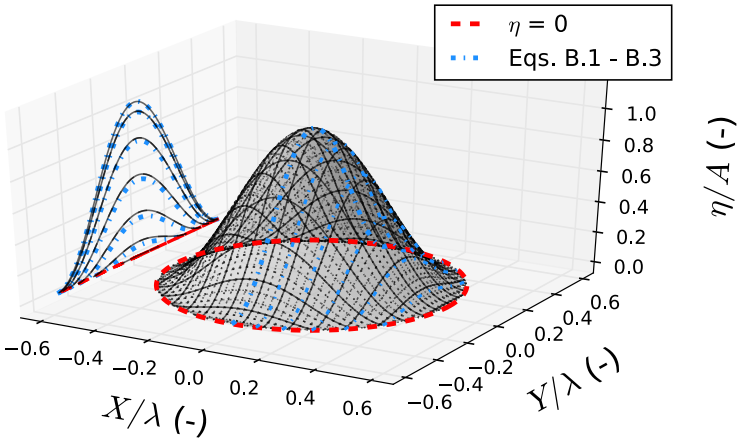

Fig. B.1 Constant X planes for $r < \lambda/2$ (Eqs. B.1 to B.3) shown over the crest of the perturbation, as defined by Eq. 7.1.

where A_{yz} and λ_{yz} depend on the local coordinates (X, Y) and can be obtained by use of basic geometrical considerations. The new amplitude term can be computed using Eq. 7.1:

$$A_{yz} = \frac{A}{2}\cos\left(\frac{2\pi X}{\lambda}\right) + \frac{A_{yz}}{2} \tag{B.2}$$

and the new wavelength is limited by a circle at $\eta = 0$, thus:

$$\lambda_{yz}/2 = \sqrt{(\lambda/2)^2 + X^2} \tag{B.3}$$

The defined intersection with several coordinate planes is shown in Fig. B.1.

The A_{yz} and λ_{yz} parameters are constant for a given value of X and, therefore, y derivative becomes easy to obtain.

$$\frac{\partial \eta_{yz}}{\partial y} = -\pi \frac{A_{yz}}{\lambda_{yz}} \sin\left(\frac{2\pi Y}{\lambda_{yz}}\right) \tag{B.4}$$

and the second derivative:

$$\frac{\partial^2 \eta_{yz}}{\partial y^2} = -2\pi^2 \frac{A_{yz}}{\lambda_{yz}^2} \cos\left(\frac{2\pi Y}{\lambda_{yz}}\right) \tag{B.5}$$

Similar considerations hold for η_{xz}.

Appendix C

Robust outlier cutoff filtering

Data gathered by the USS can contain outliers due to many reasons (Zhang et al., 2018). Proper data filtering is necessary to avoid accounting for the USS noise as turbulence. Outliers depart from the expected estimation of the flow depth but do not necessarily accumulate at the lower and upper bounds. When obtaining the Probability Mass Function (PMF) some erroneous measurements can be observed to run together at different voltage levels (Fig. C.1). A quick flow observation indicates that these voltage values associated to different water levels are not taking place and, hence, definition of narrow bounds becomes necessary.

A commonly used technique is to estimate the variance of the sample, estimated by means of the STD, to establish the filtering bounds around a certain number of STD away from the mean. However, the STD approximates the population variance using the squared value of each sample, thus endorsing bigger weight to the outliers. Using this overestimated variance to discard outliers would result in larger rates of acceptance of outliers and, consequently, in the overestimation of the depth variance (i.e., the free surface turbulent properties). Additionally, the mean value can also be affected by the presence of outliers. Further discussion on the inadequacy of using mean and standard deviation can be found in Leys et al. (2013).

Alternatively, the median (MED) and the Median Absolute Deviation (MAD) can be used as estimators of location and variance, being both robust estimators against outliers with a breakdown point of 50 %[1] as opposed to the counterpart mean and standard deviations which hold a 0 % breakdown point[2].

It must be noted that the median is the location estimator that presents the highest breakdown point (Leys et al., 2013). Similarly, the MAD represents the best robust scale estimator, even more than the classical interquartile range that remains at a 25 % breakdown point (Leys et al., 2013; Rousseeuw and Croux, 1993). The use of both MED and MAD was already suggested

[1] 50 % of contaminated data is necessary to force the estimator to result in a false output.

[2] A single extreme value would modify its estimation.

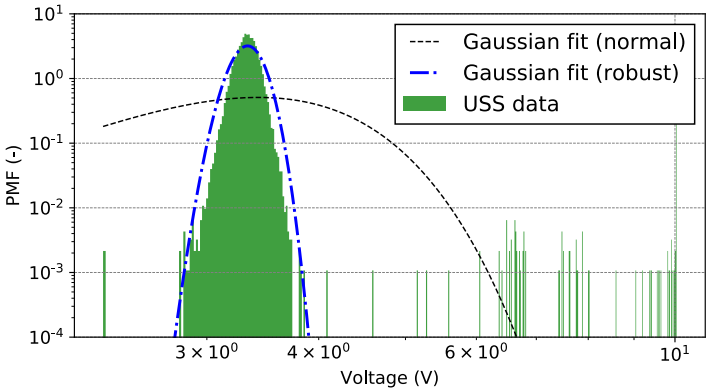

Fig. C.1 Probability Mass Function (PMF) of a USS voltage signal for $h_c/s = 2.1$ and step V (see Fig. 10.3). Note that axes are both in log-scale, which allows better insight on the structure of the outliers, that spread at different voltage levels. Two Gaussian distributions are fitted using the mean and STD ("normal") and the proposed MED and MAD estimators ("robust"), showing a significant difference in the outliers detection.

by Wahl (2003) for the detection and removal of velocity data outliers. Difference between normal and robust estimators can be well perceived from Fig. C.1, where a Gaussian is fitted by using the moments method obtaining the location and variance with the normal estimators (mean and STD) and with the robust estimators (MED and MAD). Figure C.1 also shows a small proportion of outliers piling up at different voltage levels which are easily observable when using a vertical log-scale.

The MAD was popularized by Hampel (1974), who argued that it was Carl Friedrich Gauss originally proposing this estimator. It can be obtained by sorting the absolute value of the residuals around the median and selecting the value corresponding to the 50 %. It is implemented in many commonly used numerical libraries (e.g., MATLAB, R programming language or Python 2.7 together with the statsmodels library, being the latter combination the one used for this analysis).

The MAD of the sampled flow depth (h) can be related to the standard deviation of different probability density functions as (Rousseeuw and Croux, 1993):

$$\tilde{h}' = \varphi \, \mathrm{MAD}\,(h) = \varphi \, \mathrm{MED}\,(|\eta|) \tag{C.1}$$

being φ a coefficient and η the time series of the free surface deviation from the median value (see also, Fig. 6.2):

$$\eta = h - \overline{h} \tag{C.2}$$

with $\overline{h}$ the expected value of h, obtained by using the MED operator. When a Gaussian behaviour is assumed (Rousseeuw and Croux, 1993):

$$\varphi = 1.483 \tag{C.3}$$

On the question of how many standard deviations are necessary to be accounted to make sure that "good data" is not filtered out, the universal threshold represents a conservative estimator. It can be expressed as (Goring and Nikora, 2002):

$$\zeta_u = \sqrt{2 \log N} \tag{C.4}$$

with N the total number of data points of the sample. Use of the universal threshold yields bounds wide enough to avoid filtering out good data even if the underlying distribution is slightly skewed, but (usually) narrower bounds than just cutting extreme physically meaningless values. Hence, skewness of the flow depth distribution should not be affected by the filtering.

In the case that the final distribution of the sample results considerably skewed, MAD could be estimated for both deviations departing from the MED value on the upper and lower directions and, consequently, different filtering thresholds could be defined for both positive and negative deviations. Rearranging the equations, the filtering criterion can be written as:

$$|\frac{\eta}{\varphi \, \mathrm{MAD}(\eta)}| \leq \zeta_u \tag{C.5}$$